

RPSEA

Corrosion-Fatigue Performance of High-Strength Riser Materials in Seawater and Sour Brine Environments

07121-1403.FINAL

Fatigue Performance of High-Strength Riser Materials Subjected to Sour Environments

DEAC2607NT42677

February 29, 2012

Stephen J. Hudak, Jr., Principal Investigator,
James H. Feiger, and Guadalupe B. Robledo
Southwest Research Institute®
San Antonio, TX 78238-5166

and

Jeffrey Hawk
DOT-National Energy Technology Laboratory (NETL)
Albany, OR 97321-2198

LEGAL NOTICE

This report was prepared by Southwest Research Institute (SwRI®) as an account of work sponsored by the Research Partnership to Secure Energy for America, RPSEA. Neither RPSEA members of RPSEA, the National Energy Technology Laboratory, the U.S. Department of Energy, nor any person acting on behalf of any of the entities:

- a. MAKES ANY WARRANTY OR REPRESENTATION, EXPRESS OR IMPLIED WITH RESPECT TO ACCURACY, COMPLETENESS, OR USEFULNESS OF THE INFORMATION CONTAINED IN THIS DOCUMENT, OR THAT THE USE OF ANY INFORMATION, APPARATUS, METHOD, OR PROCESS DISCLOSED IN THIS DOCUMENT MAY NOT INFRINGE PRIVATELY OWNED RIGHTS, OR**
- b. ASSUMES ANY LIABILITY WITH RESPECT TO THE USE OF, OR FOR ANY AND ALL DAMAGES RESULTING FROM THE USE OF, ANY INFORMATION, APPARATUS, METHOD, OR PROCESS DISCLOSED IN THIS DOCUMENT.**

THIS IS A FINAL REPORT. THE DATA, CALCULATIONS, INFORMATION, CONCLUSIONS, AND/OR RECOMMENDATIONS REPORTED HEREIN ARE THE PROPERTY OF THE U.S. DEPARTMENT OF ENERGY.

REFERENCE TO TRADE NAMES OR SPECIFIC COMMERCIAL PRODUCTS, COMMODITIES, OR SERVICES IN THIS REPORT DOES NOT REPRESENT OR CONSTITUTE AND ENDORSEMENT, RECOMMENDATION, OR FAVORING BY RPSEA OR ITS CONTRACTORS OF THE SPECIFIC COMMERCIAL PRODUCT, COMMODITY, OR SERVICE.

ABSTRACT

Corrosion-fatigue is a significant design consideration in deepwater floating production systems. Mechanical loading is accentuated due to the compliant nature of these structures, and sour service conditions can also occur either due to the nature of the crude production or due to seawater flooding of the reservoir to enhance production yield. Although new high-strength riser steels have recently been developed to meet the demands of deepwater development, the corrosion-fatigue performance of these new materials is largely unknown.

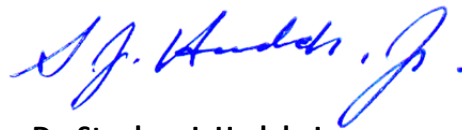
The goal of this study was to fill this knowledge gap by generating corrosion-fatigue data in two aggressive environments: 1.) seawater with cathodic protection representative of the environment outside the riser and 2.) sour brine with low-oxygen ($O_2 < 10$ ppb) representative of the environment inside the riser. Laboratory air data was also generated to provide a baseline for comparison with the above aggressive environments. Experiments were performed on five different steels with yield strengths ranging from 848 to 1080 MPa, and one titanium alloy (Ti Grade 29) with a yield strength of 786 MPa. However, not all steels were tested in the sour brine environment since two of the steels were not designed to operate in sour service. The Ti-alloy was only tested in sour brine since prior data are available on this material in seawater environments. These materials were characterized in terms of crack growth rates as a function of applied stress intensity factor range, da/dN (ΔK), which can be used to set inspection limits in riser design, or for engineering critical assessments. Classical S-N fatigue data were also generated using full-thickness strip fatigue specimens extracted from the pipe wall.

Material strength level and cyclic loading frequency were found to be key variables affecting corrosion-fatigue crack growth rates. For both environments, the highest strength steels were found to exhibit higher growth rates and lower saturation frequencies – that is a frequency below which the rates no longer increased with further decreases in frequency – than the lower strength steels. Fatigue crack growth rates as a function of ΔK were also measured, and exhibited two different frequency responses. At high ΔK , the classical frequency response occurred: decreased frequency gave increased crack growth rates. At low ΔK , an inverse frequency effect was observed: decreased frequency gave decreased crack growth rates, as well as increased corrosion-fatigue crack growth thresholds. These differences are believed to be caused by different underlying processes controlling crack growth – specifically, material-environment reaction kinetics at high ΔK , and crack-closure due to corrosion-product wedging at low ΔK . Because of this complex frequency dependence, the S-N corrosion-fatigue data were generated at different frequencies (0.01Hz, 0.17 Hz, and 1 Hz) selected to match the frequencies experienced by risers in different applied stress and fatigue life regimes, within practical limits.

In S-N testing, corrosion-fatigue in both environments occurred at stresses well below the fatigue endurance limit in laboratory air. Cyclic lives in the seawater with cathodic protection environment were found to be between two and ten times less than

those in the baseline air environment, while cyclic lives in the sour brine environment were found to be 30 to 100 times less than those in the baseline air environment. In both environments, degradation was greatest at lower stresses in the high-cycle-fatigue regime. The effect of material strength level had little or no measurable effect on the S-N corrosion-fatigue performance, and the effect of cyclic frequency on the corrosion-fatigue performance was mixed. The S-N response to these two variables differed significantly from the fatigue crack growth kinetics measured in these same materials. Possible reasons for these differences are discussed.

The Ti-29 alloy exhibited significantly different fatigue crack growth and S-N fatigue behavior than did the steels. At high ΔK , the baseline fatigue crack growth rates in Ti-29 in air exhibited rates that were three to four times greater than those in the steels; this difference is believed to be due to the effect of the lower modulus and lower ductility in Ti-29 compared to those in the steels. In contrast, at low ΔK , the rates in Ti-29 in air were equal to or less than those in the steels of comparable strength levels. In sour brine at ΔK values of 20 MPa \sqrt{m} and above, the rates in sour brine were up to two to four times greater than those in air; however, at low ΔK the rates in sour brine merged with those in air. Consequently, at high ΔK , the higher baseline rates in air plus the increase of two to four times in the sour brine environment gave corrosion-fatigue crack growth rates in Ti-29 that approached those of the steels; however, at low ΔK the reduction in the crack driving force in Ti-29 due to roughness-induced crack closure, particularly in the sour brine environment, resulted in Ti-29 rates that were comparable to air crack growth rates in steels. The S-N fatigue lives of Ti-29 in sour brine were reduced by a factor of about two compared to those in air (for Ti-23 available from the literature). These Ti-29 S-N fatigue lives in sour brine were eight to ten times better than those in the steels in sour brine. Thus, for sour-service applications in the intermediate- and high-cycle fatigue regimes, Ti-29 has more favorable corrosion-fatigue performance than that of the steels.



Dr. Stephen J. Hudak, Jr.
Principal Investigator
Southwest Research Institute
February 29, 2012

APPROVED:



Dr. Ben H. Thacker
Director, Materials Engineering Department
Southwest Research Institute
February 29, 2012

THIS PAGE INTENTIONALLY LEFT BLANK

TABLE OF CONTENTS

Section	Page
ABSTRACT	iii
1.0 INTRODUCTION	1
2.0 RESEARCH OBJECTIVE AND APPROACH	2
3.0 MATERIALS AND ENVIRONMENTS	3
4.0 EXPERIMENTAL PROCEDURES	7
4.1 Fatigue Crack Growth Rate Testing	7
4.2 S-N Fatigue Testing	8
4.3 Test Environment Containment, Control and Safety Considerations	10
5.0 CORROSION-FATIGUE CRACK GROWTH RATE RESULTS AND DISCUSSION	12
5.1 Steel Corrosion-Fatigue Crack Growth Rates	12
5.1.1 Steel Fatigue Crack Growth Rates in Lab Air	12
5.1.2 Effect of Loading Frequency on Steel Corrosion-Fatigue Crack Growth Rates	14
5.1.3 Effect of Hydrogen Source on Frequency Response	20
5.1.4 Effect of Frequency Schedule on Steel Corrosion-Fatigue Crack Growth Rates Versus ΔK	21
5.1.5 Possible Mechanisms Causing Inverse Frequency Effects in Steels	20
5.1.6 Effect of Steel Strength Level on Corrosion-Fatigue Crack Growth Rates vs. ΔK	33
5.2 Ti-29 Corrosion-Fatigue Crack Growth Rates	38
5.2.1 Ti-29 Fatigue Crack Growth Rates in Lab Air	38
5.2.2 Effect of Loading Frequency on Ti-29 Corrosion-Fatigue Crack Growth Rate	40
5.2.3 Ti-29 Corrosion-Fatigue Crack Growth Rates Versus ΔK	46
6.0 S-N FATIGUE RESULTS AND DISCUSSION	49
6.1 High-Strength Steel S-N Corrosion-Fatigue Results and Discussion	49
6.1.1 Steel S-N Fatigue Lives in Lab Air	49
6.1.2 Steel S-N Corrosion-Fatigue Lives in Seawater with Cathodic Protection	51
6.1.3 Steel S-N Corrosion-Fatigue Lives in Sour Brine	52
6.1.4 Effect of Loading Frequency on S-N Corrosion-Fatigue Life	53

TABLE OF CONTENTS *(Continued)*

Section	Page
6.1.5 Comparison of S-N Corrosion-Fatigue in High-Strength Steels Versus X65 Steel.....	55
6.1.6 Comparison of Corrosion-Fatigue Trends in S-N Versus Crack Growth Results.....	57
6.2 Ti-29 S-N Corrosion-Fatigue Results and Discussion.....	58
6.2.1 Ti-29 S-N Corrosion-Fatigue in Sour Brine	58
6.2.2 Comparison of S-N Corrosion-Fatigue Performance of Ti-29 and Steels	60
7.0 SUMMARY AND CONCLUSIONS	61
7.1 Corrosion-Fatigue Crack Growth Rates.....	61
7.1.1 Steel $da/dN(\Delta K)$ Summary and Conclusions	61
7.1.2 Ti-29 Alloy $da/dN(\Delta K)$ Summary and Conclusions	62
7.2 S-N Corrosion-Fatigue Life	63
7.2.1 Steel S-N Summary and Conclusions	63
7.2.2 Ti-29 S-N Summary and Conclusions	64
8.0 ACKNOWLEDGEMENTS	64
9.0 REFERENCES	65

LIST OF TABLES

Table		Page
3-1	Pipe outer diameters and wall thicknesses of the materials examined in the current project.....	3
3-2	Average tensile properties of the five high-strength steels and one Ti-alloy characterized in the current program, along with corresponding corrosion-fatigue test environments	4
3-3	Potential applications of the materials examined in the current project	4
3-4	Sour brine gas mixture and brine chemistry.....	5
5-1	Influence of steel strength level on nominal corrosion-fatigue crack growth rates in offshore environments (at $\Delta K = 22 \text{ MPa}\sqrt{\text{m}}$, $R = 0.5$, and frequency = 0.01 Hz) relative to the baseline rate in lab air.....	20
5-2	Surface topography for Ti-29 corrosion-fatigue cracks grown in air versus sour brine environments.....	45

LIST OF FIGURES

Figure		Page
3-1	Steel pipes with outer diameters ranging from 284 mm to 406 mm and wall thickness from 13.8 mm to 33.5 mm.....	3
3-2	Polyethylene brine make-up tank and oxygen purging tank with Orbisphere oxygen meter and flow loop control system used to start the sour brine tests	6
4-1	Compact-type specimen used for fatigue crack growth rate testing (units in mm)	8
4-2	Typical S-N fatigue strip specimen and example cutting plan for specimen removal from pipe; depending on pipe diameter, three-to-five specimens were removed from each pipe segment.....	9

LIST OF FIGURES (*Continued*)

Figure	Page
4-3 Photograph of convex and concave brass inserts used in the grips to apply a uniform clamping force across the curved section of the strip fatigue S-N specimens.....	10
4-4 Triple-containment chamber components for S-N fatigue testing in sour brine environment	11
5-1 Summary of fatigue crack growth rate data for five different steels in lab air showing trend, at a given ΔK , of increasing rates with increasing material yield strength (YS)	13
5-2 Frequency-scan results in 848 MPa YS steel in seawater environment	14
5-3 Frequency-scan results in 910 MPa YS steel in seawater environment	15
5-4 Frequency-scan results in 924 MPa YS steel in seawater environment	15
5-5 Frequency-scan results in 945 MPa YS steel in seawater environment	16
5-6 Frequency-scan results in 1080 MPa YS steel in seawater environment	16
5-7 Summary of frequency response in seawater versus steel yield strength (YS)....	17
5-8 Frequency-scan results in 848 MPa YS steel in sour brine environment	18
5-9 Frequency-scan results in 924 MPa YS steel in sour brine environment	18
5-10 Frequency-scan results in 945 MPa YS steel in sour brine environment	19
5-11 Summary of frequency response in sour brine versus steel yield strength (YS)	19
5-12 The effect of frequency schedule on the seawater corrosion-fatigue crack growth rates in the 848 MPa YS steel	22
5-13 The effect of frequency schedule on the seawater corrosion-fatigue crack growth rates in the 910 MPa YS steel	23

LIST OF FIGURES *(Continued)*

Figure	Page
5-14 The effect of frequency schedule on the seawater corrosion-fatigue crack growth rates in the 924 MPa YS steel	23
5-15 The effect of frequency schedule on the seawater corrosion-fatigue crack growth rates in the 945 MPa YS steel	25
5-16 The relative ΔK -independence of seawater corrosion-fatigue crack growth rate in the 1080 MPa YS steel	27
5-17 The effect of frequency schedule on the sour brine corrosion-fatigue crack growth rates in the 848 MPa YS steel	28
5-18 The effect of frequency schedule on the seawater corrosion-fatigue crack growth rates in the 945 MPa YS steel	29
5-19 Influence of frequency on crack growth in an aqueous $H_2S + CO_2$ environment [8, 9]	30
5-20 Variation in crack closure and effective crack-driving force over time for experiments conducted in aqueous $H_2S + CO_2$ environment at various cyclic frequencies [8, 9]	31
5-21 Notional representation of complex dependence of fatigue crack growth rates on cyclic frequency hypothesized based on current understanding of crack closure associated with corrosion-product induced wedging	32
5-22 Corrosion-fatigue crack growth rates in seawater and air as a function of steel strength for Frequency Schedule 1	34
5-23 Corrosion-fatigue crack growth rates in seawater and air as a function of steel strength level for Frequency Schedule 2.....	35
5-24 Corrosion-fatigue crack growth rates in sour brine and air as a function of steel strength level for Frequency Schedule 1	36
5-25 Corrosion-fatigue crack growth rates in sour brine and air as a function of steel strength level for Frequency Schedule 2.....	37

LIST OF FIGURES (*Continued*)

Figure	Page
5-26 Comparison of air fatigue crack growth rate data in the 786 MPa YS Ti-29 with those in the 848 MPa and 945 MPa YS steels.....	39
5-27 Frequency scan results in 786 MPa Ti-29 alloy in sour brine environment.....	42
5-28 Comparison of frequency scan results in 786 MPa Ti-29 alloy in lab air versus sour brine environment.....	42
5-29 Rough fracture surface topography of specimen tested in sour brine environment: a) side view showing out-of-plane cracking, and b) top view showing rough fracture surface topography	43
5-30 Topographic measurements on crack surfaces tested in sour brine environment.....	44
5-31 Topographic measurements on crack surfaces tested in air environment	45
5-32 Corrosion fatigue crack growth rate data for Ti-29 in the sour brine environment; the Ti-29 lab air data from Figure 5-20 are also shown for comparison.....	47
5-33 Comparison of Ti-29 fatigue crack growth rate data in lab air and sour brine (from Figure 5-23) versus those in the 848 MPa YS steel in lab air and sour brine (from Figure 5-15).....	48
6-1 Comparison of air-baseline S-N fatigue data generated at SwRI and at NETL	50
6-2 Comparison of air baseline S-N fatigue data for five steels at various strength levels with the BS 7608, Class B design curve	50
6-3 Comparison of S-N fatigue data in baseline air and seawater with cathodic protection environments	51
6-4 Comparison of S-N fatigue data in baseline air and sour brine environments	52
6-5 Comparison of S-N fatigue data in air, seawater with cathodic protection, and in sour brine environments.....	53

LIST OF FIGURES *(Continued)*

Figure	Page
6-6 Corrosion-fatigue life ratios (FLRs) for 0.17-Hz/1-Hz data in the seawater with cathodic protection environment at various applied stress ranges for different steel strength levels	54
6-7 Corrosion-fatigue life ratios (FLRs) for 0.17 Hz/1 Hz data in the sour brine environment at various applied stress ranges for different steel strength levels.....	55
6-8 Comparison of current high-strength steel data with available X65/X70 data in lab air	56
6-9 Comparison of estimated sour brine fatigue performance of high-strength steel with threaded connections versus sour brine fatigue performance of welded X65/X70 steel	57
6-10 Comparison of S-N data on Ti-29 in sour brine with Ti-29 air data in base metal (BM), electron beam (EB) welds, and tungsten inert gas (TIG) welds from Ref. [13], and Ti-29 weld design curve [12]	59
6-11 Comparison of sour brine and air data on 786 MPa YS Ti-29 alloy (from Figure 6-10) with sour brine and air data in high-strength steels (from Figure 6-4)	60

1.0 INTRODUCTION

Fatigue has become an increasingly significant design consideration in deep-water floating production systems. Due to the highly compliant nature of these structures, fatigue loading is accentuated compared to traditional fixed-bottom platforms. Fatigue loading arises due to vessel motions that are caused by wave and current action. Some of the most fatigue- and fracture-critical components of these systems are the import and export steel catenary risers (SCRs), as well as the top-tension risers (TTRs). Wave motions transmit significant fatigue loading to the SCR, particularly at the touchdown location where the nearly vertical riser curves to join the pipeline or flowline on the ocean floor. In addition, the riser can experience fatigue loading due to vortex-induced vibrations (VIV) caused by currents. These vibrations can occur at any number of locations along the riser length depending on the dynamic response of the structure and the current profile.

This situation has motivated the generation of substantial data on the stress versus cycles to failure (S-N) fatigue performance of girth welds in full-scale risers. These full-scale data capture the residual stress and fatigue size effects, as well as the statistical sampling effects, often associated with large welded structures. However, economics dictate that these full-scale data be generated using resonance fatigue loading at relatively high frequencies of 20 to 30 Hz in a laboratory air environment.

Sour service conditions can arise either due to the nature of the crude production or due to seawater flooding of the reservoir to enhance production yield. Seawater flooding can result in the development of sour conditions that are specific to the details of the reservoir geology.

Consequently, the available full-scale data measured in air are not adequate for design of risers that transport sour production, since sour environments can significantly degrade the fatigue performance compared to that in an air environment. For example, in conventional riser steels, reductions in the fatigue life by factors of 10 to 40 times have been observed in sour brine environments, compared to the fatigue life in laboratory air [1-7]. Moreover, the extent of degradation is dependent on the cyclic loading frequency and typically increases with decreasing cyclic frequency due to the time-dependent interaction of the riser materials and the environment [8-11]. Thus, ideally tests need to be conducted at or near the cyclic loading frequency experienced in the structure – typically 0.01 to 0.33 Hz. Consequently, even if the full-scale tests could somehow be conducted in the sour environment, the 20 to 30 Hz resonance frequency that is used in these tests would preclude the occurrence of a significant environmental degradation of the fatigue performance.

Higher-strength steel risers have been developed recently to meet the requirements of deep water and hostile environments. However, the optimization of alloy composition and microstructure in these steel are primarily based on mechanical properties such as tensile stress-strain curves and fracture toughness, along with limited corrosion testing. Consequently, information is lacking on the corrosion-fatigue performance of these new materials in representative offshore service environments. The goal of this program was to generate corrosion-fatigue data to fill this information gap. This new corrosion-fatigue information will enable more realistic design trade studies by offshore operators, and thereby contribute to

safer, more reliable, and more environmentally sustainable ultra-deepwater oil and gas development in the Gulf of Mexico, as well as around the world.

The research summarized in this report was performed by Southwest Research Institute (SwRI) and sponsored by RPSEA under Project 07121-1403, which was funded by the U.S. Department of Energy (DOE) through the National Energy Technology Laboratory (NETL). As described below, NETL also participated in the research by performing the baseline S-N fatigue experiments in laboratory air.

2.0 RESEARCH OBJECTIVE AND APPROACH

The objective of this research was to quantify the extent to which various offshore environments degrade the fatigue performance of new high-strength materials that are being considered for use in ultra deepwater oil and gas exploration, development and production. A dual approach was utilized in characterizing the corrosion-fatigue performance of these material including: 1) a fracture mechanics based approach using specimens containing existing fatigue pre-cracks in order to quantify the rate of corrosion-fatigue crack growth as a function of the mechanical crack-tip “driving force”, da/dN (ΔK), and 2) a classical S-N fatigue approach that uses smooth (un-cracked) specimens to quantify the total (crack initiation plus propagation) fatigue “life” as a function of applied nominal stress range. In both approaches the key variables were material strength level, cyclic loading frequency, and environmental severity – specifically, seawater (SW) with cathodic “protection” environment representative of that experienced outside the pipe, and a low-oxygen sour brine (SB) environment representative of that experienced inside the pipe.

Characterizing the crack driving force in terms of the range of crack-tip stress intensity factor (ΔK), defined by linear elasticity, enables the resulting da/dN (ΔK) data to be employed in fracture mechanics computations in riser design, fitness-for-service assessments, as well as in determining non-destructive inspection requirements.

A crucial initial step in meeting the project objective was to elucidate the effect of cyclic frequency on corrosion-fatigue crack growth rates in the material-environment systems of interest so that appropriate loading frequencies could be selected for subsequent testing. Optimum frequencies are needed, which will ensure that laboratory-generated data are representative of service loading conditions, while at the same time do not result in impractical test durations. To identify the frequency response of the various material-environment combinations, frequency-scan experiments were conducted at a fixed ΔK and over a range of frequencies using a technique that has previously been described in Refs. [8-10]. These results were then used to formulate a testing strategy for generating corrosion-fatigue crack growth rates over a wide range of ΔK , as well as a wide range of S-N fatigue lives.

3.0 MATERIALS AND ENVIRONMENTS

The materials assessed in the current project included five carbon-manganese steels and a single titanium alloy. Test materials were supplied by three different pipe manufacturers in the form of seamless pipe in various diameters and wall thicknesses summarized in Table 3-1, and shown in Figure 3-1. The average tensile properties based on three replicate measurements on each of these six test materials are summarized in Table 3-2. As can be seen, the average yield strengths of the steels varied by about 27 percent, from a low of 848 MPa to a high of 1080 MPa. Although the tensile ductilities in the steels, as measured by percent elongation and percent reduction in area, tended to decrease with increasing strength level, all of the steels exhibited good ductility. The strength level of the Ti Grade 29 alloy (Ti-29) was comparable to that of the lowest strength steel; however, as expected, the ductility of the Ti-alloy was significantly lower than those of the steels.

TABLE 3-1: Pipe outer diameters and wall thicknesses of the materials examined in the current project.

Material	OD, mm	WT, mm
Steel 1	284.0	33.5
Steel 2	386.0	31.6
Steel 3	245.4	13.8
Steel 4	298.5	27.0
Steel 5	406.4	25.4
Ti-Gr 29	376.3	27.0



FIGURE 3-1: Steel pipes with outer diameters ranging from 284 mm to 406 mm and wall thickness from 13.8 mm to 33.5 mm.

TABLE 3-2: Average tensile properties of the five high-strength steels and one Ti-alloy characterized in the current program, along with corresponding corrosion-fatigue test environments.

Material	Yield Strength (YS) MPa	Ultimate Strength (UTS) MPa	YS/UTS	Percent Elongation	Percent Reduction in Area	Corrosion-Fatigue Environments	
						SW	SB
Steel 1	848	862	0.984	23.7	71.1	X	X
Steel 2	910	993	0.916	19.2	65.8	X	
Steel 3	924	1000	0.924	22.1	62.7	X	X
Steel 4	945	1000	0.945	20.5	66.8	X	X
Steel 5	1080	1160	0.931	18.5	65.4	X	
Ti-Gr 29	786	884	0.889	13.7	26.2		X

The selection of the above materials for assessment in the current project was based on their potential for use in a variety of applications, as indicated in Table 3-3. Since steel pipes with these high strength levels are not currently weldable, their near term application as risers will involve joining using threaded connections. Consequently, all steels were tested in the base metal condition. Although the Ti-29 alloy is weldable, it was also tested in the base metal condition to facilitate comparison with the steels. It should also be pointed out that only three of the five steels assessed here are recommended for use in sour service; thus only these three steels were tested in sour brine environment. Since Ti-29 corrosion-fatigue data in sour environment are limited, testing on this material was performed in sour brine, but not in seawater since ample data in the latter environment are presently available [12-19].

TABLE 3-3: Potential applications of the materials examined in the current project.

Material	YS, MPa	Selection Rationale	Target Applications
Steel 1	848	Highest strength material available with sour resistance	Inner Casing, Sour SCR, Hybrid
Steel 2	910	Highest strength material available for non-sour applications	Outer Casing, Non-Sour SCR/Hybrid
Steel 3	924	Highest strength material available for sour service, but sour resistance unknown	Outer Casing, Sour SCR, Hybrid
Steel 4	945	Highest strength material available for sour service, but sour resistance unknown	Outer/Inner Casing, Sour SCR, Hybrid
Steel 5	1080	Potential for non-sour service, but little data available	Outer Casing, Non-Sour SCR/Hybrid
Ti-Gr 29	786	High-strength Ti-alloy of choice, to compare against steels	Inner Casing, Sour SCR, Hybrids, Dry Tree

Fatigue crack growth rates and S-N fatigue data were generated in three environments: 1) laboratory air, which provided a baseline for comparison of the effects of the more aggressive environments; 2) simulated seawater plus cathodic protection (SW + CP), which was prepared per ASTM D1141 and included cathodic protection at -1050 millivolts (mv) versus the Standard Calomel Electrode, to represent the external environment of the riser; and 3) a sour brine (SB) environment, which was prepared with a production brine with 35 percent hydrogen sulfide (H₂S) and 65 percent carbon dioxide (CO₂) and oxygen below 10 parts per billion (ppb), to represent the internal environment of the riser. The composition of the production brine is given in Table 3-4, and was provided by BP. The environmental chamber for the sour brine environment contained an aqueous volume of 10 liters (L) and a gaseous volume of 2.7 L; based on equilibrium thermodynamic calculations this liquid-to-gaseous volume ratio resulted in an H₂S concentration of 497 parts per million (ppm) in the brine solution and a pH of 4.27 at the test temperature of 25°C.

Table 3-4: Sour brine gas mixture and brine chemistry.

Gas Phase	Brine Chemistry
35 wt.% H ₂ S	33,160 ppm NaCl
65 wt.% CO ₂	286 ppm KCl
	448 ppm CaCl ₂
	127 ppm MgCl ₂
	52 ppm SrCl ₂
	101 ppm NaBr
	53 ppm Na ₂ SO ₄
	979 ppm NaHCO ₃
	1,560 ppm acetic acid

All testing was performed at room temperature since this temperature is believed to give the most conservative corrosion-fatigue performance for the material-environment systems of interest here, which are believed to cause damage to the materials by a hydrogen embrittlement mechanism. Tests were also performed at atmospheric pressure by matching the partial pressures that would occur at elevated pressure. Available data suggest that this approach gives results that are equivalent to those at elevated temperature and pressure.

The brine solution was prepared in a polyethylene tank, prior to being transferred to a stainless steel tank for de-aeration, as shown in Figure 3-2. Also shown in Figure 3-2 is the Orbisphere instrument used for monitoring the oxygen concentration during de-aeration. The brine solution was de-aerated prior to introduction of the H₂S gas to achieve the oxygen

concentration of less than 10 ppb. No monitoring of the oxygen concentration was performed during the actual test due to the oxygen sensor's inability to withstand chemical attack from the H₂S test gas. However, prior testing with monitored for oxygen level in a brine solution containing CO₂ (without H₂S) demonstrated that the level remained stable at well below 10 ppb over a one-month period.

Following de-aeration, the brine solution was introduced into the test chamber and the gas mixture was injected at 100 milliliters per minute (ml/min) for the first hour to saturate the exposed specimen surface and chamber walls. After the first hour, the flow rate was reduced to 20 ml/min and held at this level for the remainder of the fatigue test.



FIGURE 3-2: Polyethylene brine make-up tank and oxygen purging tank with Orbisphere oxygen meter and flow loop control system used to start the sour brine tests.

4.0 EXPERIMENTAL PROCEDURES

The experimental procedures employed in both the fatigue crack growth rate testing and S-N fatigue life testing are summarized in this section, and where appropriate background references on these procedures are cited. Procedures for safely containing and controlling the sour brine test environment are also briefly described.

4.1 Fatigue Crack Growth Rate Testing

Two types of fatigue crack growth rate tests were utilized. First, frequency-scan experiments to assess fatigue crack growth rates over a range of cyclic loading frequencies from 0.01 Hz to 10 Hz under a constant crack “driving force” ($\Delta K = 22 \text{ MPa}\sqrt{\text{m}}$, and $R = \text{minimum load/maximum load} = 0.5$). These loading values were selected to interrogate the material-environment interaction in the regime where crack growth rates become independent of ΔK and therefore are controlled by underlying rate controlling processes (surface reactions and/or hydrogen diffusion) since it is these processes that govern the observed frequency dependence. The relatively high ΔK and R values also served to minimize the extent of crack closure, which can confound the interpretation of the frequency dependence. The goal of these tests was to determine a saturation frequency below which the corrosion-fatigue crack growth per cycle no longer increases with decreasing frequency.

Next, fatigue crack growth rates were measured as a function of ΔK to generate data that can be used in engineering-critical assessments. These tests were conducted at constant- K_{max} and decreasing- ΔK to simulate the riser loading which includes a nearly steady mean stress (or K_{max}), and a variable ΔK . This loading corresponds to a decreasing ΔK throughout the test, thereby resulting in high fatigue crack growth rates initially and decreasing rates as the crack grows toward a threshold stress intensity factor range, ΔK_{th} . Under these loading conditions, the stress ratio ($R = \text{minimum load/maximum load}$) is initially low (near 0.1) and increases to a high value (near 0.9) at the end of the test as the applied ΔK approaches ΔK_{th} . During the constant- K_{max} testing, there was also a frequency schedule implemented that utilized three test frequencies. A summary of the frequency schedule is provided and discussed in Section 5.3. The rate of decrease in ΔK was controlled according to the ΔK -gradient procedure in ASTM E647 [20], to ensure a smooth decrease in the crack-tip plastic zone, thereby minimizing transient crack growth rates, using a normalized K-gradient parameter $C = -0.23 \text{ mm}^{-1}$, where C is defined as:

$$C = \left(\frac{1}{K} \right) \cdot \left(\frac{dK}{da} \right) \quad (1)$$

All fatigue crack growth tests were performed using the compact-type fracture mechanics specimen shown in Figure 4-1, which were pre-cracked in accord with ASTM E647 prior to testing. Specimens were extracted from full-scale pipe in the load limiting (L-C) orientation, which corresponds to the dominant cracking plane for risers subjected to service loading.

Crack extension was measured as a function of applied loading cycles during the test using a current switching-direct current potential drop (PD) procedure. Dual-voltage probes were utilized to minimize the effect of ambient temperature variations on the PD-measured crack length. For the frequency-scan testing at a constant- ΔK of 22.0 MPa \sqrt{m} , the PD-inferred crack length was fed into an automated, computer-controlled system that enabled the applied loading range to be decreased as the crack extended to maintain the constant- ΔK . This same system was used to automatically decrease ΔK in the fatigue crack growth rate versus ΔK testing, which was performed at a constant K_{max} of 48.8 MPa \sqrt{m} .

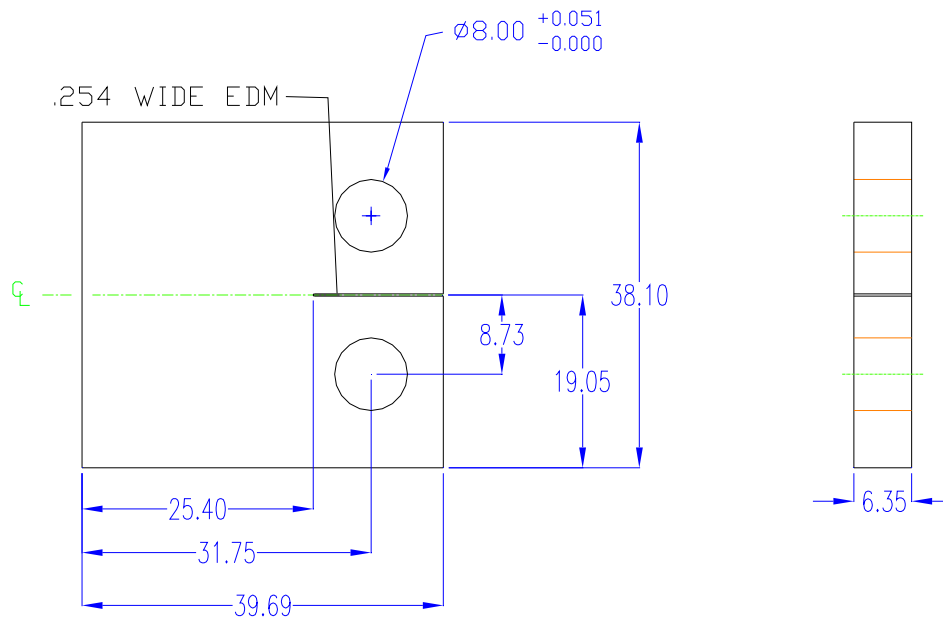


FIGURE 4-1: Compact-type specimen used for fatigue crack growth rate testing (units in mm).

4.2 S-N Fatigue Testing

Full-thickness strip S-N fatigue specimens were extracted from the pipes as illustrated in Figure 4-2. The number of specimens that could be excised from a given pipe segment varied between three-to-five, depending on the inner pipe-diameter (ID). The specimens were 762 mm in length with thickness equal to the pipe thickness, and a reduced gauge section whose width was equal to the thickness, and which ranged from 14 mm to 33 mm. This was done to limit the load capacity required for fatigue testing in these high-strength steels – particularly for the baseline testing in air where the fatigue endurance limit is typically proportional to the ultimate strength of the steel. The use of a specimen gauge section of width equal to the pipe thickness is not advisable when fatigue testing welded pipe material, in which case it is important to sample an adequate length of weld in order to generate representative fatigue

properties. However, in the present test this was not an important consideration since all tests were on base material – that is, without welds. As discussed later, the fatigue results support the validity of this approach.

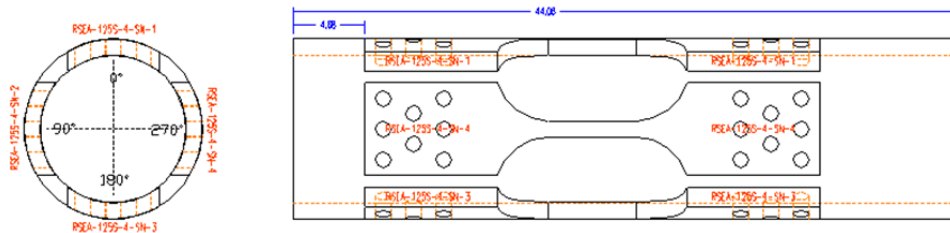


FIGURE 4-2: Typical S-N fatigue strip specimen and example cutting plan for specimen removal from the pipe; depending on pipe diameter, three-to-five specimens were removed from each pipe segment.

Since the S-N specimens extracted from pipe were full-thickness, they had curved ID and OD surfaces. Thus, special brass grip inserts were manufactured to conform to the pipe and also provide a flat grip area for clamping. A photograph of the concave and convex brass inserts shown with a test specimen is provided in Figure 4-3.

The S-N fatigue data were generated using constant-amplitude applied stress ranges from 900 MPa to about 75 MPa. All tests were performed at a stress ratio ($R = \text{minimum stress}/\text{maximum stress}$) of 0.1. These stresses resulted in fatigue lives from 5,000 cycles to 10 million cycles.

Fatigue testing in the air environment used relatively high cyclic loading frequencies (2-8 Hz) to expedite the data generation. This is an acceptable practice since air is a relatively benign environment for these steels; thus fatigue lives are insensitive to cyclic loading frequency. As previously discussed, tests conducted in the seawater plus cathodic protection and in the sour brine environments used frequencies of 0.01 Hz, 0.17 Hz, or 1 Hz, depending on the applied stress and life regime. Specifically, the life regimes for the different frequencies were 0.01 Hz: 5,000 to 60,000 cycles; 0.17 Hz: 26,000 to 1,600,000 cycles, and 1 Hz: 165,000 to 10,000,000 cycles. Tests that survived 10,000,000 cycles without failure were defined as “runouts.” These combinations of cyclic frequencies and fatigue lives resulted in individual test durations from one week to nearly six months.

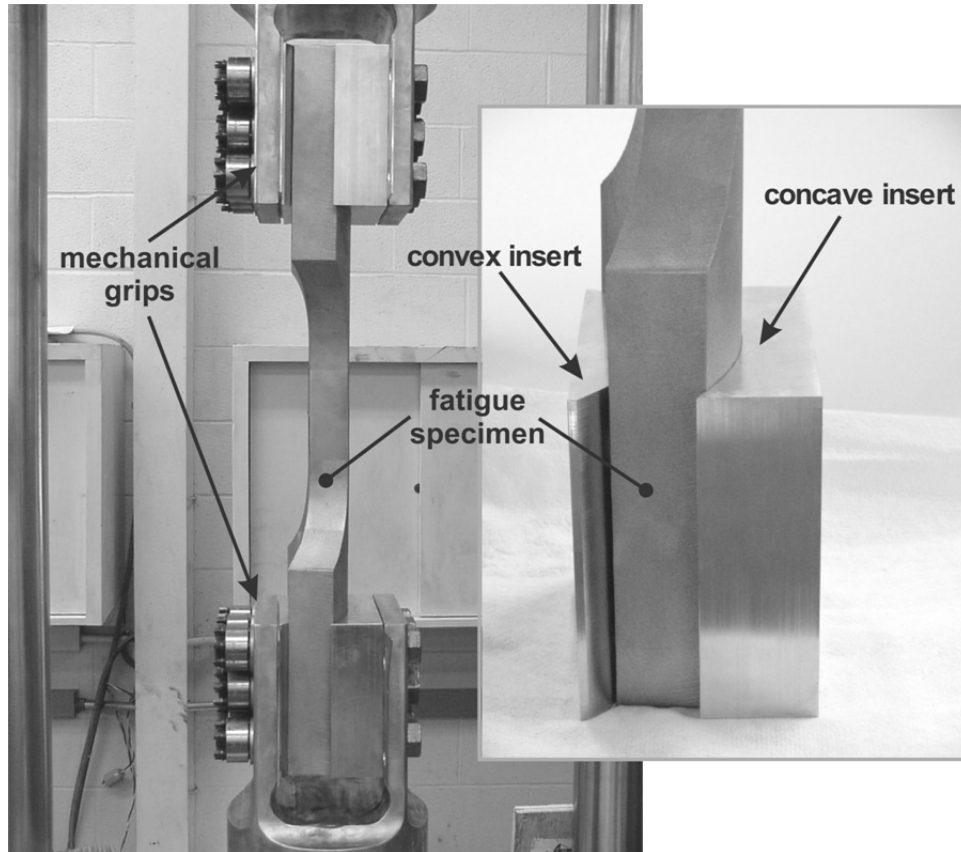


FIGURE 4-3: Photograph of convex and concave brass inserts used in the grips to apply a uniform clamping force across the curved section of the strip fatigue S-N specimens.

4.3 Test Environment Containment, Control and Safety Considerations

Safety considerations were of prime importance due to the potentially harmful nature of the sour test gas (H_2S), and the corrosive characteristics of the test solution (acid brine). Thus, corrosion-fatigue testing in the sour brine environment was conducted in a specially-designed facility consisting of environmental chambers, a gas delivery and control system, and a safety system. The safety system contained sensors and alarms to provide automatic shutdown of the gas supply system in the event of a test gas leak. For both safety, as well as to maintain low oxygen levels (less than 10 ppb), the sour brine containment system consisted of a triple containment, which was comprised of a primary chamber, a shroud enclosure, and an exhaust enclosure, as shown in Figure 4-4 for S-N corrosion-fatigue testing. Fatigue crack growth rate testing was conducted in a similar triple-containment chamber; however, the chamber size was smaller to accommodate the smaller size of the crack growth specimen.

The innermost primary chamber contained the specimen and the sour brine test solution, and was constructed of a nickel-based alloy for corrosion resistance. This chamber was

electrically isolated from the specimen to prevent galvanic corrosion of the specimen. The shroud provided secondary containment and was constructed of a 10-mil thick transparent, flexible polymeric tube connected to two aluminum flanges attached to the upper and lower specimen grips. The shroud was filled with flowing nitrogen (N_2) gas to provide a further barrier to diffusion of oxygen into the primary chamber during testing. The shroud also served as a barrier to contain any sour gas that might escape from the primary chamber, should the primary chamber sealing system fail during testing. For this reason, the shroud also housed an H_2S detector, which was connected to an alarm/shutdown panel that was used to stop the flow of the test gas into the primary chamber in the event of a primary chamber leak.

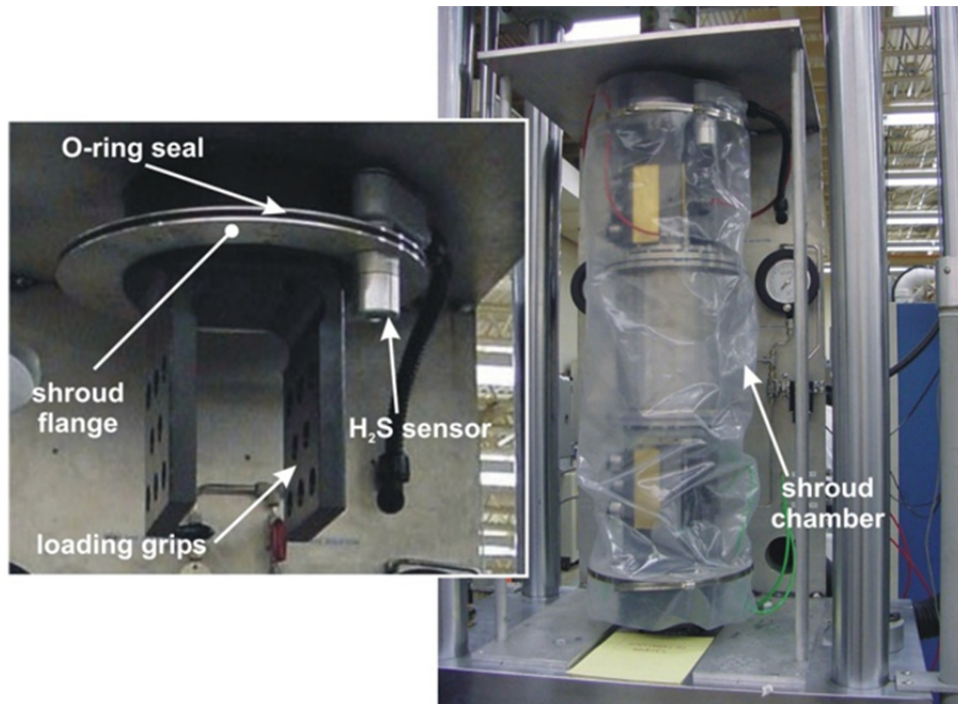


FIGURE 4-4: Triple-containment chamber components for S-N fatigue testing in sour brine environment.

The third barrier consisted of an acrylic and aluminum exhaust enclosure that surrounded the central portion of the test frame. This enclosure was connected to a roof-mounted duct system that provided continuous evacuation of the enclosure during sour gas testing. The enclosure also served as a platform to mount hardware associated with the test gas and test solution delivery lines, flow meters and valves. The flow rate of each gas stream within the test chamber was controlled by means of rotameters, with the maximum flow through each of approximately 125 ml/min at a supply pressure of 15 psig. The gas leaving the test chamber passed through $\frac{3}{4}$ -inch PVC tubing in the hydraulic system trenching to a gas scrubber outside

the lab, which contained an aqueous caustic solution (NaOH) to reduce the H₂S gas to a non-toxic sulfide compound.

The gas exiting the scrubber passed through a bed of activated charcoal to remove trace amounts of H₂S, and was then evacuated through a roof-mounted ventilation system and stack. Solenoid valves were located within each test frame enclosure and on the gas delivery manifold outside of the test laboratory. The monitor/alarm panel automatically controlled the operation of each flow shutoff valve. Additionally, the system is designed to be failsafe in the event of loss of air supply, or control panel power to the Uninterruptable Power Supply (UPS).

In contrast, the environmental containment for the corrosion-fatigue testing in the seawater environment was much simpler than that described above for the sour brine environment. Specifically, seawater testing was conducted in a polymeric chamber that was open to the laboratory air, since it was designed to simulate seawater near the surface and in the splash zone, where high fatigue bending stresses are typically experienced in risers during service. For the steel specimens tested in the seawater environment, a potentiostat was implemented to provide the cathodic protection previously detailed.

5.0 CORROSION-FATIGUE CRACK GROWTH RATE RESULTS AND DISCUSSION

This section summarizes the corrosion-fatigue performance of all six test materials in terms of fracture mechanics-based crack growth rate data obtained in the baselines laboratory air (Air) environment, as well as in the seawater plus cathodic protection (SW + CP) environment, and sour brine (SB) environment. For each of these environments results are initially presented and compared for the five high-strength steels, then for the Ti-29 alloy. Results are also discussed and compared with relevant literature results, and where appropriate, interpreted in terms of underlying mechanisms.

5.1 Steel Corrosion-Fatigue Crack Growth Rates

This subsection presents the corrosion-fatigue crack growth rates for all five steels examined in the current project. First the baseline crack growth rate data are presented in the laboratory-air environment, followed by the frequency-scan results in SW + CP and SB, and finally the corrosion-fatigue crack growth rate data versus ΔK in the SW and SB environments.

5.1.1 Steel Fatigue Crack Growth Rates in Lab Air

As mentioned previously, the fatigue crack growth rate behavior of the steels in laboratory air are significant in that they provide a baseline for comparison of the potential degradation of fatigue behavior of these materials in seawater and sour brine environments to be discussed in subsequent section of this report.

Results for the five steels tested in laboratory air are summarized in Figure 5-1. These data include two replicate tests at each steel strength level, and can be seen to exhibit very good

reproducibility. The fatigue crack growth rates also exhibit a slight tendency to increase with increasing yield strength (YS). This trend could be due to either or both: 1) the decrease in ductility with increasing material strength level and/or 2) a slight increase in the materials' sensitivity to the moisture in the lab air environment with increasing material strength level.

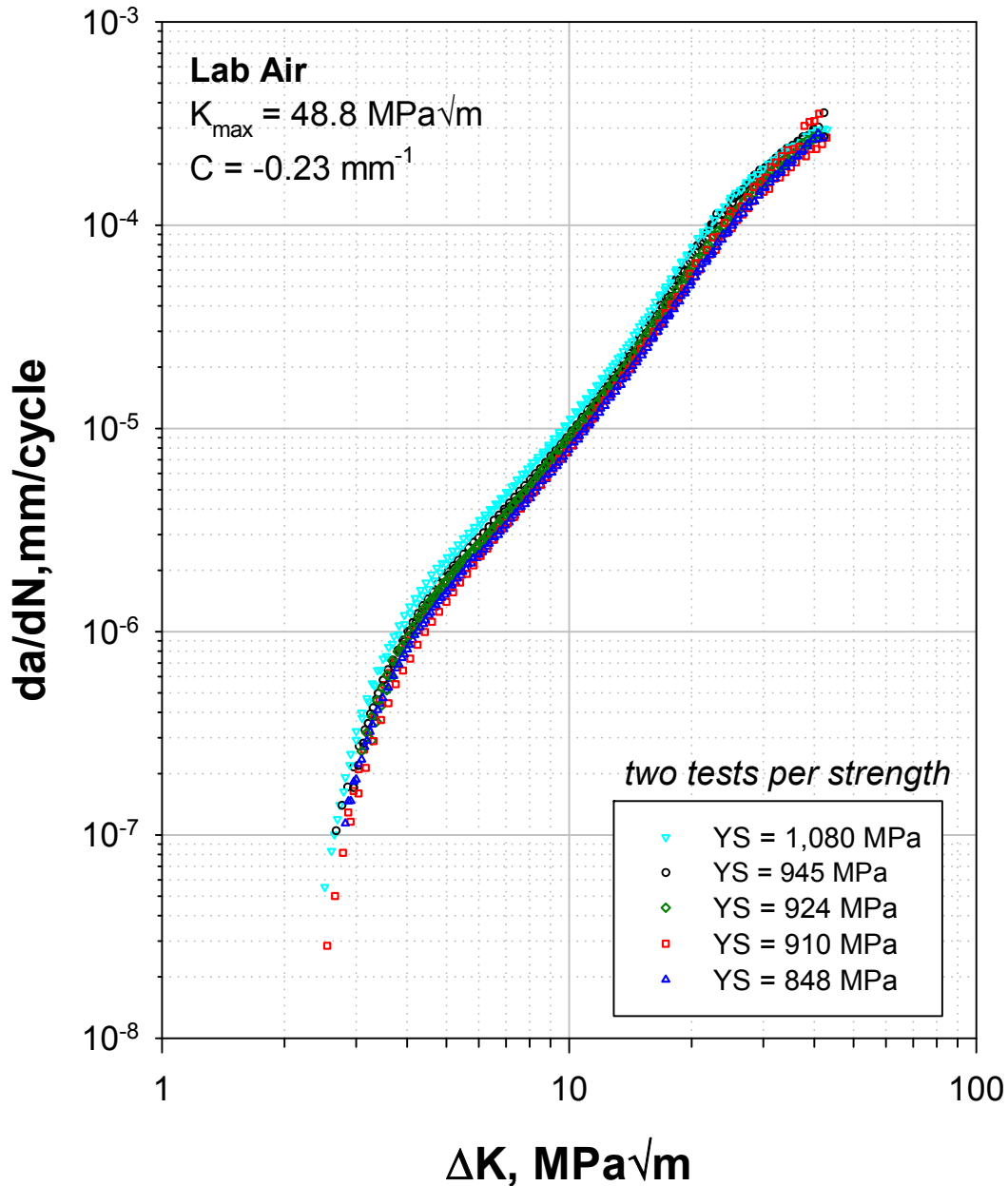


FIGURE 5-1: Summary of fatigue crack growth rate data for five different steels in lab air showing trend, at a given ΔK , of increasing rates with increasing material yield strength (YS).

5.1.2 Effect of Loading Frequency on Steel Corrosion-Fatigue Crack Growth Rates

The frequency-scan results for the seawater environment are summarized in Figures 5-2 through 5-6, which show the corrosion-fatigue crack growth rates at a constant $\Delta K = 22 \text{ MPa}\sqrt{\text{m}}$ and $R = 0.5$, as a function of crack size (a) normalized by the test specimen width (W) for varying cyclic frequencies. As indicated in the figures, the tests start and end in lab air at 10 Hz to provide a baseline for comparison of results in seawater. Starting from the smallest normalized crack sizes at the left of the figures, the frequency in seawater is then stepped down from 10 Hz, 1 Hz, 0.33 Hz, 0.1 Hz, and 0.01 Hz before stepping back up to 10 Hz in inverse manner. The increment of crack growth during each frequency was selected to allow time for the corresponding corrosion-fatigue crack growth rates to stabilize to a steady-state value, which it did for most of the steps. These results exhibit the classical corrosion-fatigue frequency effect – that is, increasing growth rates as the frequency is decreased. It is interesting to note that in this seawater environment the rates during the increasing frequency portion of the test are systematically higher than those from the decreasing frequency portion of the test.

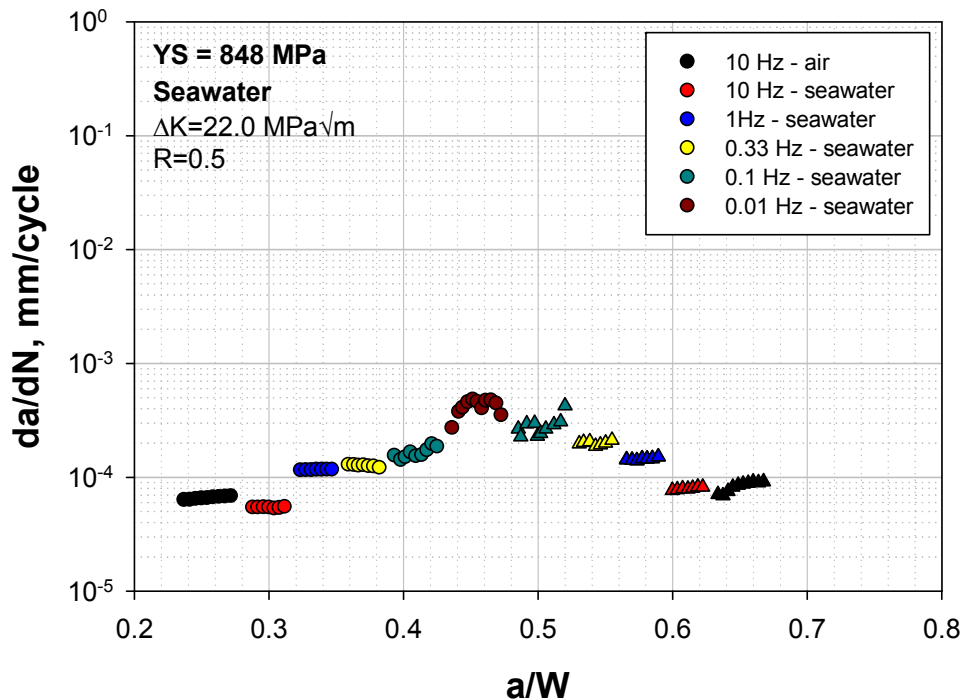


FIGURE 5-2: Frequency-scan results in 848 MPa YS steel in seawater environment. (Circles indicate decreasing-frequency segment of test, while triangles indicate increasing-frequency portion of test; colors indicate frequency value as shown in legend).

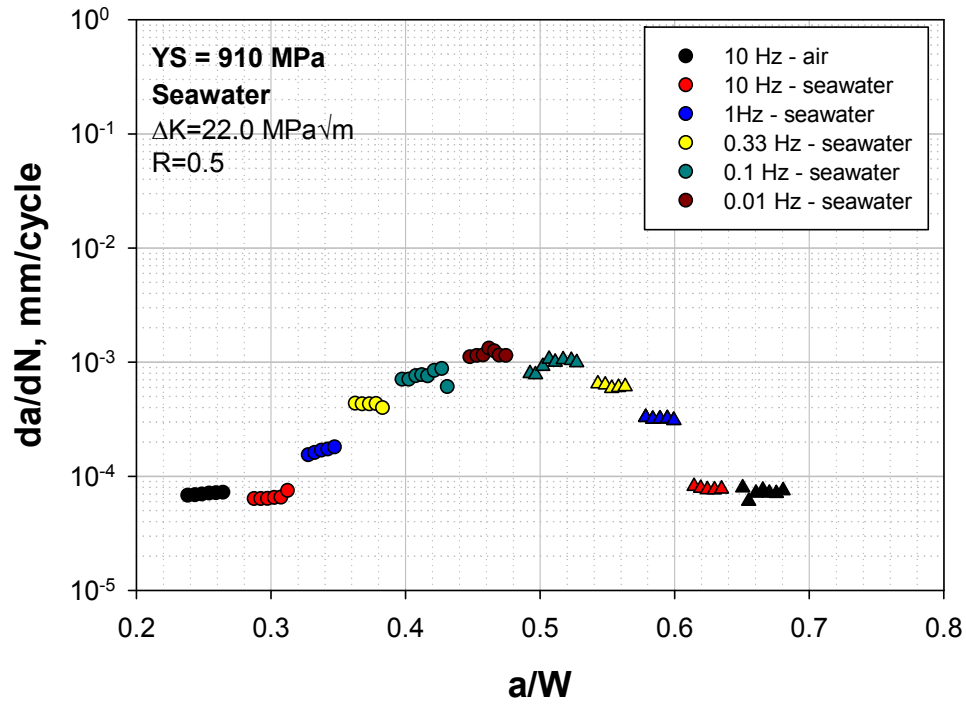


FIGURE 5-3: Frequency-scan results in 910 MPa YS steel in seawater environment.

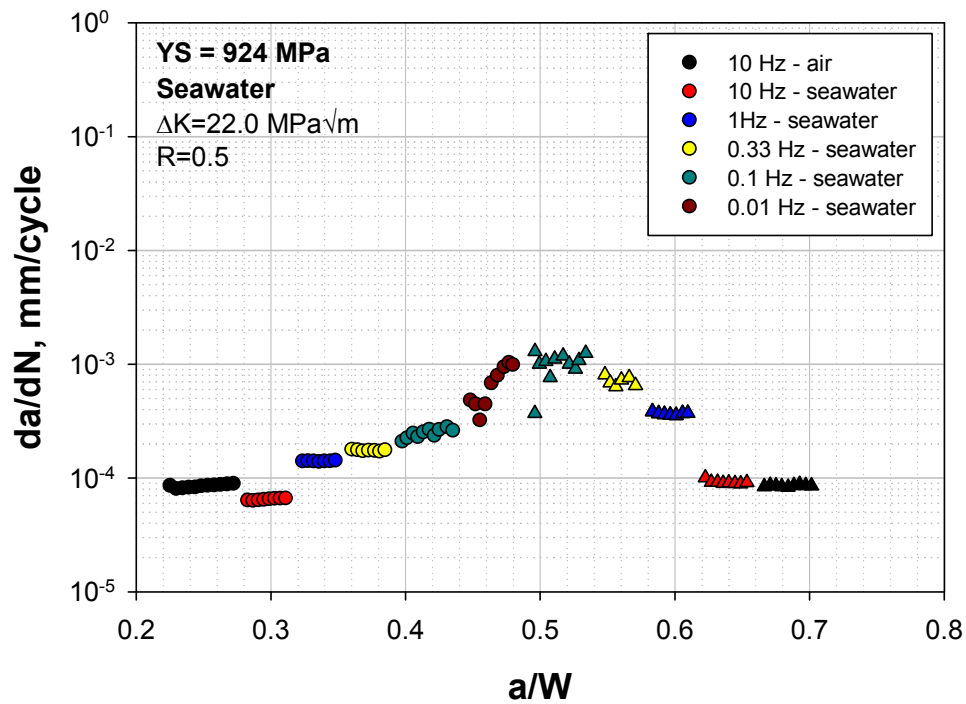


FIGURE 5-4: Frequency-scan results in 924 MPa YS steel in seawater environment.

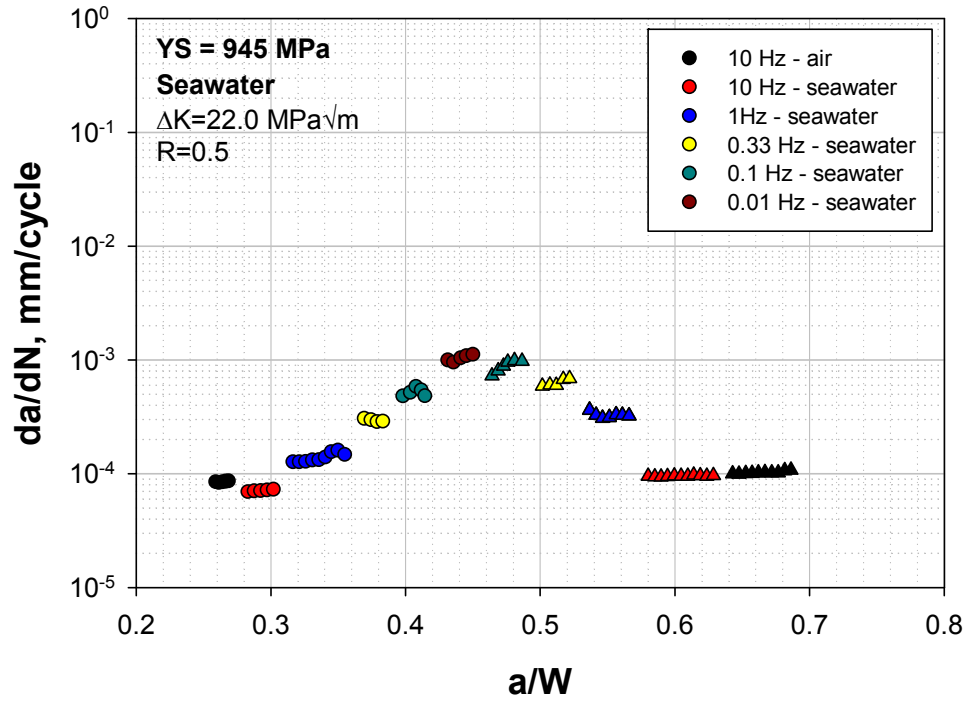


FIGURE 5-5: Frequency-scan results in 945 MPa YS steel in seawater environment.

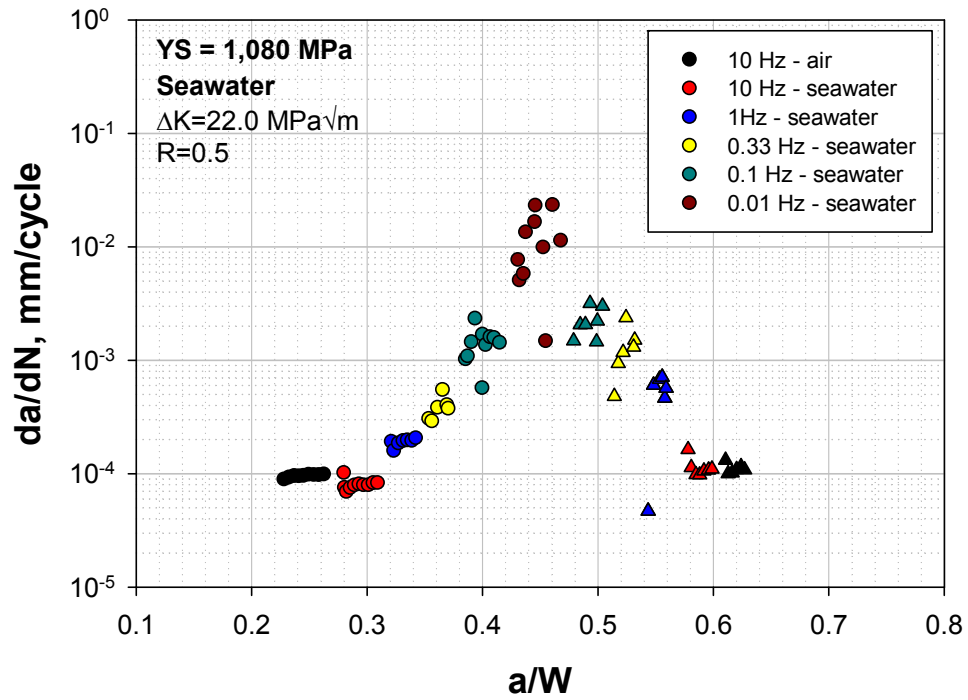


FIGURE 5-6: Frequency-scan results in 1080 MPa YS steel in seawater environment.

It is significant to note that as material YS is increased in the frequency-scan results in Figures 5-3 to Figure 5-6, respectively, the peak corrosion-fatigue crack growth rate, as well as the sharpness of the peak increases. The above trend is clearer in Figure 5-7, which shows the average rates from each of the frequency-steps in seawater as a function of frequency. As can be seen, the rates at all frequencies increase with increasing strength level. Moreover, the rates for the two different steels having very similar strength levels exhibit similar frequency responses. Thus, material strength level is a dominant variable controlling the corrosion-fatigue sensitivity in seawater.

It is also significant to note that at lower frequencies the rates in certain of the steels approach a plateau, thereby suggesting saturation in the frequency dependence at the lower frequencies. However, this is not the case for the highest strength material, which actually exhibits an increase in the slope of the curve upon going from 0.1 Hz to 0.01 Hz.

Figures 5-8 through 5-10 summarize the frequency-scan results in the sour brine environment for materials with strength level 848 MPa, 924 MPa, and 945 MPa, respectively. Similar to the case of the seawater environment, the same general trend is exhibited in sour brine – specifically, increasing corrosion-fatigue crack growth rates with increasing material strength level. This trend is also evident in the summary of results in sour brine for the materials with different strength levels in Figure 5-11.

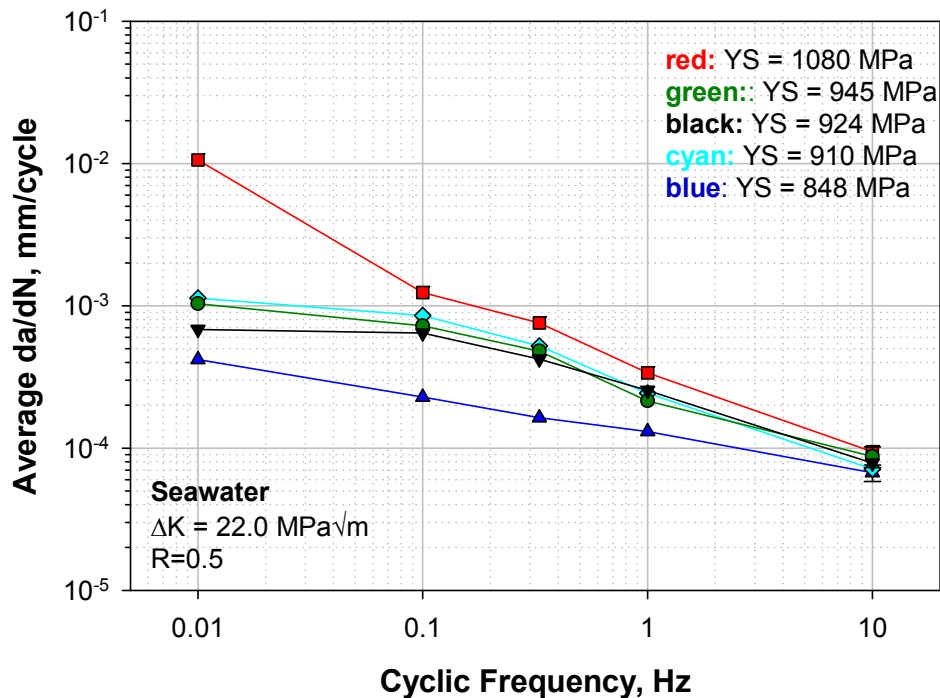


FIGURE 5-7: Summary of frequency response in seawater versus steel yield strength (YS).

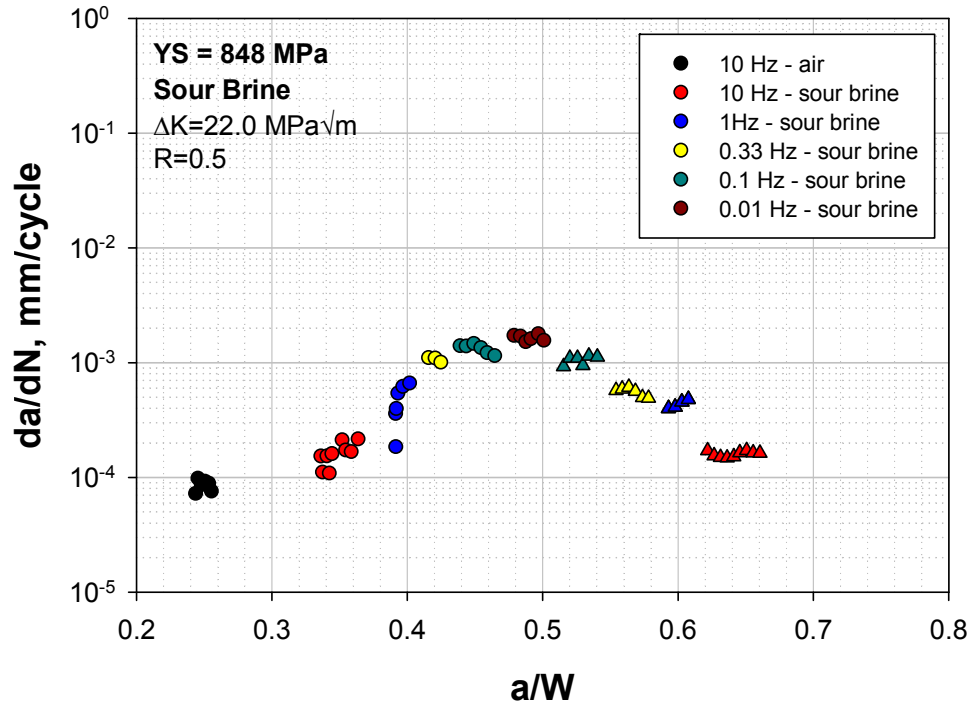


FIGURE 5-8: Frequency-scan results in 848 MPa YS steel in sour brine environment.

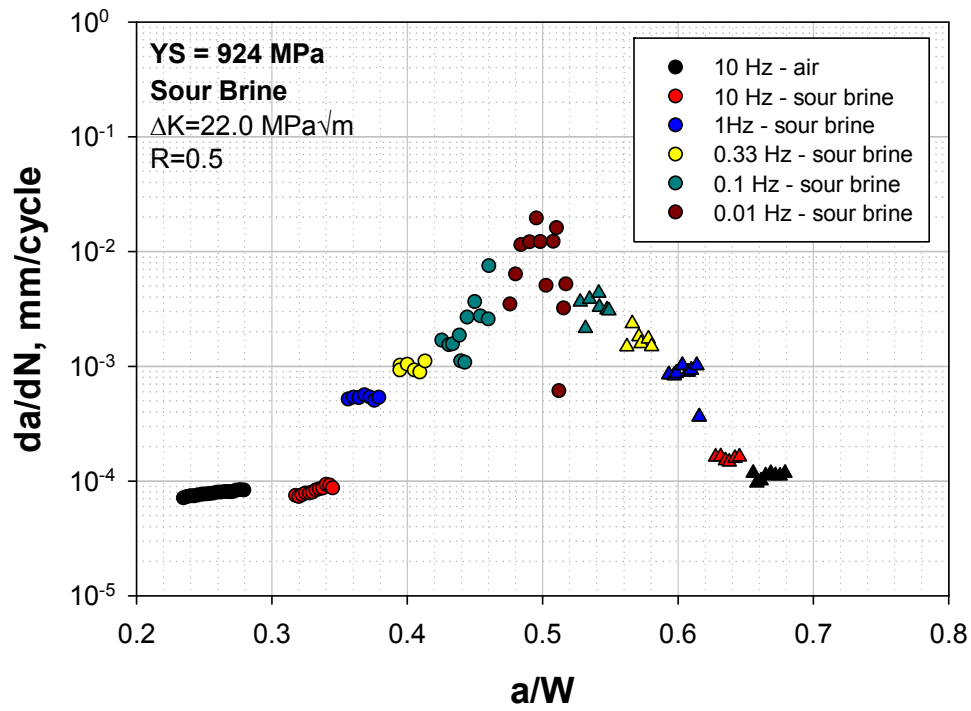


FIGURE 5-9: Frequency-scan results in 924 MPa YS steel in sour brine environment.

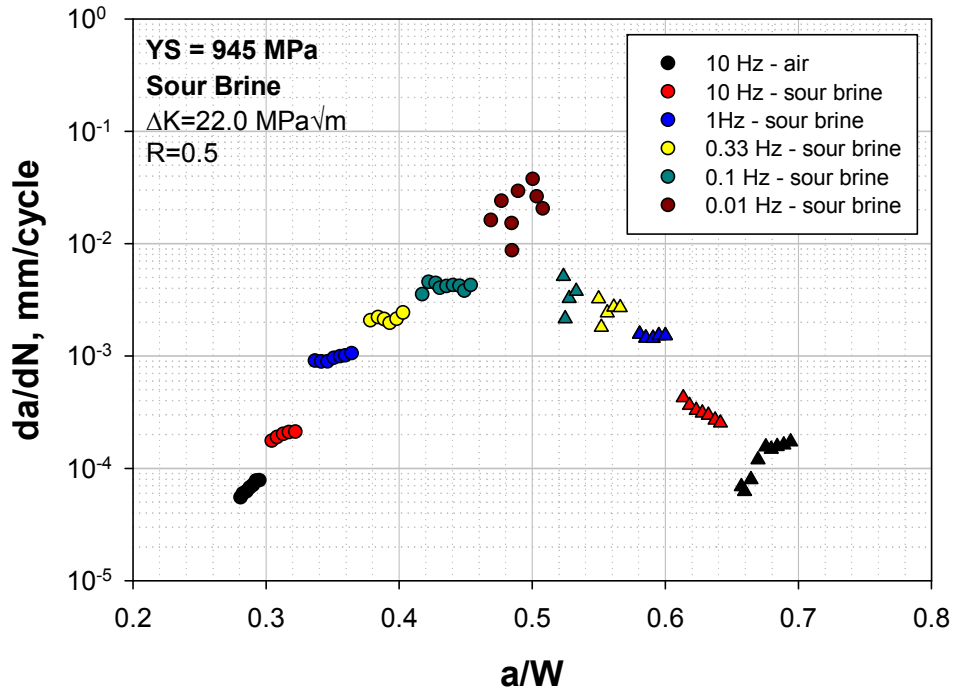


FIGURE 5-10: Frequency-scan results in 945 MPa YS steel in sour brine environment.

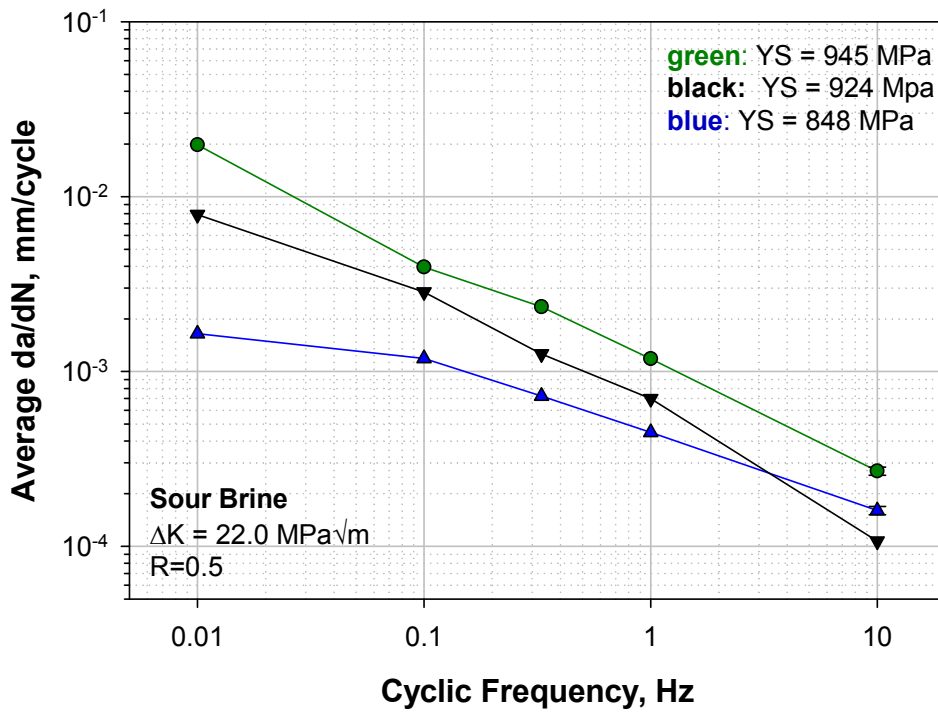


FIGURE 5-11: Summary of frequency response in sour brine versus steel yield strength (YS).

Equally important is the fact that for a given material strength level the rates in the sour brine environment are significantly higher than those in the seawater environment – as can be seen by comparing results in Figures 5-2 through 5-7 with those in Figures 5-8 through 5-11. This trend is also clearly evident in Table 5-1, which summarizes the maximum rates, observed at the lowest frequency of 0.01 Hz, in the frequency-scan tests for the various material-environment combinations. As can be seen, the rates in the sour brine (SB) environment are significantly higher than those in the seawater plus cathodic protection (SW+CP) environment. Although the enhanced rates in both environments are believed to be controlled by the availability of atomic hydrogen, this concentration is expected to be greater for the SB environment because H₂S is known to poison the hydrogen recombination reaction, thereby resulting in a higher concentration of atomic hydrogen at the highly strained crack-tip.

TABLE 5-1: Influence of steel strength level on nominal corrosion-fatigue crack growth rates in offshore environments (at $\Delta K= 22 \text{ MPa}\sqrt{\text{m}}$, $R = 0.5$, and frequency = 0.01 Hz) relative to the baseline rate in lab air.

Environment	Yield Strength, MPa				
	848	910	924	945	1080
Sour Brine	24X	–	100X	200X	–
Seawater	6X	15X	15X	15X	100X

5.1.3 Effect of Hydrogen Source on Frequency Response

It was previously hypothesized that this lack of symmetry in the frequency response may be due to a systematic change in the local crack-tip environment [21]. The change in the occluded environment could occur since the occluded environment is believed to be controlled by the balance between the rate of creation of reactive surface and/or reaction kinetics at the crack-tip versus the rate of transport of reactants and product to and from the crack-tip. Thus any change in the reaction kinetics over time would result in a change in the occluded environment. An alternative cause of this lack of symmetry may be caused by the existence of two sources of damaging hydrogen: 1) production of atomic hydrogen by surface reaction at the fresh surface formed due to the high strain at the crack tip, followed by diffusion of this atomic hydrogen to the fracture process zone just below the crack tip where maximum hydrostatic stresses occur; and 2) production of atomic hydrogen through surface reaction on all external surfaces of the specimen followed by diffusion within the bulk of the specimen far ahead of the crack; this bulk hydrogen would subsequently be attracted to the moving crack-tip by hydrostatic stress field as the moving crack-tip approaches. Thus, the hydrogen supplied through the crack-tip would be expected to dominate the rates observed during the early portion of the frequency scan test, while the bulk hydrogen would eventually add to the hydrogen available to the crack tip and increase the rates during the later portion of the test, after there is adequate time for hydrogen to permeate the bulk of the specimen. Recent experiments with coated and uncoated X-65 steels tend to support the concept of two sources

of hydrogen during corrosion-fatigue crack growth in steels exposed to hydrogenous environments [22, 23]. The above results on high-strength steels are consistent with these literature results. Moreover, since the magnitude of the asymmetry in rates observed in the frequency scan results is between a factor of two, these results suggest that the contribution of both hydrogen sources to crack growth is approximately equal.

It is interesting to note that the rates observed in the SB environment between the first segment of these tests – where the frequency was decreasing, and the second segment of the test – where the frequency was increasing, are not as asymmetric as those in the SW+CP environment previously discussed. This may be due to the fact that the hydrogen source from external surfaces, which provides hydrogen to the bulk material, is limited by the fact that these surfaces are covered with iron sulfide films that serve to block the permeation of hydrogen into the material, except at the crack-tip where the highly strained material ruptures these films.

5.1.4 *Effect of Frequency Schedule on Steel Corrosion-Fatigue Crack Growth Rates vs. ΔK*

Since the frequency-scan results described above did not exhibit a unique frequency below which the rates no longer increased with decreasing frequency, it was decided to conduct subsequent $da/dN(\Delta K)$ testing using variable frequencies, based on considerations of the anticipated structural loading frequencies, as well as the test frequencies that would result in practical test durations. This approach is analogous to the variable frequency testing approach that has recently been employed in S-N fatigue testing in sour brine environments.

As described previously in the experimental procedure section, all $da/dN(\Delta K)$ tests were performed at a constant K_{max} of 48.8 MPa \sqrt{m} with decreasing values of ΔK using the smooth gradient parameter $C = -0.23 \text{ mm}^{-1}$ as defined by Eq. [1] from ASTM E647 [20].

Corrosion-fatigue crack growth rates versus ΔK curves in the seawater environment, which were based on this variable-frequency approach, are summarized in Figures 5-12 through 5-15 for steels with strength levels of 848 MPa, 945 MPa, and 1080 MPa, respectively. The variable frequencies employed are indicated to the right side of the data in these figures. Specifically, at high growth rates and ΔK values, a relatively low frequency of 0.01 Hz was used to simulate the very low frequencies associated with thermal fatigue due to starting and stopping the flow of production fluids; at intermediate growth rates and ΔK values, the predominant wave loading frequency of 0.17 Hz was used to simulate the structural response associated with hull motions and vortex induced vibrations (VIVs); and finally, at very low growth rates and ΔK values, a frequency of 1 Hz was pragmatically chosen to facilitate data generation in practical test durations. Within this general testing scheme two different frequency schedules were used, the difference being the rate at which the frequency was switched from 0.17 Hz to 1 Hz, as indicated by the different lengths of blue and green arrows to the right of the data in Figures 5-12 through 5-15.

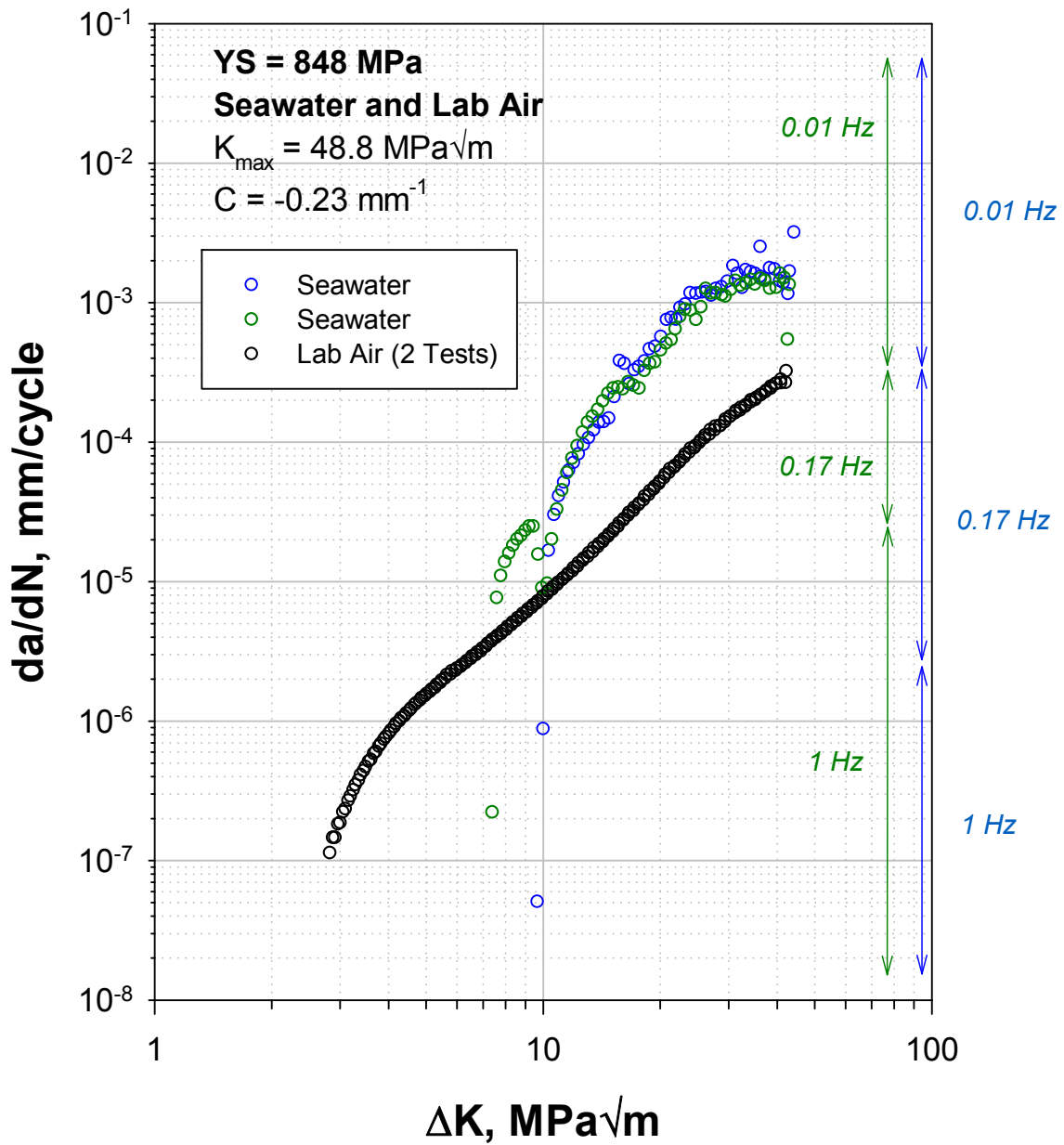


FIGURE 5-12: The effect of frequency schedule on the seawater corrosion-fatigue crack growth rates in the 848 MPa YS steel.

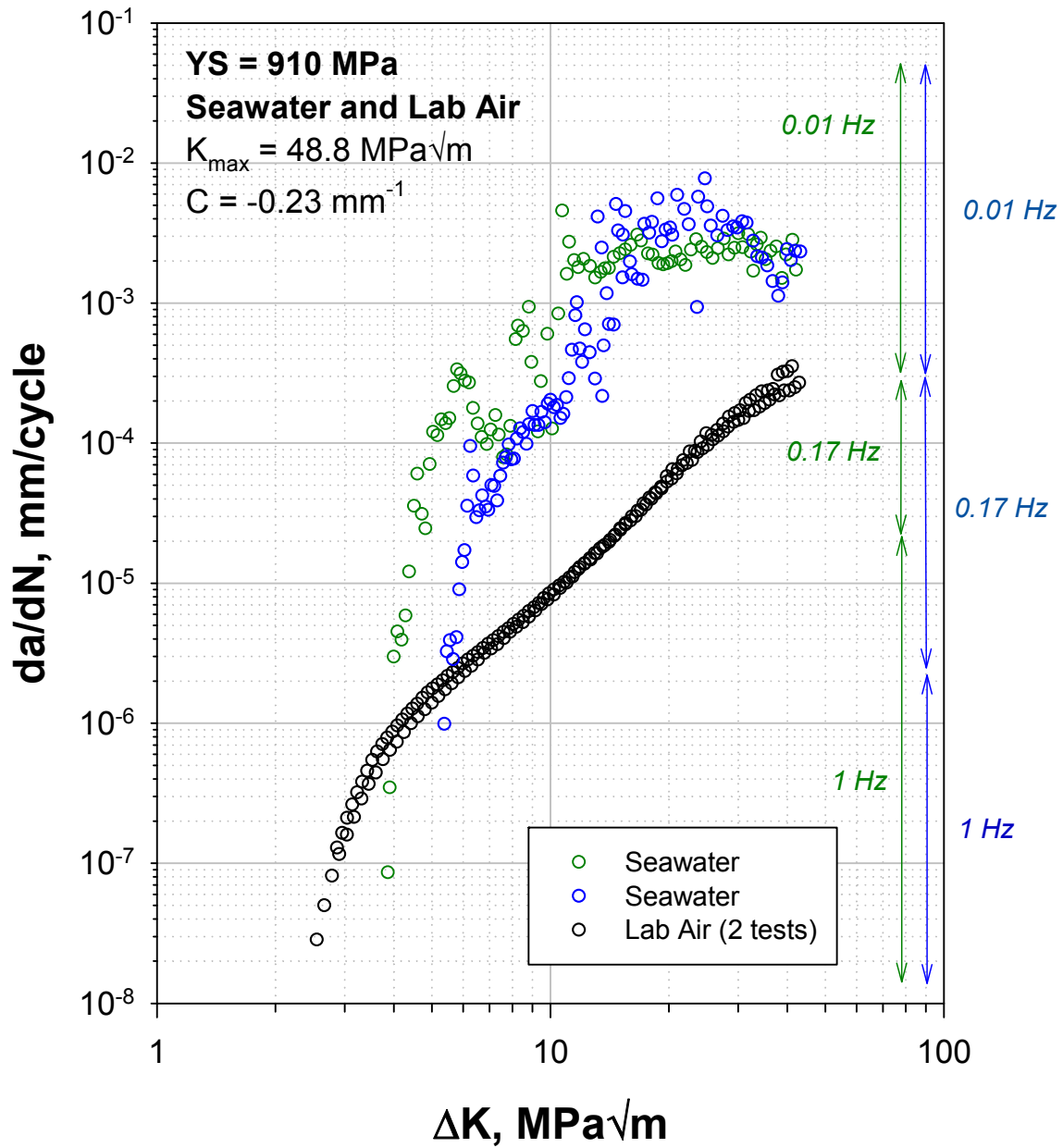


FIGURE 5-13: The effect of frequency schedule on seawater corrosion-fatigue crack growth rates in the 910 MPa YS steel.

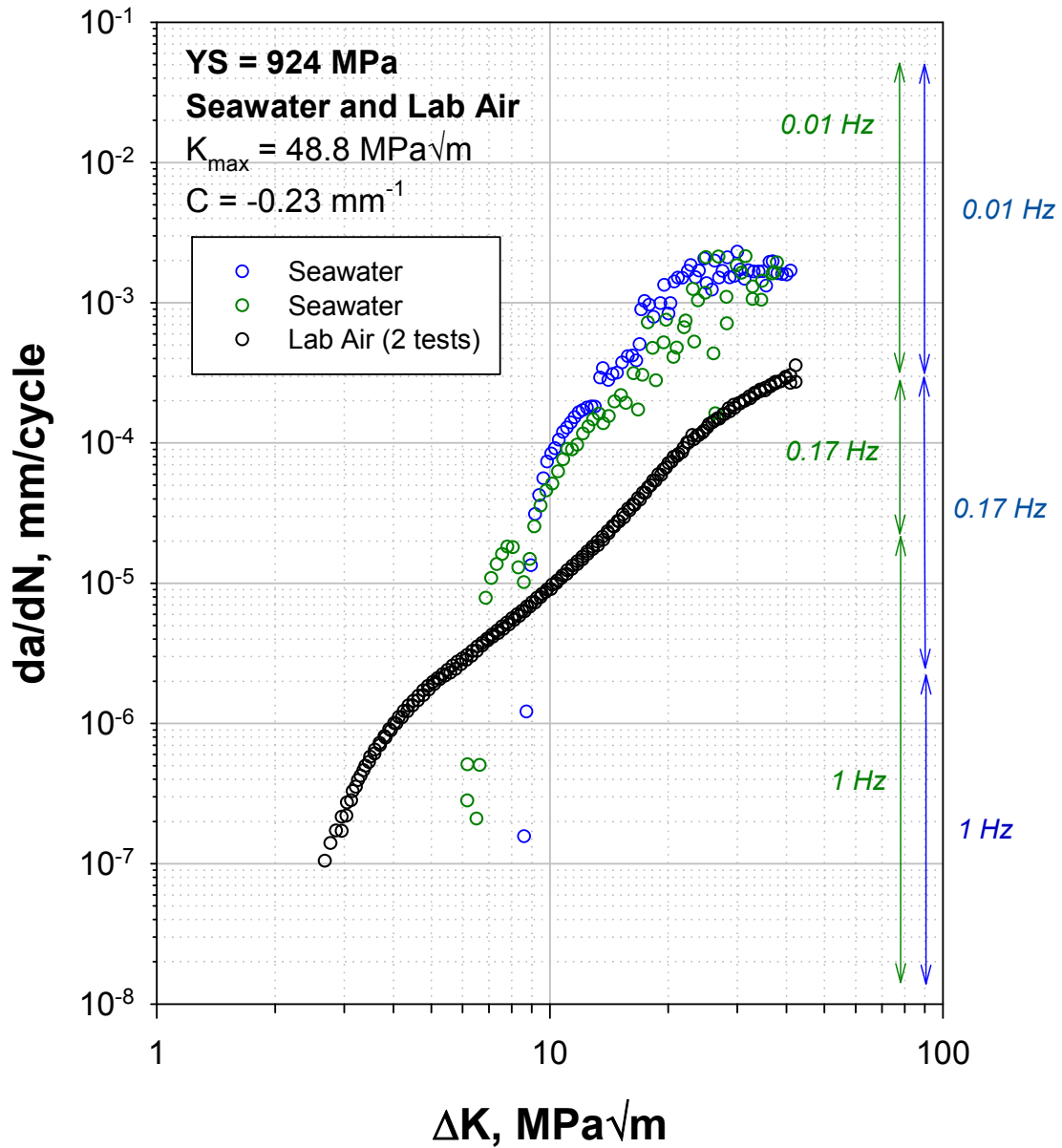


FIGURE 5-14: The effect of frequency schedule on the seawater corrosion-fatigue crack growth rates in the 924 MPa YS steel.

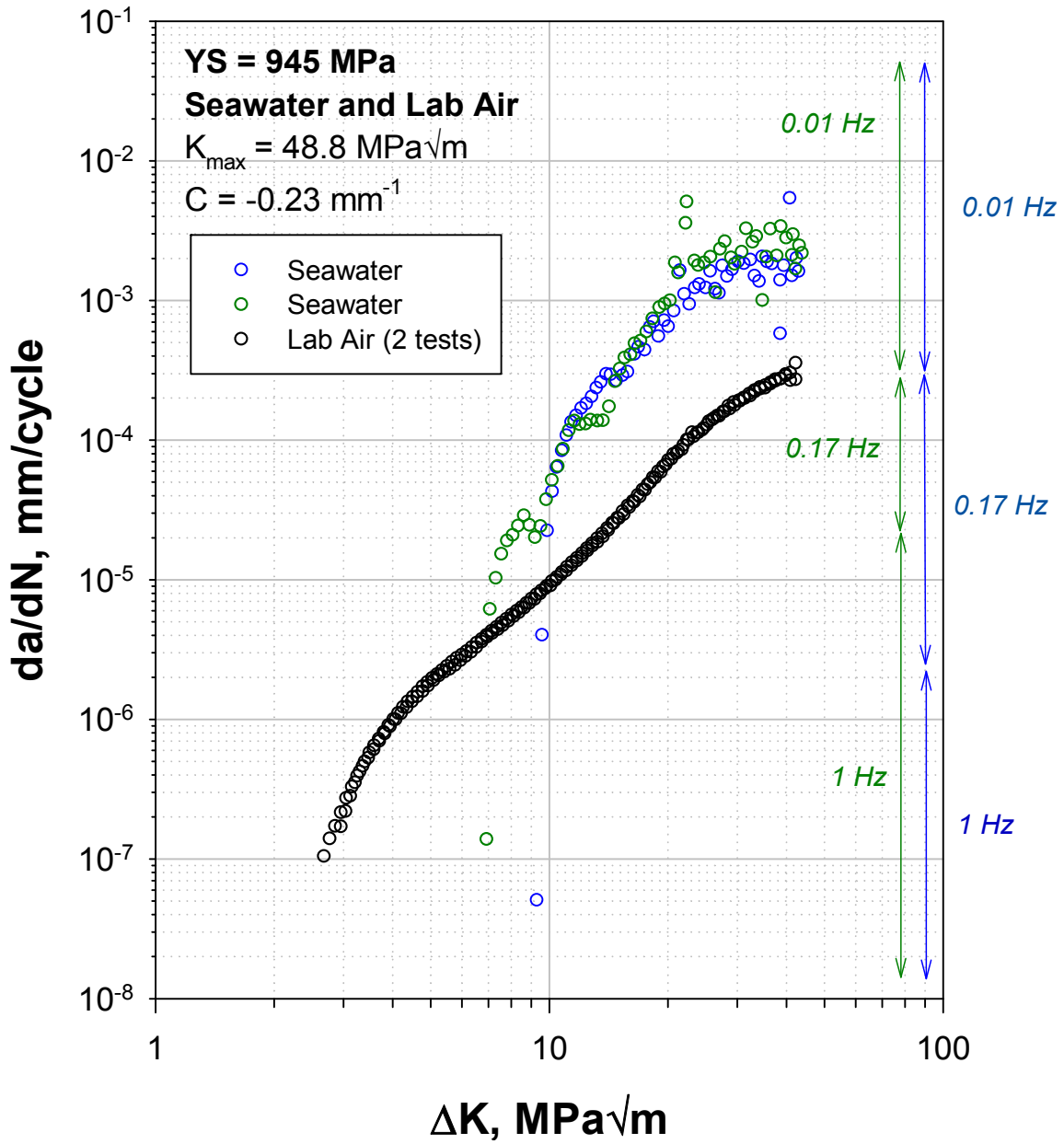


FIGURE 5-15: The effect of frequency schedule on the seawater corrosion-fatigue crack growth rates in the 945 MPa YS steel.

The corrosion-fatigue crack growth rate results shown in Figures 5-12 and 5-15 exhibit similar trends with respect to frequency schedule. Namely, continuing to test at 0.17 Hz to a lower growth rate resulted in the precipitous drop-off in rates below a ΔK of 10 MPa \sqrt{m} (the blue data points). In contrast, switching from 0.17 Hz to 1 Hz at a higher rate resulted in much higher growth rates in this regime and a distinct suppression of the apparent ΔK_{th} value at which the rates precipitously drop-off. Although the shift in apparent ΔK_{th} is only about a 22-24 percent, it results in rates in this regime that differ by several orders of magnitude.

The above effect of frequency schedule was not observed for the 1080 MPa YS material in seawater, as shown in Figure 5-16. In this case the initial rates at high ΔK are three to four times faster than those shown in Figures 5-12 through 5-15. The fact that these high rates in Figure 5-16 persist to a very low ΔK value suggests that they may be associated with stress corrosion cracking (SCC) resulting from the high K_{max} value of 48.8 MPa \sqrt{m} in this test, as well as the high yield strength of this particular steel. These high rates are also consistent with the frequency-scan results on this material (Figure 5-6) that were obtained at $\Delta K = 22$ MPa \sqrt{m} and $R = 0.5$, and which also correspond to a relatively high $K_{max} = 44$ MPa \sqrt{m} . Because of the relatively constant, high rates in this test, the frequency was never decreased below 0.01 Hz as in prior two tests. Overall, the seawater data in Figures 5-12 through 5-16 exhibited the same sensitivity to material YS as did the frequency-scan results.

Figures 5-17 and 5-18 summarize the corrosion-fatigue crack growth rates in the sour brine environment for the 848 MPa and 945 MPa strength level materials. These experiments used the same frequency schedules as those described above for tests in the seawater environment. However, in the sour brine environment the different frequency schedules result in more significant differences in the rates than in the case of the seawater environment. The increased sensitivity to frequency schedule in this case is likely a reflection of the more aggressive nature of the sour brine environment compared to the seawater environment.

The final point to be made regarding the effect of frequency on the corrosion-fatigue crack growth rates in steel is that in both the seawater and sour brine environments the data at low ΔK exhibit an inverse frequency dependence – that is, *increasing* rates with *increasing* frequency at a given value of ΔK . This inverse frequency dependence is opposite to the classical frequency dependence that is observed at higher ΔK values, as evidenced by the previously described results from both the frequency-scan tests at $\Delta K = 22$ MPa \sqrt{m} in Section 5.1.2. As discussed in the following section, the observed inverse frequency dependence at low ΔK is theorized to be due to the effect of corrosion product wedging on the effective ΔK local to the crack-tip.

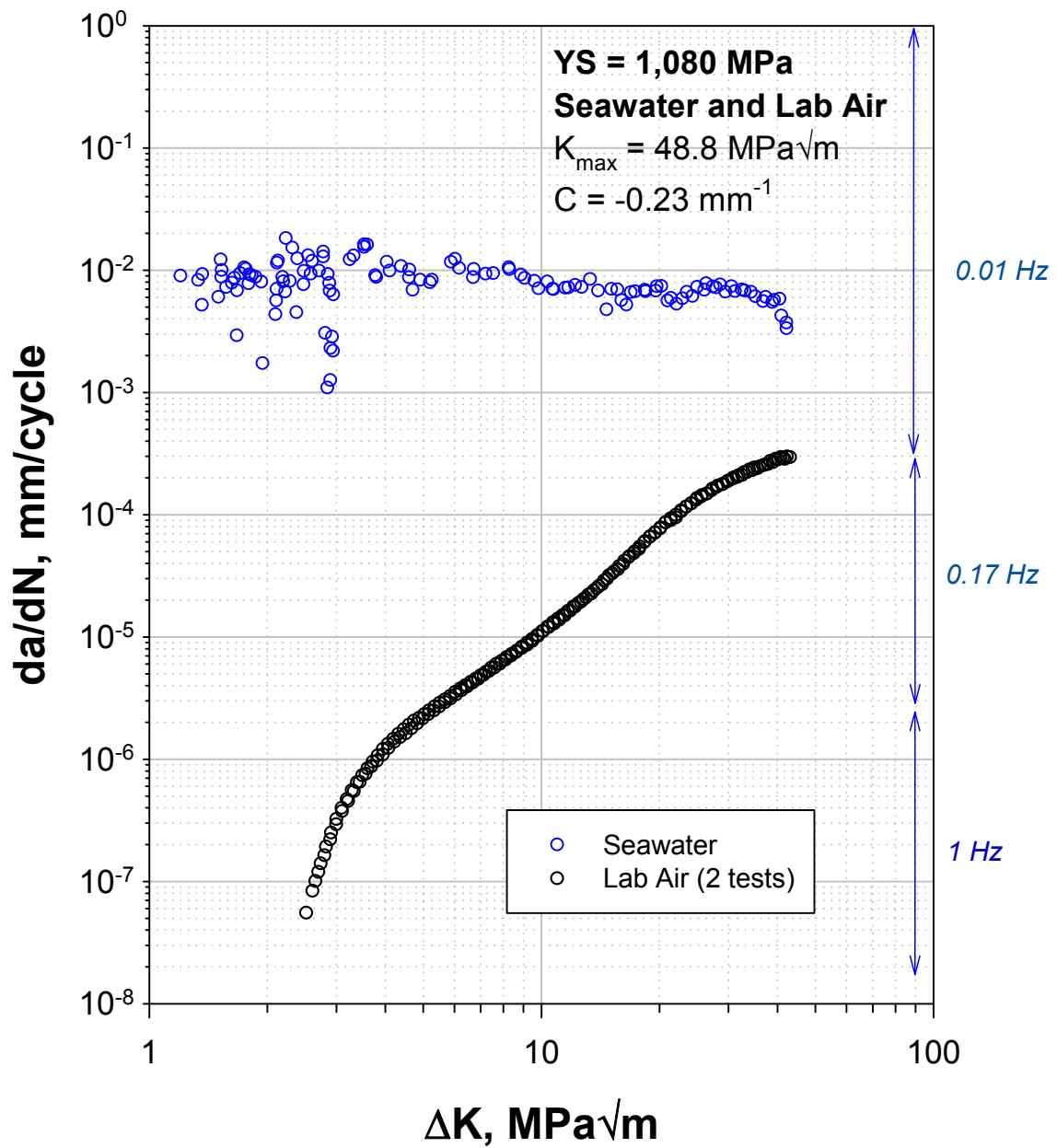


FIGURE 5-16: The relative ΔK -independence of seawater corrosion-fatigue crack growth rate in the 1080 MPa YS steel.

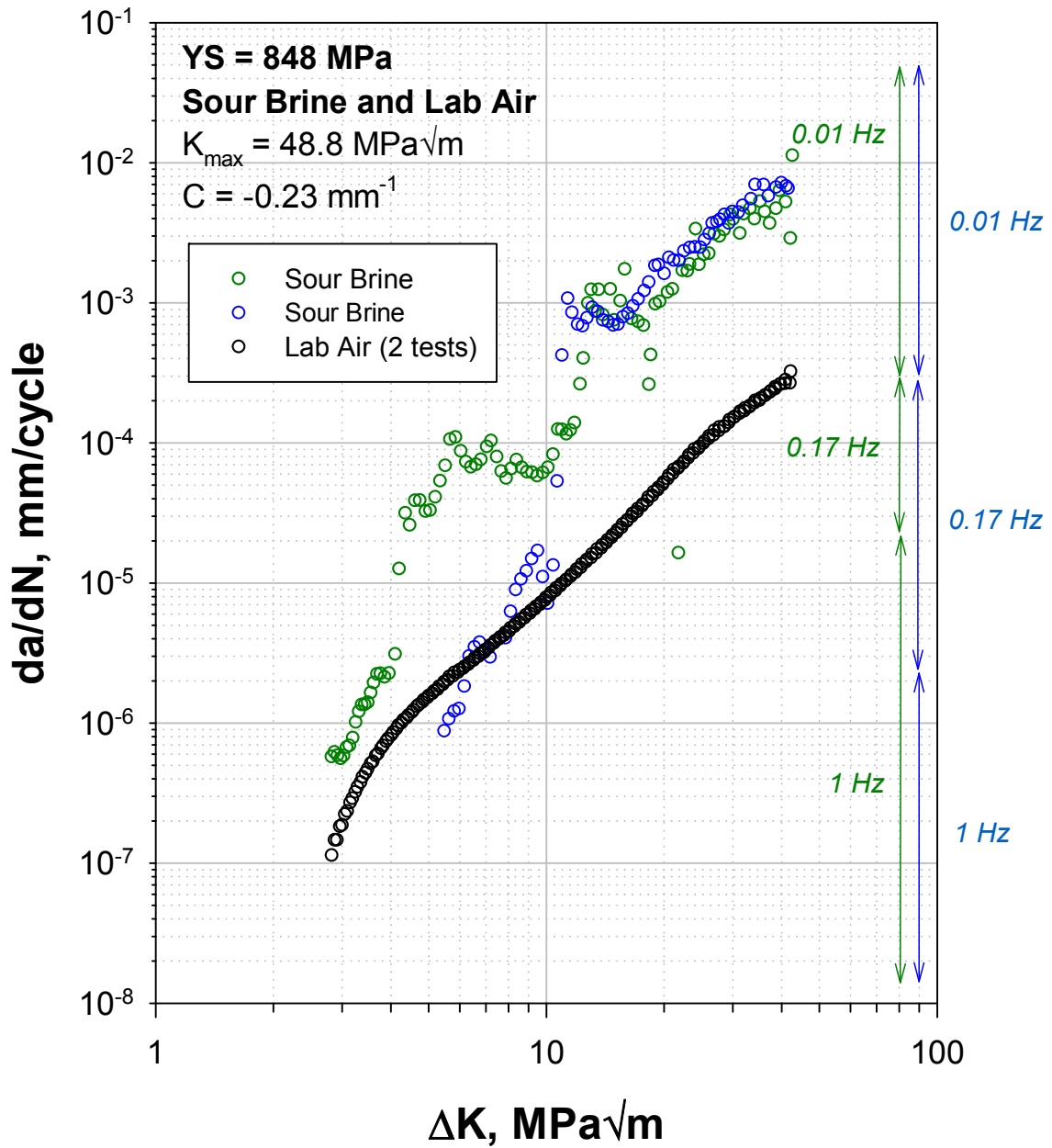


FIGURE 5-17: The effect of frequency schedule on the sour brine corrosion-fatigue crack growth rates in the 848 MPa YS steel.

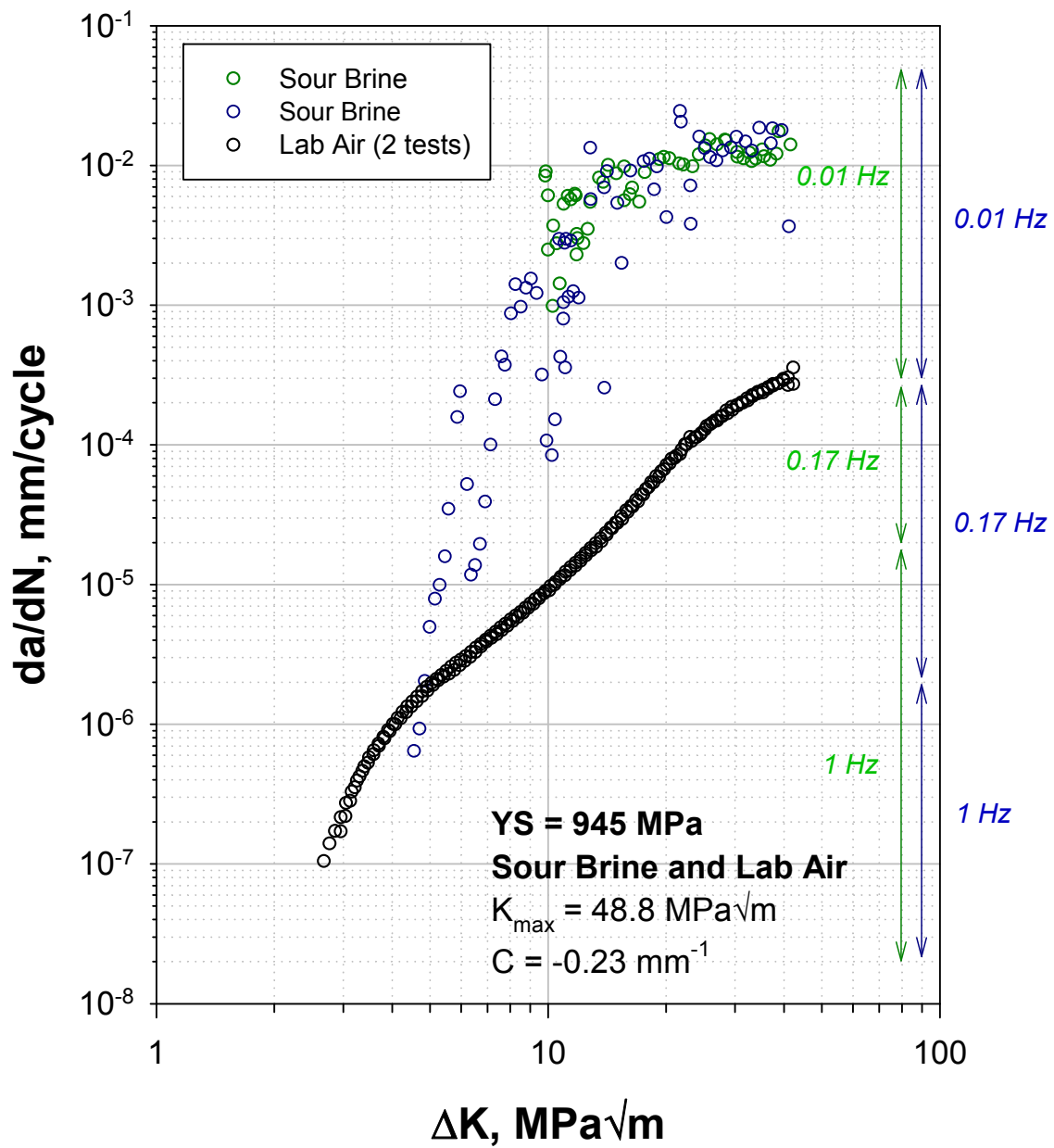


FIGURE 5-18: The effect of frequency schedule on the seawater corrosion-fatigue crack growth rates in the 945 MPa YS steel.

5.1.5 Possible Mechanisms Causing Inverse Frequency Effects in Steels at Low ΔK

The precipitous drop-off in growth rates at low frequencies, and associated inverse frequency dependence, in aggressive environments has also been previously observed, as shown in Figure 5-19. This phenomenon is believed to be caused by crack closure resulting from the build-up of corrosion product debris within the crack [8-9]. The wedging action of the corrosion products can cause the effective ΔK (ΔK_{eff}) at the crack-tip to be less than the applied ΔK that is normally computed from remote load and crack size. Support for this mechanism is provided by actual crack closure measurements obtained using elastic compliance measurements. These results are shown in Figure 5-20 and were obtained while generating the corrosion-fatigue crack growth data summarized in Figure 5-19 [8-9].

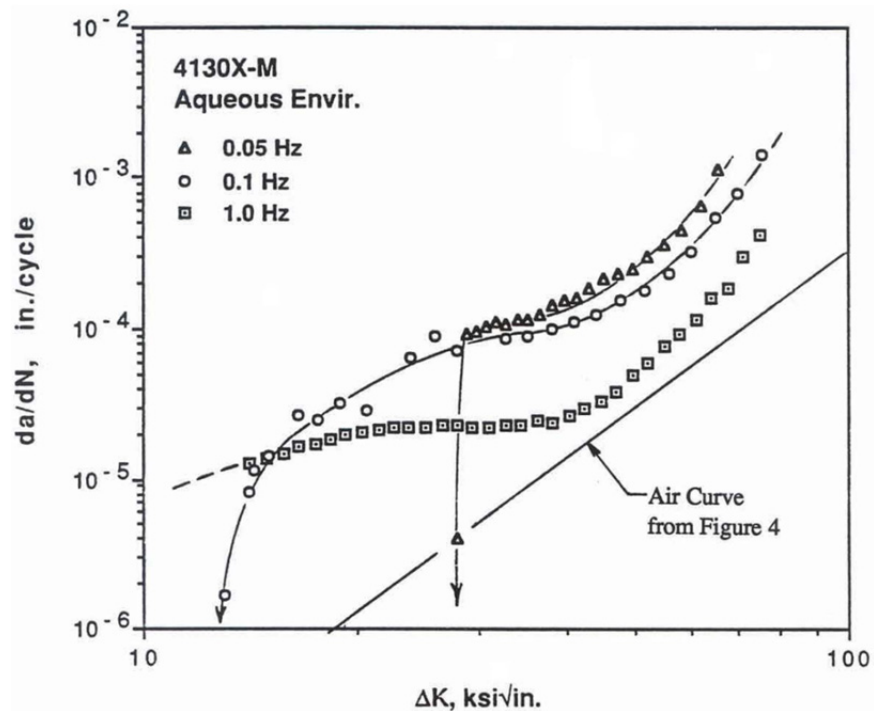


FIGURE 5-19: Influence of frequency on crack growth in an aqueous $H_2S + CO_2$ environment [8, 9].

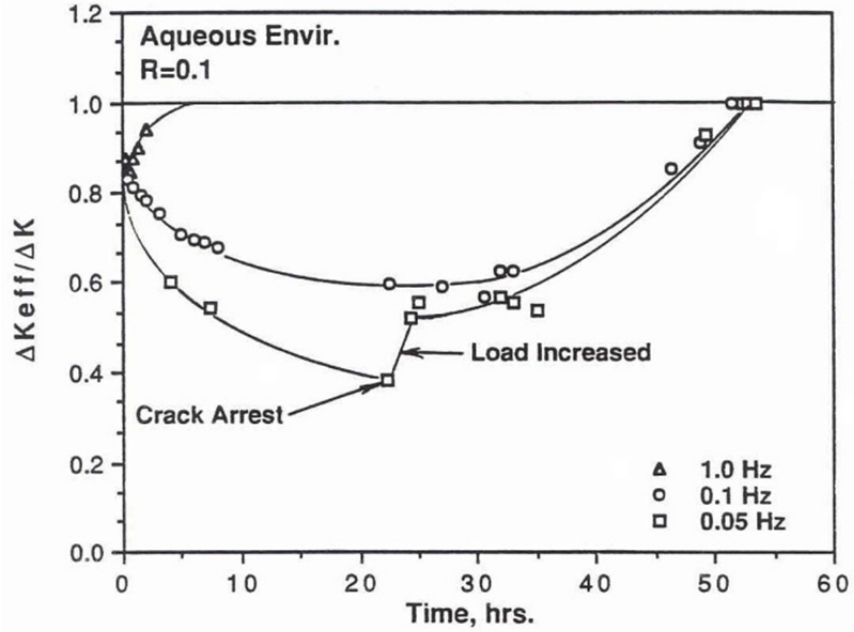


FIGURE 5-20: Variation in crack closure and effective crack driving force over time for experiments conducted in aqueous H₂S + CO₂ environment at various cyclic frequencies [8, 9].

It should be pointed out that the crack growth and crack closure results in Figures 5-19 and 5-20, respectively, were generated at R of 0.1. At this low R-value, the K_{max} value and elastic crack opening displacement would also be expected to be low since

$$\delta = 4 / \pi \left(\frac{K_{\max}^2}{E \sigma_{ys}} \right) = 4 / \pi \left(\frac{\Delta K^2}{(1-R)^2 E \sigma_{ys}} \right) \quad (2)$$

Where δ is the maximum crack opening displacement at K_{max}, the maximum K in the loading cycle, $\Delta K = K_{\max} - K_{\min}$, $R = K_{\min}/K_{\max}$, E is the elastic modulus, and σ_{ys} is the materials' yield stress. It follows that the process of corrosion debris build-up and associated crack wedging is expected to be rather sensitive to R, or equivalently to K_{max}. Thus, changing the loading variables will significantly alter the extent of crack closure from corrosion product wedging, as well as the resulting crack growth response. We believe this to be the case over a wide range of loading conditions, since crack closure is an inextricable part of the crack growth process and persists even at high R and high K_{max} levels, although it becomes more localized as indicated by high resolution crack closure measurements [24].

It is significant to note that the above phenomenon has also been observed in corrosion-fatigue crack growth in a titanium alloy in saltwater [25] and an aluminum alloy in sump-tank water [26]. Thus, this phenomenon may well be universal to environment enhanced fatigue crack growth.

Based on the above mechanistic understanding, it is reasonable to postulate that the frequency for onset of saturation, or alternatively the frequency giving the maximum fatigue

crack growth rate, will increase with decreasing applied ΔK – as notionally illustrated in Figure 5-21. If this precise response were experimentally determined, this knowledge could be used to rationally define an optimum S-N or fatigue crack growth testing protocol whereby frequency could be systematically increased as applied stress is decreased, thereby minimizing the test duration required to generate long life data beyond 10^6 cycles. However, significant frequency-scan testing would be required to adequately map the detailed response in Figure 5-21.

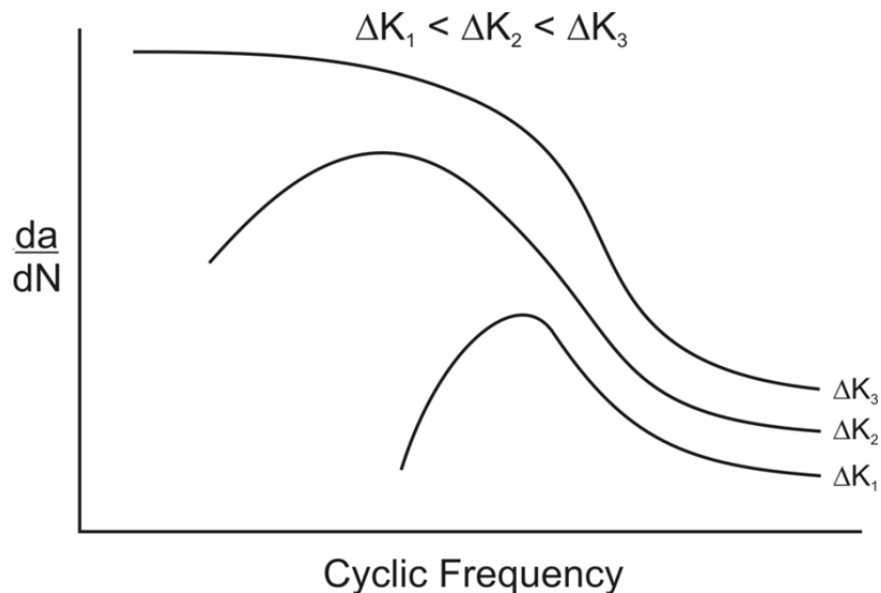


FIGURE 5-21: Notional representation of complex dependence of fatigue crack growth rates on cyclic frequency hypothesized based on current understanding of crack closure associated with corrosion-product induced wedging.

The inverse frequency dependence observed here at low ΔK , which is believed to be caused by corrosion product debris build-up, is in marked contrast to the classical frequency dependence often observed at higher ΔK values that is believed to be caused by one or more rate-controlling kinetic processes involved in supplying damaging hydrogen to the crack-tip [27]. In this regard, possible rate-controlling processes can include the transport of reactive species to the crack-tip, the chemical/electrochemical reactions at the fresh surface created by the high strain at the crack-tip, and/or the diffusion of hydrogen to the region of hydrostatic stress ahead of the crack-tip. We believe that understanding these rate controlling processes holds the key to comprehending and eventually predicting the dependence of corrosion-fatigue crack growth rates on material, environmental (temperature, partial pressure, pH), and loading variables (ΔK , R, and particularly cyclic frequency).

5.1.6 Effect of Steel Strength Level on Corrosion-Fatigue Crack Growth Rates vs. ΔK

It is significant to note that although the corrosion-fatigue crack growth rate trends with respect to frequency schedule in Figures 5-12 through 5-15 are similar in all steels and environments, the actual rates at a given ΔK can differ significantly, depend on the material strength level and/or microstructure. This effect is more clearly seen in Figures 5-22 and 5-23, where results are compared for the five steels tested in seawater and sour brine for each of the two different frequency schedules, respectively. Above ΔK values of 20 MPa \sqrt{m} the rates in both figures are similar since all data were generated at 0.01 Hz; however, below ΔK value of 20 MPa \sqrt{m} the rates begin to diverge in the two figures due to the influence of different frequency schedules, as discussed in Section 5.1.4. Nevertheless, in both figures, the crack growth rates at a given ΔK differ significantly depending on the steel. Specifically, the steels with YS values of 848 MPa, 924 MPa and 945 MPa exhibit comparable rates within the factor of two-to-three observed data scatter. However, the rates in the steel with a YS of 1080 MPa are several orders magnitude higher; moreover, these persist to very low ΔK values approaching one, with no indication of a ΔK_{th} . This behavior suggests that these high rates are associated with the onset of a stress corrosion cracking (SCC) mechanism at the applied K_{max} value of 48.8 MPa \sqrt{m} . The overall trend for the above steel is increasing susceptibility to corrosion-fatigue or SCC with increasing yield strength. However, the exception to this trend is 910 MPa YS steel rates, which are significantly greater than those of steels with YSs in the range of 848 MPa to 945 MPa, thereby suggesting that steel processing and microstructure can also have a significant effect on corrosion-fatigue susceptibility.

Figures 24 and 25 summarize the corrosion-fatigue crack growth rates vs. ΔK measured in the sour brine environment for the 848 MPa and 945 MPa YS steels, for the two different frequency schedules. In both cases, the higher strength 945 MPa steel exhibits significantly higher rates than those exhibited in the 848 MPa steel. It is also interesting to note that this difference in rates between these same two materials is more pronounced in the sour brine environment (Figures 24 and 25) than in the seawater environment (Figures 22 and 23). These results are consistent with the often observed trend that sour brine environments are more damaging to steels than are seawater with typical levels of cathodic protection. This is presumable due to the known ability of H_2S to poison the hydrogen recombination reaction thereby producing more atomic hydrogen at the surface that can diffuse into, and damage, the steel.

Thus, it appears that overall susceptibility of steels to corrosion-fatigue in offshore environments is complex and depends on strength level, and/or processing and microstructure, as well as details of the environment.

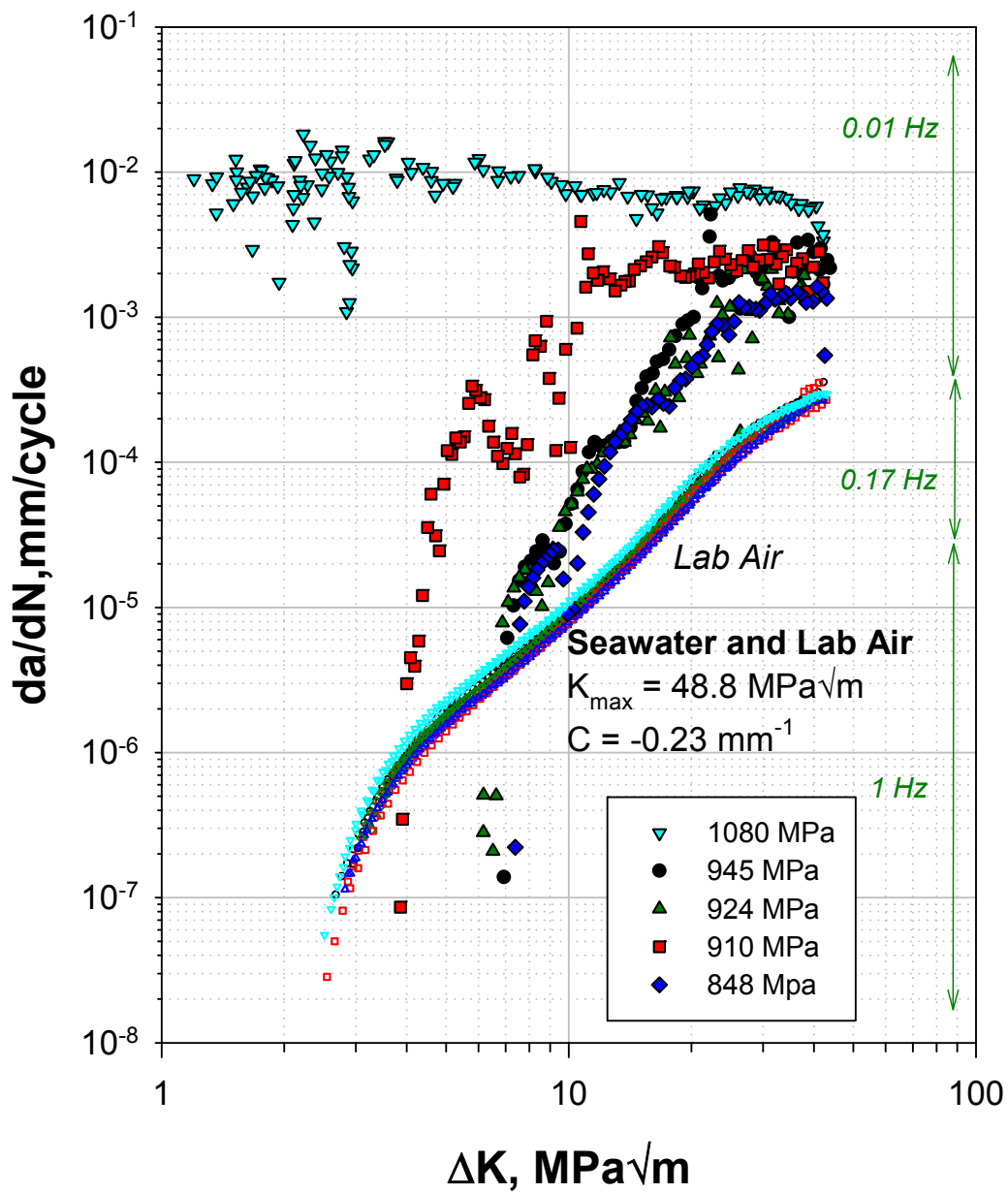


FIGURE 5-22: Corrosion-fatigue crack growth rates in seawater and air as a function of steel strength for Frequency Schedule 1.

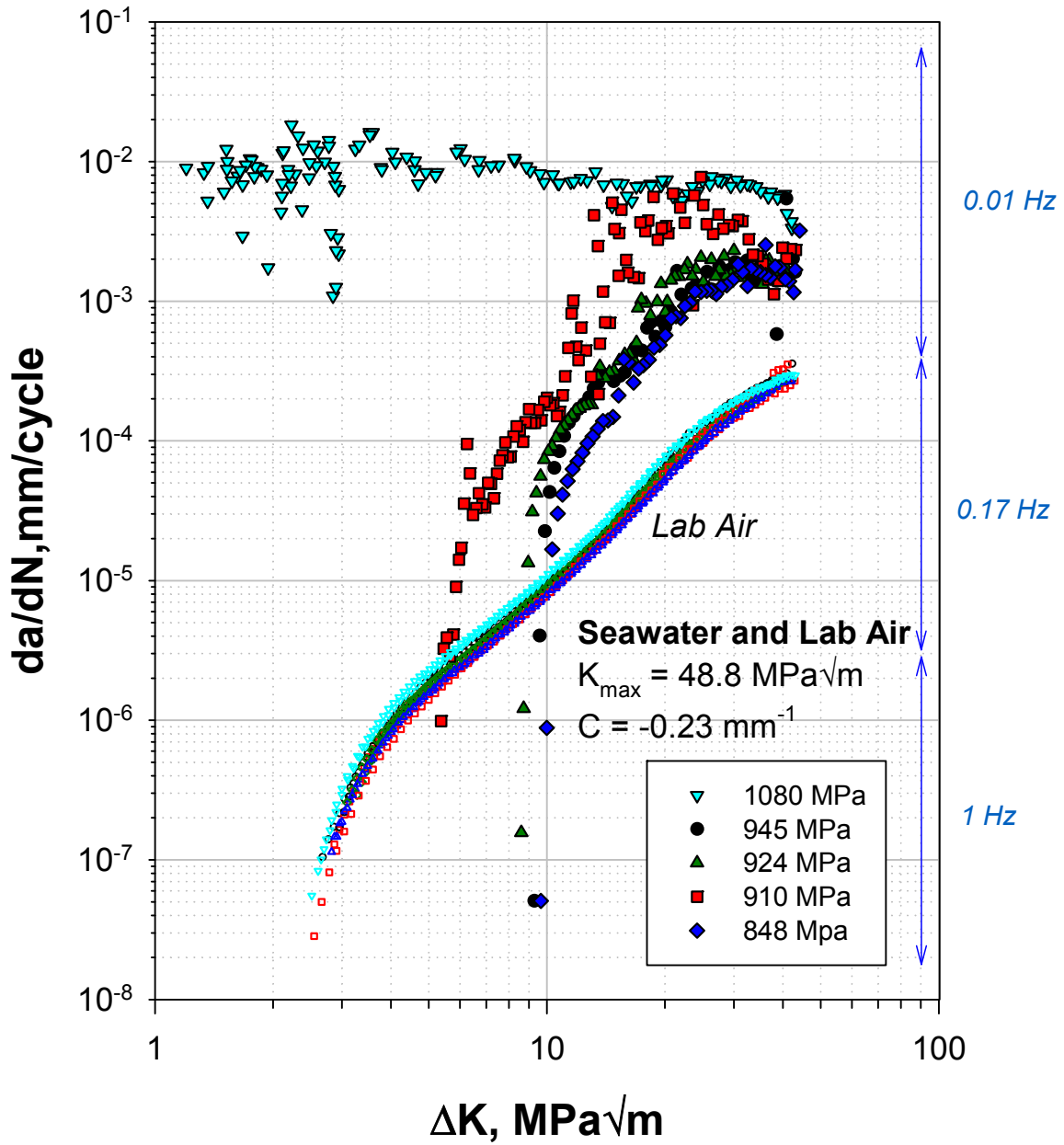


FIGURE 5-23: Corrosion-fatigue crack growth rates in seawater and air as a function of steel strength level for Frequency Schedule 2.

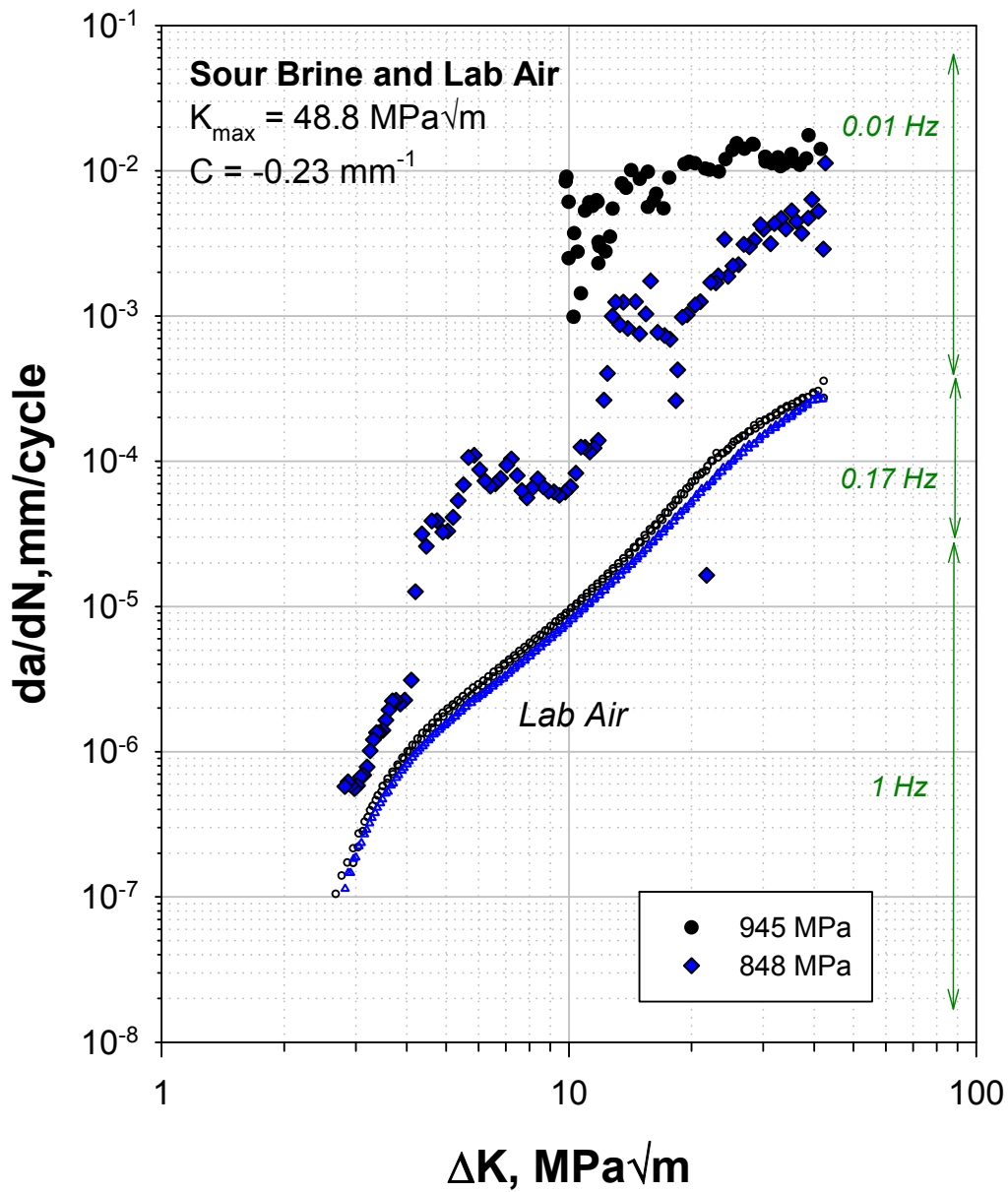


FIGURE 5-24: Corrosion-fatigue crack growth rates in sour brine and air as a function of steel strength level for Frequency Schedule 1.

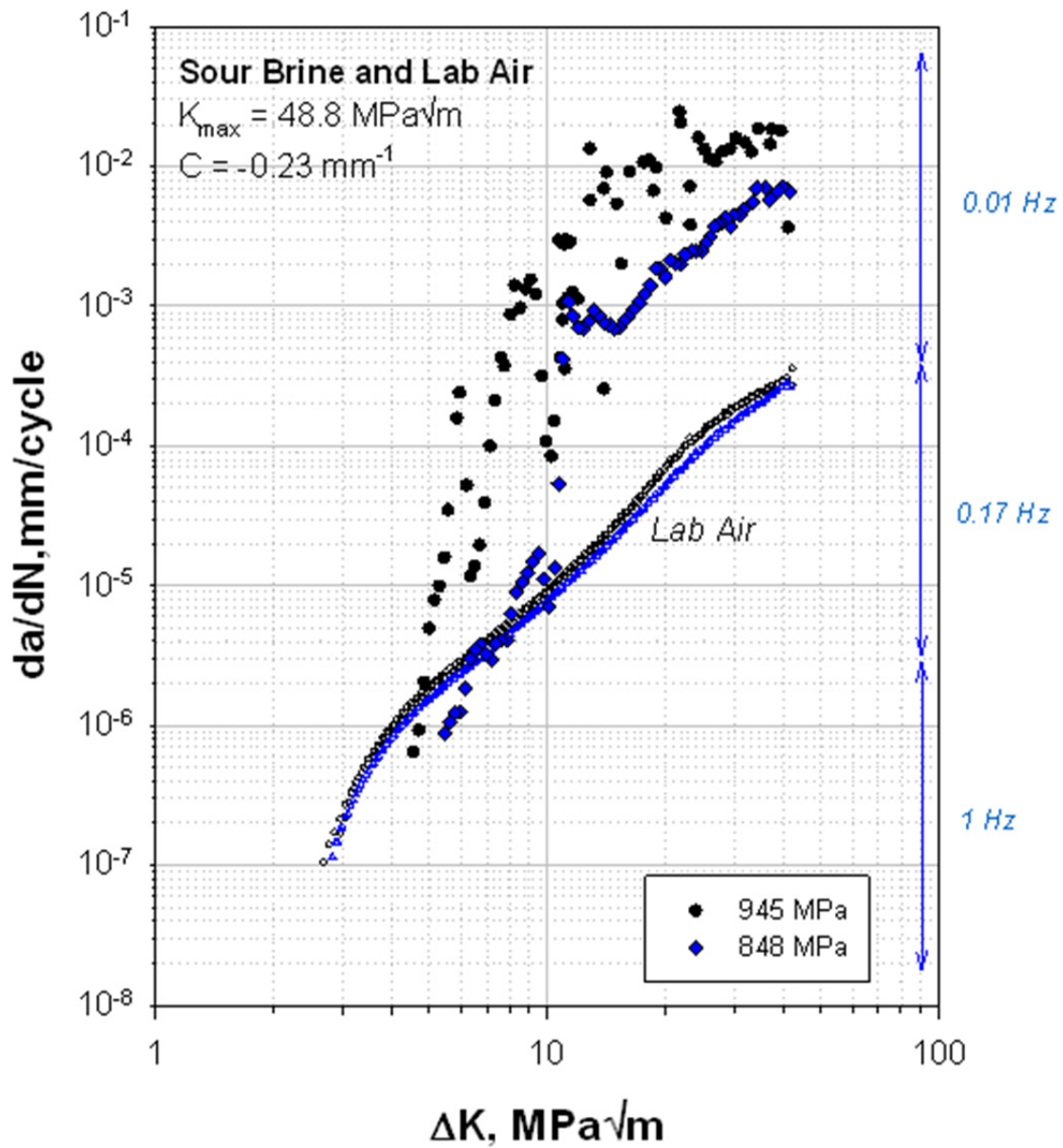


FIGURE 5-25: Corrosion-fatigue crack growth rates in sour brine and air as a function of steel strength level for Frequency Schedule 2.

5.2 Ti-29 Corrosion-Fatigue Crack Growth Rates

This section summarizes the corrosion-fatigue crack growth rate performance of Ti-29 in sour brine versus air, and compares these results to those for steels of comparable strength levels in the same environments. Fractographic analyses of the fracture surfaces from crack growth in sour brine and air were also performed in attempting to understand the corrosion-fatigue response in the Ti-29 alloy.

5.2.1 Ti-29 Fatigue Crack Growth Rates in Lab Air

The fatigue crack growth rates in Ti-29 having a YS of 786 MPa that were measured in laboratory air are summarized in Figure 5-26, along with comparable results on two of the steels having similar YS levels (848 MPa and 945 MPa). At ΔK below 10 MPa \sqrt{m} , the fatigue crack growth rate response in the Ti-29 is comparable, or perhaps a bit lower, than those in the steels. However, as the ΔK values increase above 10 MPa \sqrt{m} , the fatigue crack growth rates in Ti-29 become increasingly faster than those in the steels and eventually level off at about three to four times faster than those in the steels. These differences in relative fatigue crack growth behavior between the two materials in different ΔK and crack growth rate regimes suggest the operation of two competing mechanisms in the two regimes.

At high ΔK values, the higher rates exhibited by Ti-29 compared to those in the steels are likely the result of the combined effects of the lower elastic modulus and lower tensile ductility in Ti-29 compared to those in the steels. At low ΔK values, the convergence of the fatigue crack growth rates are likely due to the occurrence of increasing crack closure behavior in the Ti-29 alloy. Specifically, the planar slip deformation character of Ti-alloys often gives rise to enhanced crack closure at low ΔK values due to a roughness-induced closure mechanism, which in the current instance appears to override the modulus and ductility effect that appears to be operative at high ΔK . Nevertheless, regardless of the details of the underlying mechanisms, the similarity in fatigue crack growth rate behavior in these two alloy systems in the low ΔK and low fatigue crack growth rate regime is the significant observation since this is the regime of most practical interest under high cycle fatigue, which is the dominant fatigue loading experienced by risers in service.

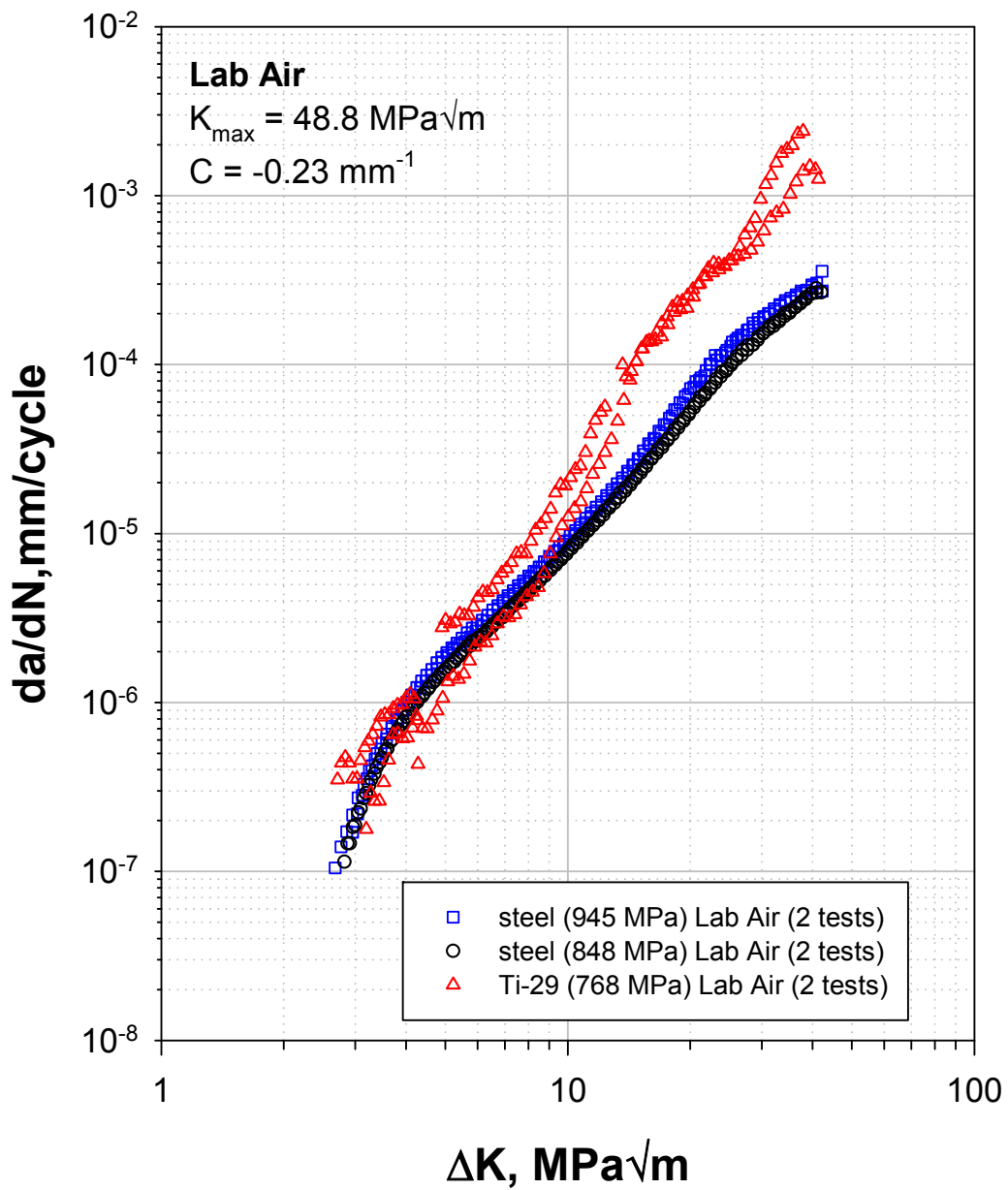


FIGURE 5-26: Comparison of air fatigue crack growth rate data in the 786 MPa YS Ti-29 with those in the 848 MPa and 945 MPa YS steels.

5.2.2 Effect of Loading Frequency on Ti-29 Corrosion-Fatigue Crack Growth Rate

Fatigue crack growth rates measured during the frequency scan tests on the Ti-29 alloy in sour brine environment exhibited a significantly different frequency sensitivity and overall degree of degradation than those in the high-strength steels. As can be seen in the frequency scan data in Figure 5-27, initially the sour brine environment increased the corrosion-fatigue crack growth rates by about a factor of two to three compared to the average rates in air, which are represented by the black data points and dashed line. Moreover, the maximum rates in the sour brine environment occurred during the 10 Hz and 1 Hz cycling early in the test, while subsequent cycling at significantly lower frequencies of 0.33 Hz, 0.1 Hz, and 0.01 Hz resulted in rates that were two to three times slower than the average rates in air. In fact, after the peak rate was observed the trend was for subsequent rates to decrease systematically as the crack grew from a normalized crack length (a/W) from 0.4 to 0.7, where 'a' is crack length and W is specimen width. Consequently, after the initial increase in crack growth rates, subsequent rates were more a function of crack length (or crack growth) than of cyclic loading frequency. Crack growth rates measured at the slowest cyclic frequency of 0.01 Hz were not discernible from those measured in lab air. It is also interesting to note that these fatigue crack growth rates for Ti-29 in sour brine exhibited significantly higher scatter compared to those in steel measured under similar conditions (see Section 5.1.2), thereby further confounding the assessment of the extent to which the sour brine environment degrades the fatigue crack growth behavior in Ti-29.

To ensure that the above apparent crack length dependence was not due to extraneous factors – for example, residual forming stresses in producing the seamless pipe, or an inherent strain rate sensitivity in the deformation response of Ti-29 – an additional frequency scan was performed in lab air. The results from this frequency scan in air are shown in Figure 5-28, where they are compared with the prior frequency scan results in sour brine. As can be seen, the resulting fatigue crack growth rates (represented by the gray squares) were relatively constant, thereby demonstrating an independence from both crack length and frequency. Thus, it appears that neither forging residual stresses, nor inherent material strain rate sensitivity is responsible for the unusual frequency response of Ti-29 subjected to cyclic loading in the sour brine environment.

As shown in Figure 5-29, cracks grown in the sour brine environment exhibited a very rough fracture surface topography, compared to cracks grown in the air environment. In order to quantify this difference, the topographic measurements of the crack surfaces grown in lab air and sour brine environments were assessed. These measurements included both surface roughness and surface waviness. Surface roughness is defined as closely spaced (short wavelength) irregularities, while surface waviness is defined as more widely spaced (longer wavelength) irregularities. These features are identified in Figure 5-30, which summarizes the sour brine results; three traces of the crack surface profile are shown corresponding to 25% (Trace 1), 50% (Trace 2), and 75% (Trace 3) of the specimen thickness. Each of these traces was measured in the direction of the growing crack. For each trace, the following results are given: 1) the surface profile, which contains both roughness and waviness components; 2) the waviness component, which was obtained by fitting a smooth curve through the surface profile; and 3) the roughness component, which was obtained by filtering-out the long-wavelength

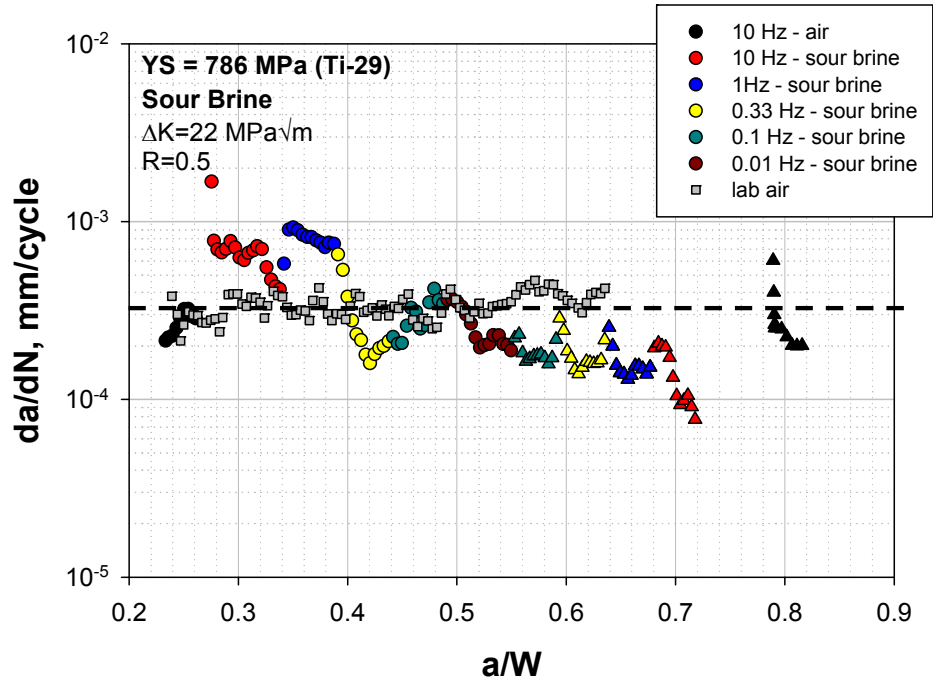


FIGURE 5-27: Frequency scan results in 786 MPa Ti-29 alloy in sour brine environment.

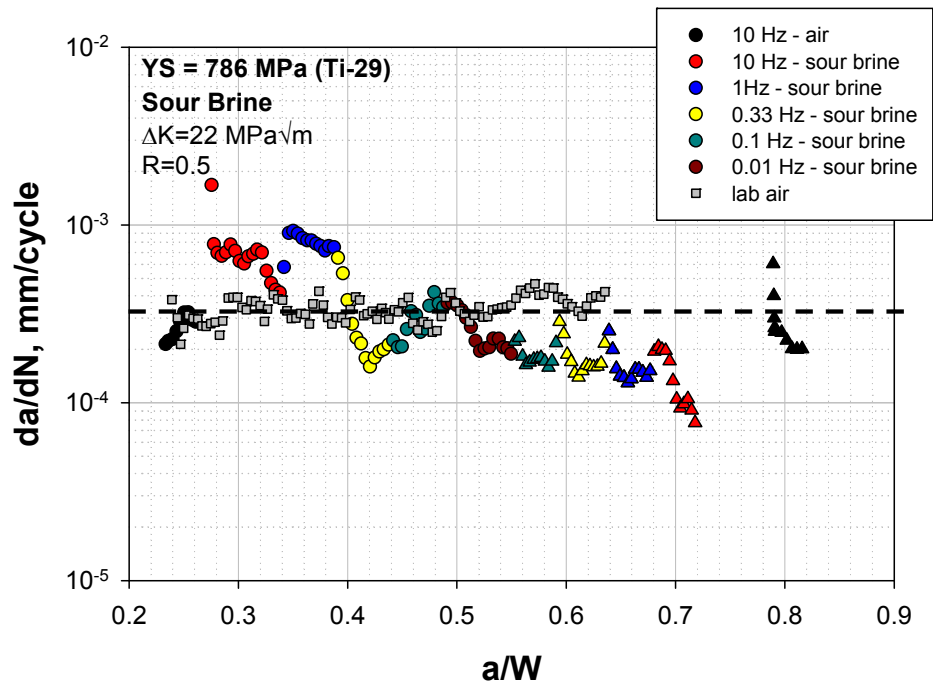


FIGURE 5-28: Comparison of frequency scan results in 786 MPa Ti-29 alloy in lab air versus sour brine environment.

waviness component. Figure 31 shows comparable results for the crack grown in lab air. In general, both roughness and waviness of the crack surface can contribute to crack closure as the peaks of the profile come into contact while the stress applied to the crack is decreased during fatigue loading. This contact occurs because most real cracks do not separate in pure Mode I (opening mode), but also have a small component of Mode II (in-plane sliding mode). Table 5-2 summarizes the quantitative measurements in terms of the arithmetic mean roughness (R_a), as well as surface waviness in terms of the arithmetic mean waviness (W_a).

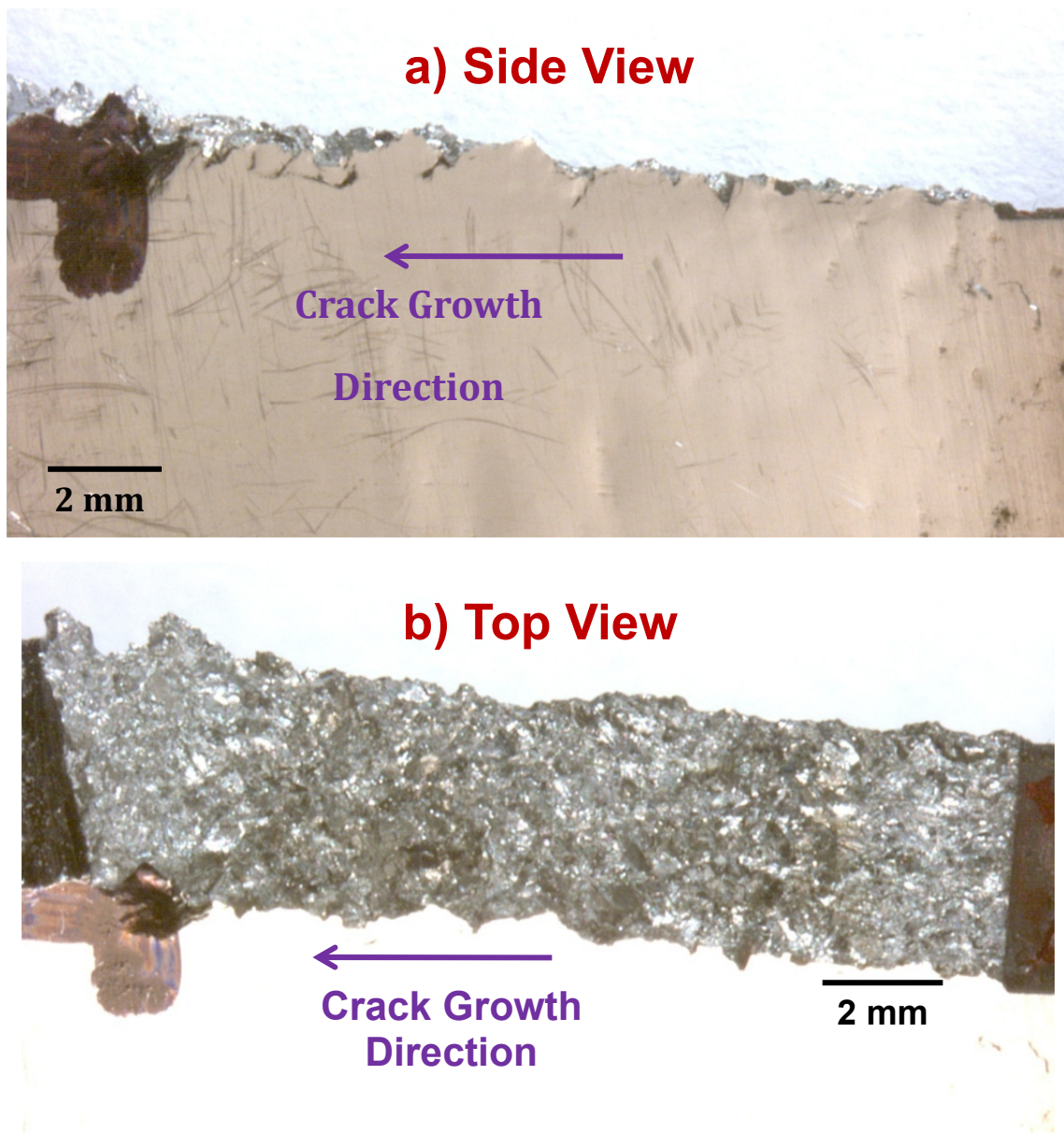


FIGURE 5-29: Rough fracture surface topography of specimen tested in sour brine environment: a) side view showing out-of-plane cracking, and b) top view showing rough fracture surface topography.

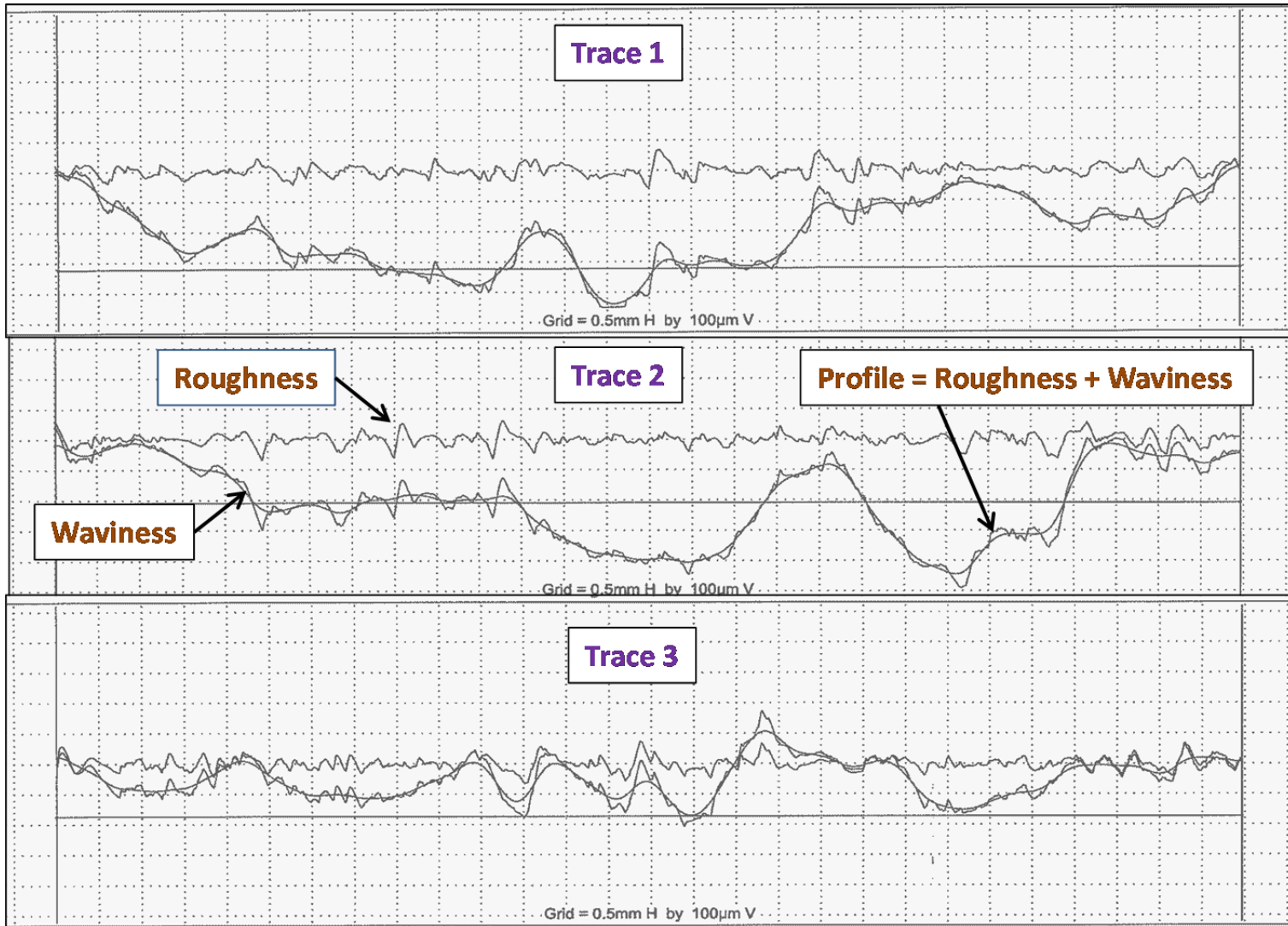


FIGURE 5-30: Topographic measurements on crack surfaces tested in sour brine environment.

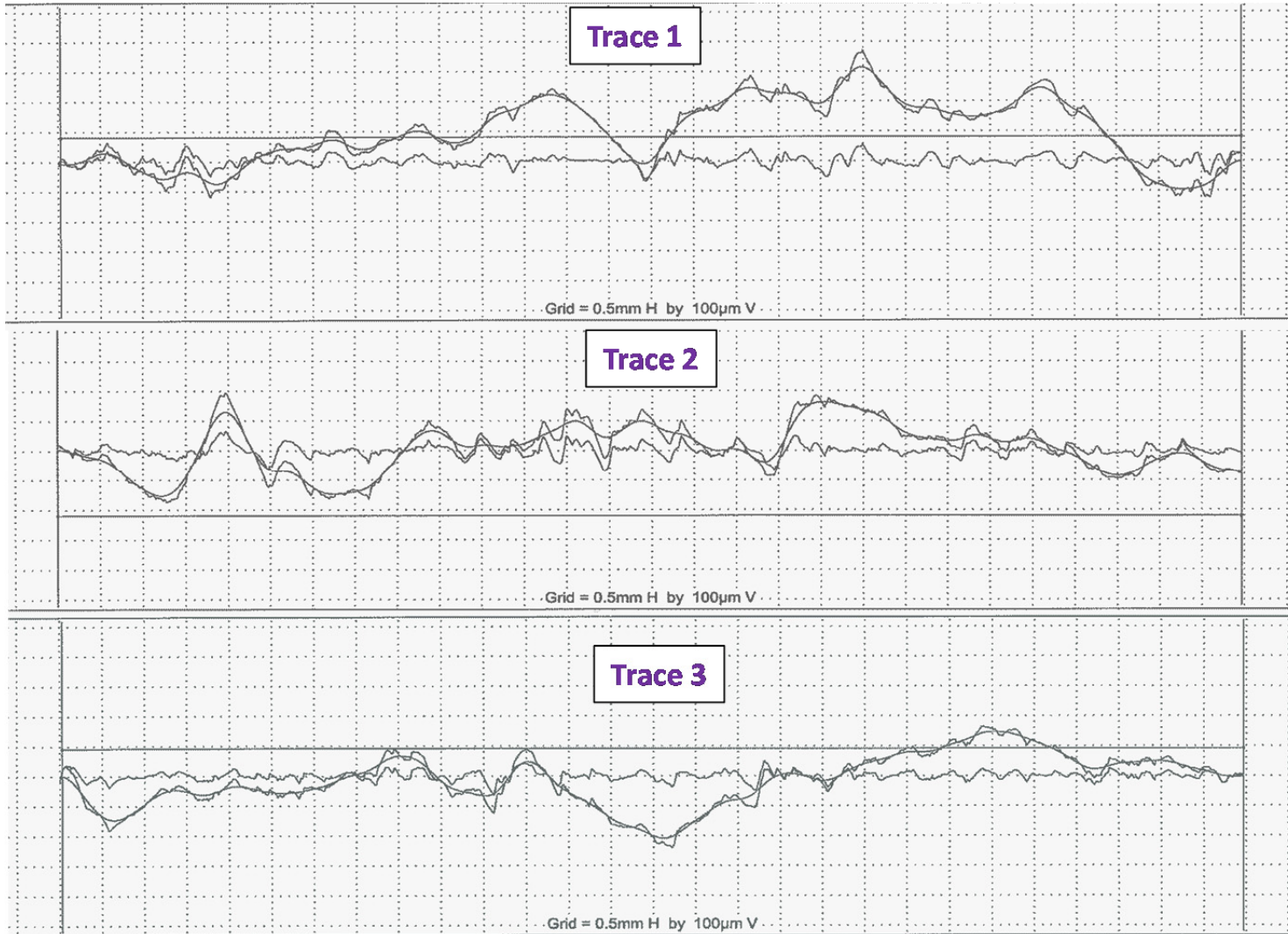


FIGURE 5-31: Topographic measurements on crack surfaces tested in air environment.

Table 5-2: Surface topography for Ti-29 corrosion-fatigue cracks grown in air versus sour brine environments.

Topographic Parameter	Air Environment				Sour Brine Environment			
	Trace 1	Trace 2	Trace 3	Air Ave.	Trace 1	Trace 2	Trace 3	Sour Ave.
Roughness, R_a (μm)	13.2	15.3	11.0	13.2	14.1	14.4	15.1	14.5
Waviness, W_a (μm)	118.8	63.0	66.3	82.7	210.3	207.7	61.9	160.0

By comparing the measurements in Table 5-2, as well as the surface profiles in Figures 5-30 and 5-31, it can be seen that the mean roughness is very similar for cracks grown in air and sour brine environments. However, the waviness for the crack grown in sour brine is about twice the magnitude of that for the crack grown in air. These results are consistent with the differences in corrosion-fatigue crack growth rates in the two environments, as previously shown in Figure 5-28. Specifically, the nature of the undulations in the measured crack growth rates in Figure 5-28 for a/W values greater than 0.4 is strikingly similar to the measured waviness in the surface topography. Nevertheless, it is not possible to correlate these two observations one-to-one since none of the three traces fully characterizes the average through-thickness waviness of the crack surfaces; this is evident from the significant variability in the three surface profiles for a given environment. This variability in the surface profiles suggests that at any moment in time (or in a given loading cycle) the crack-tip advances along a tortuous path. This path is governed by the planar-slip deformation character of Ti-29 (and Ti-alloys in general), which on a micro-scale give rise to the local surface roughness as the crack proceeds from one grain (or grain ensemble) to another. Eventually this microscopic change in crack direction results in a more global out-of-plane cracking, which is manifested in the observed waviness measurements. This out-of-plane cracking then contributes to additional Mode II sliding which causes further contact of the complex two-dimensional crack profiles.

5.2.3 Ti-29 Corrosion-Fatigue Crack Growth Rates Versus ΔK

Figure 5-32 summarizes the fatigue crack growth rate data in Ti-29 in the sour brine environment; the baseline data in lab air are also shown for comparison. At ΔK values above 20 $\text{MPa}\sqrt{\text{m}}$, one of the tests in sour brine exhibited crack growth rates that were faster than the air data by a factor of three to four. However, the second test in the sour brine environment exhibited rates that are comparable to the air rates at high ΔK , but drop below the air rates at lower ΔK values. It is unclear whether this difference in rates between the two sour tests is due to the previously discussed inverse frequency effect in steel, or to the high variability in fatigue crack growth rates in the Ti-29 alloy, as was observed in the frequency scan results in Figure 5-27.

Figure 5-33 compares the Ti-29 data in air and sour brine from Figure 5-32 with the sour brine data in the steel of comparable strength level (786 in Ti-29 versus 848 MPa in steel) from Figure 5-17. It is interesting to note that at high ΔK values the fastest rates in Ti-29 approach those observed in the steel. However, at low ΔK values, the rates in Ti-29 merge with the rates in the steel at 0.17 Hz, which are significantly less than the rates in steel at 1 Hz due to the inverse frequency effect in steel that was discussed above. This merging of the crack growth rates in Ti-29 and steel at low ΔK values is likely due to the tortuous crack path and significant crack closure that can develop in Ti-29, which eventually overcomes the modulus effect that dominates at higher ΔK values.

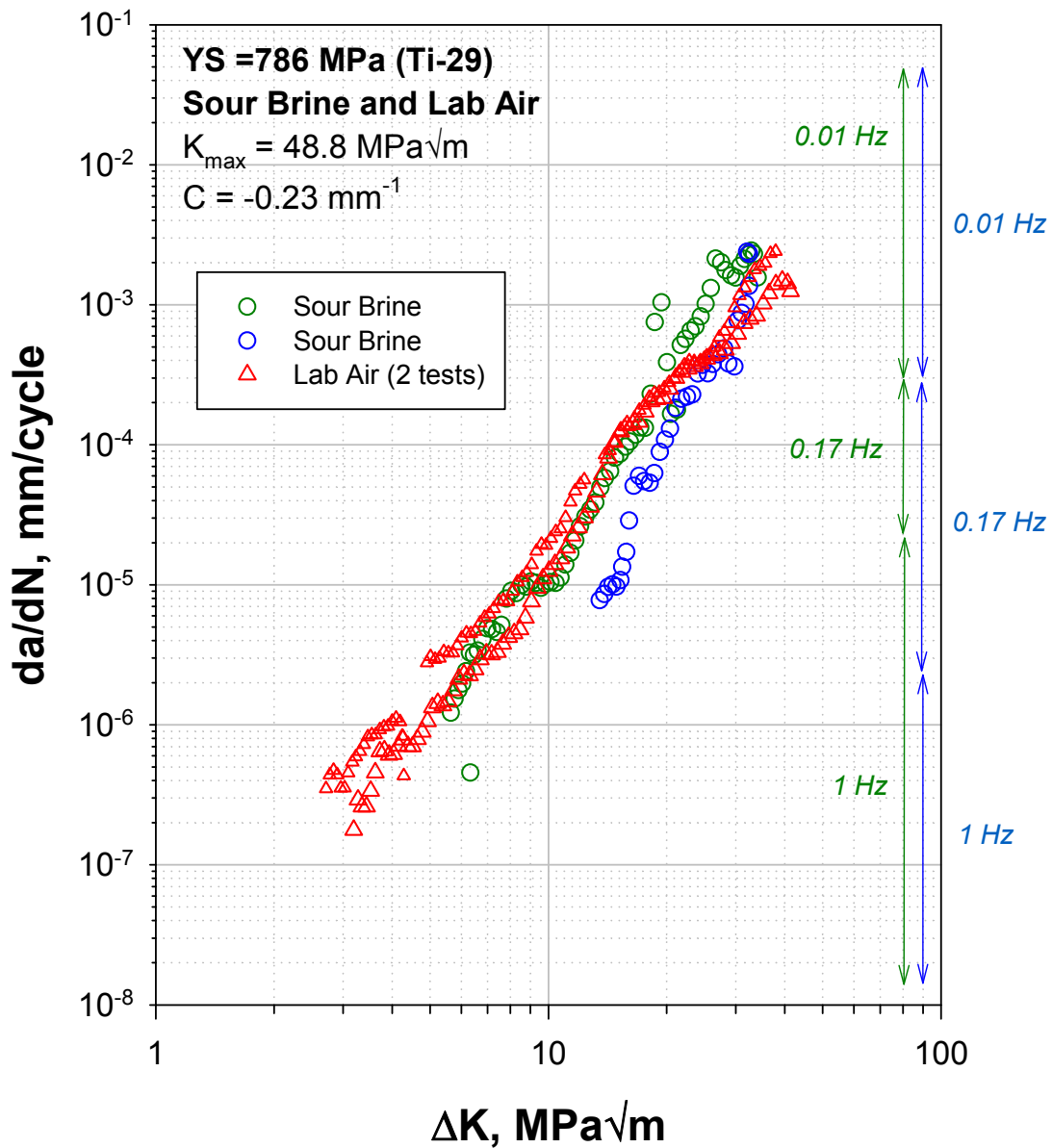


FIGURE 5-32: Corrosion fatigue crack growth rate data for Ti-29 in the sour brine environment; the Ti-29 lab air data from Figure 5-20 are also shown for comparison.

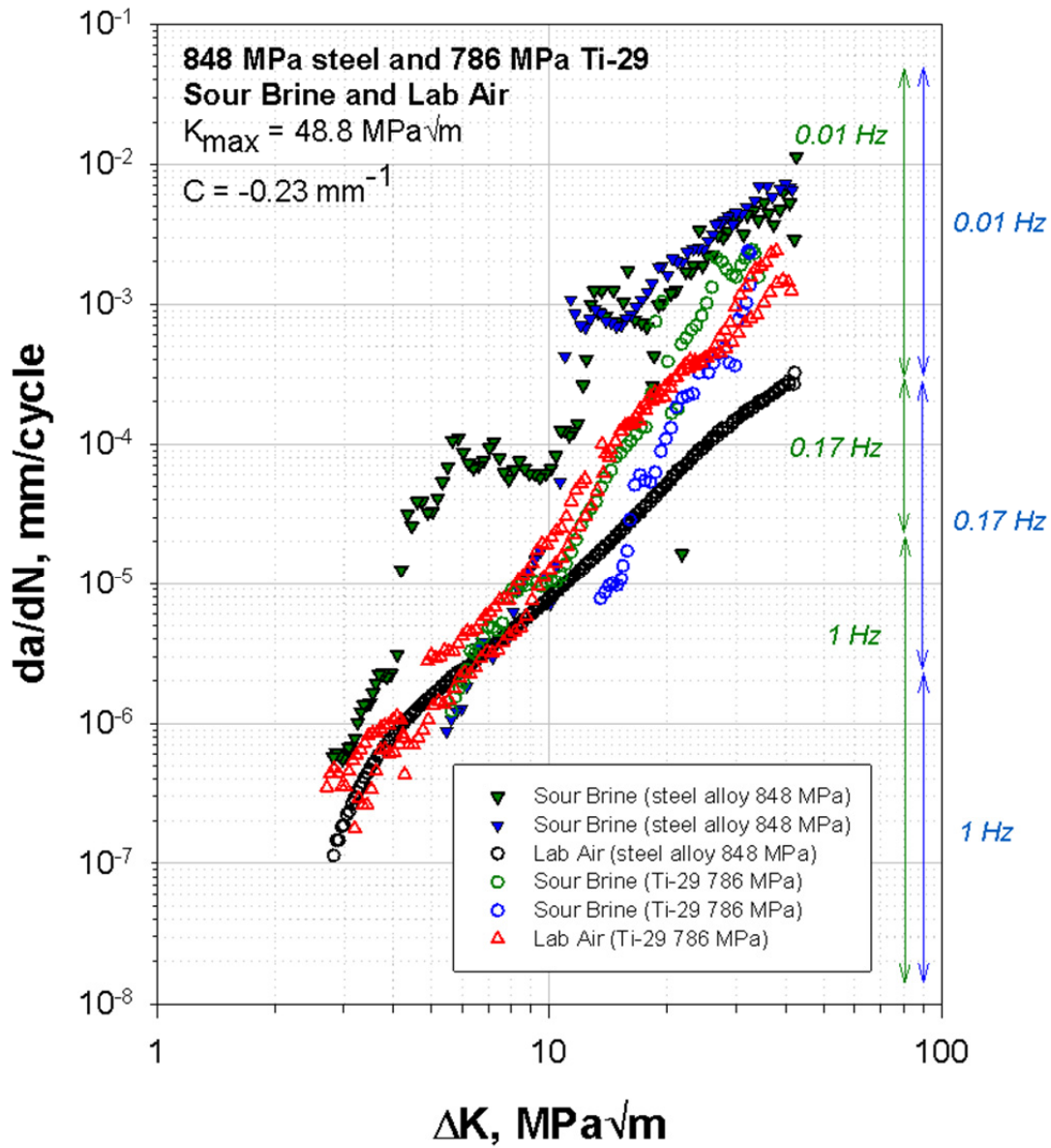


FIGURE 5-33: Comparison of Ti-29 fatigue crack growth rate data in lab air and sour brine (from Figure 5-32) versus those in the 848 MPa YS steel in lab air and sour brine (from Figure 5-17).

6.0 S-N FATIGUE RESULTS AND DISCUSSION

This section summarizes the corrosion-fatigue performance in terms of the classical S-N fatigue life approach for all six test materials in the baseline laboratory air (Air) environment, as well as in the seawater plus cathodic protection (SW+CP) environment, and sour brine (SB) environment. For each of these environments results are first summarized for the five high-strength steels, followed by results for the Ti-29 alloy, which also includes a comparison with the steel results.

6.1 High-Strength Steel S-N Corrosion-Fatigue Results and Discussion

6.1.1 Steel S-N Fatigue Lives in Lab Air

Most of the baseline air data obtained in the current project were generated at the DOE's National Energy Technology Laboratory (NETL). Selected air data were also generated at Southwest Research Institute on the 848 MPa YS steel in order to compare with the NETL-generated data on the same steel, and thereby assess the inter-laboratory reproducibility of results. These results are shown in Figure 6-1 and can be seen to exhibit good agreement between the two laboratories, particularly considering the typical scatter often observed in S-N fatigue data.

Figure 6-2 compares the air S-N fatigue data for the five steels, each having different strength levels. As indicated by the data, there was no measurable difference among the S-N fatigue lives for the steels with yield strengths ranging from 848 MPa to 945 MPa YS; however the 1080 MPa YS data exhibited noticeably longer fatigue lives. Moreover, close examination of the data beyond 1 million cycles indicated about a 30 percent higher fatigue endurance limit at 10 million cycles for both the 945 MPa and 1080 MPa YS steels compared to the lower strength steels. This trend of increasing fatigue endurance limit with increasing strength is well known for materials tested in benign environments, which is largely the case for these steels tested in laboratory air. This increase in fatigue endurance limit may also be due to differences in steel microstructure; although this assessment was not performed since the pipe manufacturers requested that their materials' microstructures be kept proprietary as a condition for donating the materials to the project. The fact that the current results on the three lowest strength steels (848 MPa to 924 MPa) do not exhibit different fatigue endurance limits is likely due to their small difference (9 percent) in nominal strength level.

Figure 6-2 also shows the trend line for the air data obtained by linear regression analysis using the applied stress as the independent variable and the fatigue life as the dependent variable. This analysis was limited to data with fatigue lives less than one million cycles where the S-N results are linear in log-log space and thus can be properly represented by a power law equation. The regression parameters for this power law fit are as follows:

$$N_f = 2 \times 10^{17} (\Delta\sigma)^{-4.486} \quad (3)$$

Equation 3 will be used as the basis for comparing the relative extent of environmental degradation in these steels due to both the seawater and sour brine environments.

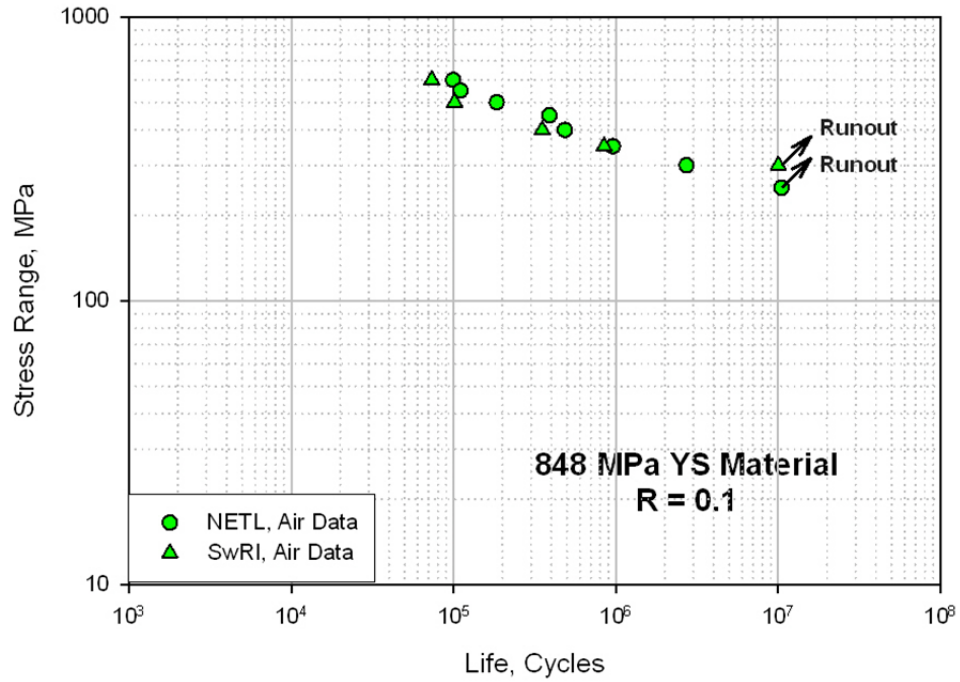


FIGURE 6-1: Comparison of air-baseline S-N fatigue data generated at SwRI and at NETL.

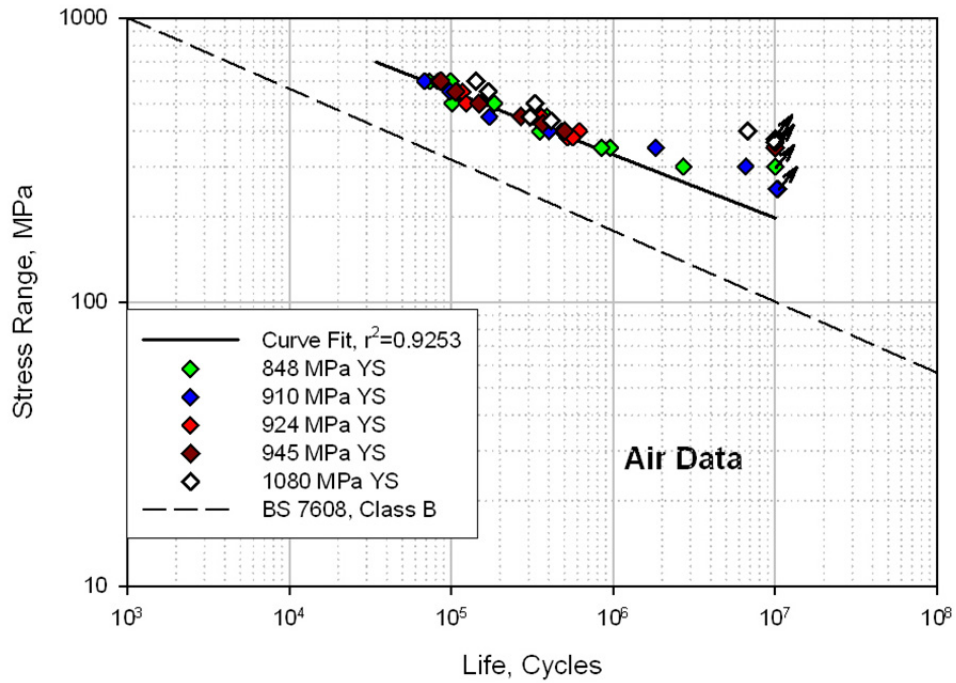


FIGURE 6-2: Comparison of air baseline S-N fatigue data for five steels at various strength levels with the BS 7608, Class B design curve.

Figure 6-2 also compares the air fatigue data from the current study with the fatigue design curve for C-Mn steel base material given in BS 7608, Class B. As can be seen, the high strength steels from the current project are well above the Class B design curve. Specifically, for stresses below 300 MPa the current fatigue lives are at least an order of magnitude greater than those of the BS 7608, Class B design curve.

6.1.2 Steel S-N Corrosion-Fatigue Lives in Seawater with Cathodic Protection

A summary of the S-N fatigue data in Air versus SW+CP is provided in Figure 6-3. Note the difference in slopes of the results in the two different environments, which results in the SW+CP data converging with the air data at high stress and low fatigue lives. This slope difference is a manifestation of the fact that the degradation in fatigue life due to the interaction of the material and seawater environment varies with applied stress range – specifically, from less than a factor of two at high stress ranges to about a factor of ten at lower stress ranges and longer lives.

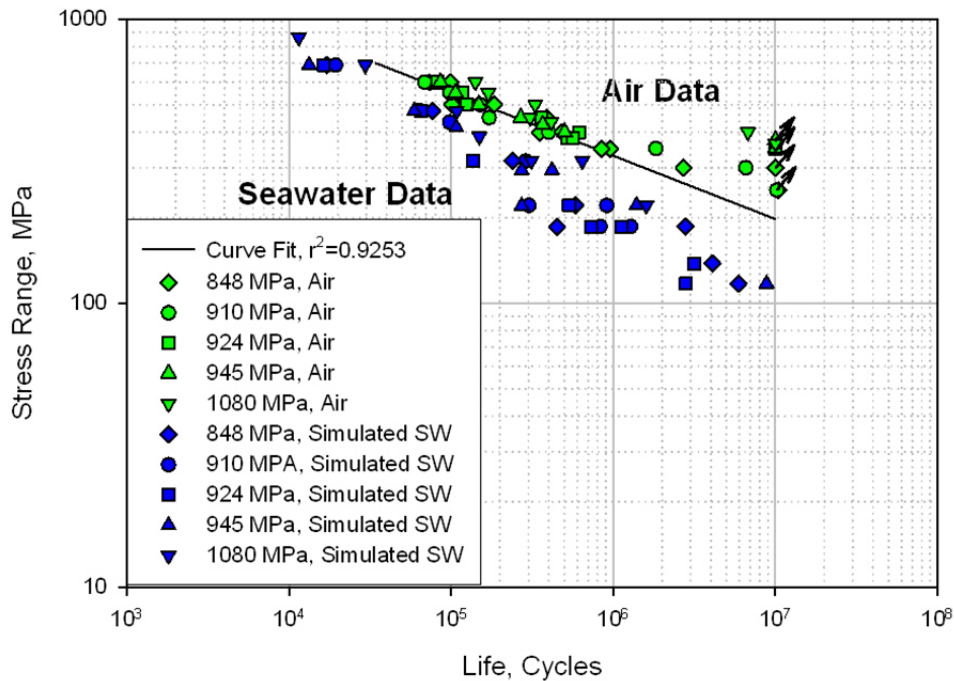


FIGURE 6-3: Comparison of S-N fatigue data in baseline air and seawater with cathodic protection environments.

6.1.3 Steel S-N Corrosion-Fatigue Lives in Sour Brine

A summary of the S-N fatigue data in air versus SB environments is provided in Figure 6-4. The slope of the SB curve differs from that of the Air curve, but the slope difference is much less pronounced than that exhibited by the SW+CP versus Air data shown in Figure 6-3. Consequently, the SB and Air curves do not converge even if the curves are extrapolated back to very low fatigue lives (e.g., 100 cycles). At applied stress ranges of 500 MPa, 400 MPa, and 200 MPa, the corrosion-fatigue lives in sour brine are respectively 30, 50, and 100 times less than those in laboratory air. The comparison below 300 MPa stress ranges is based on extrapolation of Equation 3.

Figure 6-5 provides a summary of the S-N fatigue data in SB, SW+CP, and Air environments. The difference in slopes between the SB and SW+CP data causes more significant differences between these two curves at higher stress ranges in the low-cycle-fatigue-regime than at lower stress ranges in the high-cycle-fatigue regime. Also, there are little or no discernible differences in the corrosion-fatigue lives in any of the environments as a function of material strength level. This trend differs with that observed in corrosion-fatigue crack growth kinetics in Section 5.1.3, as will be discussed later.

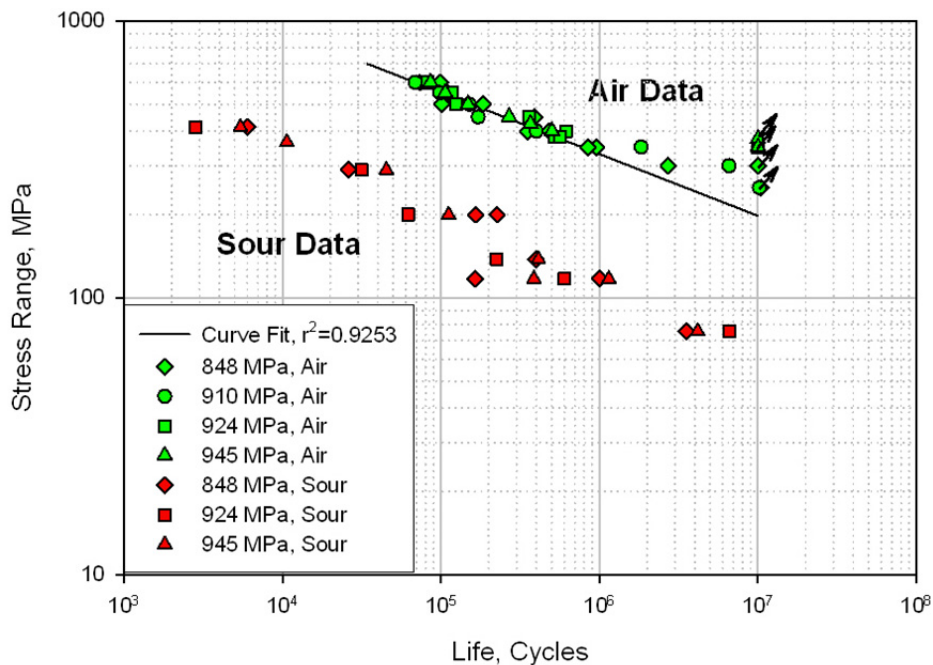


FIGURE 6-4: Comparison of S-N fatigue data in baseline air and sour brine environments.

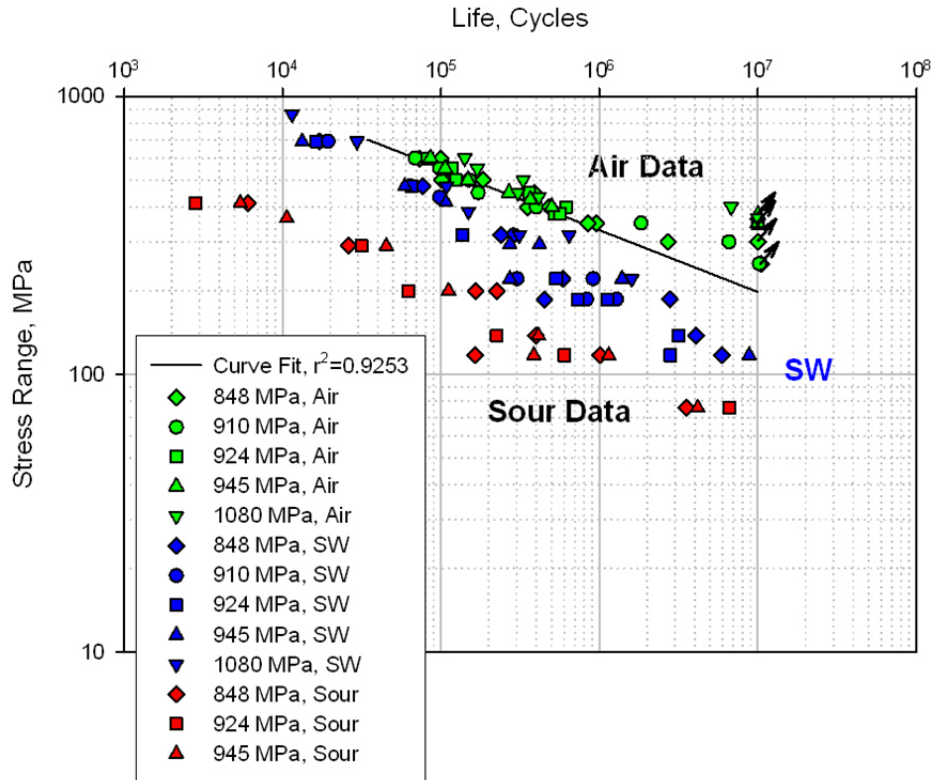


FIGURE 6-5: Comparison of S-N fatigue data in air, seawater with cathodic protection, and in sour brine environments.

6.1.4 Effect of Loading Frequency on S-N Corrosion-Fatigue Life

The possible effect of cyclic loading frequency on the S-N fatigue response in SB and in SW+CP was also examined.

In Figure 6-5, for stress ranges between 186 MPa and 317 MPa, there are seven cases in which more than one life occurs at a given stress range and for a given steel exposed to the SW+CP environment – this is due to the fact that two separate test specimens with different loading frequencies were used at the same stress level. Similarly, for stresses between 117 MPa and 200 MPa there are three cases in which more than one life occurs at a given stress range for a given steel exposed to the sour brine environment. Using these data, the effect of frequency on corrosion-fatigue life can be more clearly seen in the summary graphs of Figures 6-6 and 6-7, where results are presented in terms of a fatigue life ratio (FLR), which is defined here as the fatigue life at 0.17 Hz divided by that at 1 Hz, for a given material, environment, and applied stress range. Thus, FLR less than 1 indicates that the fatigue life decreases with decreasing frequency (the so-called classical frequency effect), and FLR greater than 1 indicates the fatigue life increases with decreasing frequency (the so-called inverse frequency effect). For an FLR of 1, the fatigue life is independent of cyclic frequency.

Based on data obtained in the seawater with cathodic protection environment in Figure 6-6, five of the seven cases indicate a classical frequency effect, while two of the seven cases indicate an inverse frequency effect. In addition, the classical frequency effect is favored at low stress ranges (186 MPa to 221 MPa) while the inverse frequency effect is favored at high stress ranges (294 MPa and 317 MPa). Interestingly, this trend is opposite to that which is reported for corrosion-fatigue crack growth kinetics in the same steels and environments in Section 5.1.3.

Based on data obtained in the sour brine environment in Figure 6-7, the three cases are evenly split with one indicating a classical frequency effect (FLR = 0.28), one an inverse frequency effect (FLR = 6.1), and one indicating little or no influence of frequency (FLR = 1.36) on fatigue life.

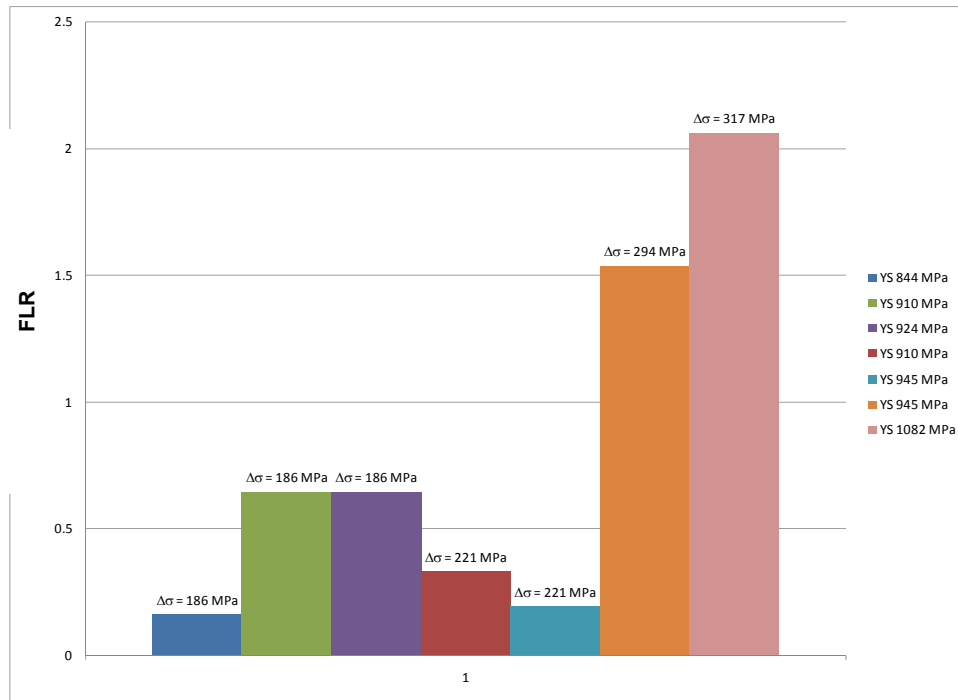


FIGURE 6-6: Corrosion-fatigue life ratios (FLRs) for 0.17-Hz/1-Hz data in the seawater with cathodic protection environment at various applied stress ranges for different steel strength levels.

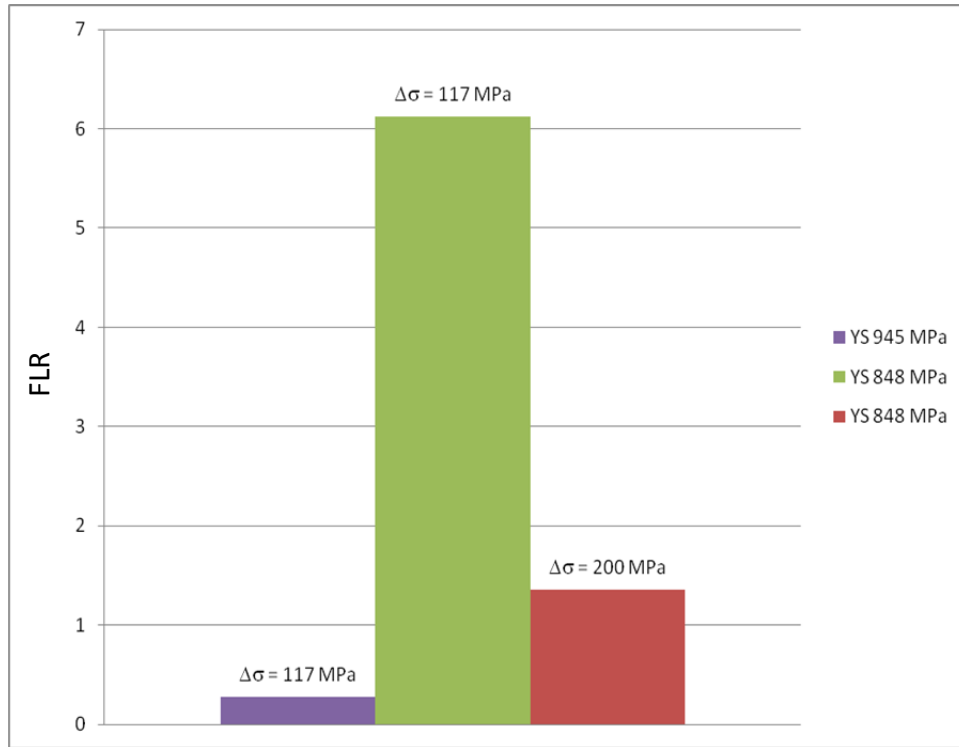


FIGURE 6-7: Corrosion-fatigue life ratios (FLRs) for 0.17 Hz/1 Hz data in the sour brine environment at various applied stress ranges for different steel strength levels.

6.1.5 Comparison of S-N Corrosion-Fatigue in High-Strength Steels Versus X65 Steel

It is of practical interest to compare the current S-N fatigue results on high-strength riser steels with available results on X65 steels tested in both air and sour brine environments [4, 5, and 7]. This comparison for results tested in lab air is shown in Figure 6-8. In interpreting these results it is important to recognize that the current high-strength steel results are in the unwelded condition, while those for the low-strength X65 steels are all in the welded condition. There are no results on welded high-strength steels since a viable weld procedure has not yet been developed for these high-strength steels; thus initial applications of these materials will employ threaded connections.

As can be seen in Figure 6-8, the low-strength steel results vary significantly, and this is primarily due to variations in the welding process employed. The most dramatic effect can be seen in the results labeled SwRI-Tenaris for which the weld root and cap were removed using a flapping process [7], and which resulted in a fatigue endurance limit at 10 million cycles, comparable to the current unwelded results on high-strength steels. These results suggest that much of the detrimental results of welds are due to the geometrical stress concentration of the weld root and cap. The flapping process is also believed to impart a near-surface residual compressive stress in the material, and this may also explain why the endurance limits for these low-strength (448-483 MPa YS) and high-strength (848-924 MPa YS) steels are similar – that is,

they do not follow the strength level dependence of the fatigue endurance limit exhibited by the current results shown in Figure 6-2.

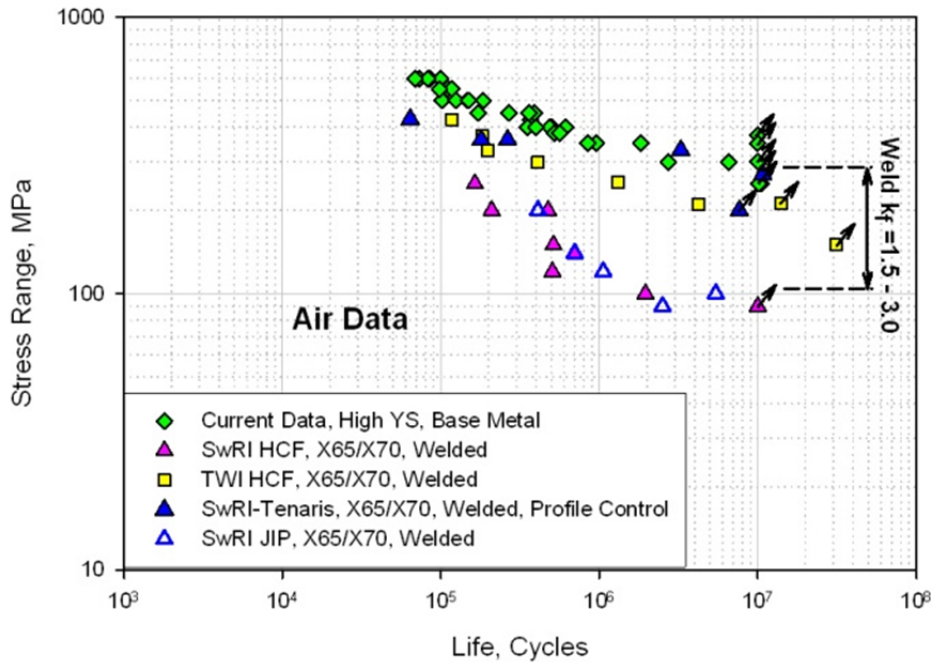


FIGURE 6-8: Comparison of current high-strength steel data with available X65/X70 data in lab air.

Based on the above discussion, if we now assume that the flapping process restores the welded fatigue properties to those of the un-welded condition, we can compute effective fatigue notch reduction factors, k_f , at 10 million cycles for the various welded S-N curves. As indicated in Figure 6-8, this gives k_f values ranging from 1.5 to 3.0.

Figure 6-9 compares the current S-N corrosion-fatigue data in sour brine with available sour brine data on welded X65 data from the literature [4-6]. As can be seen, the unadjusted comparison shows that the current high-strength data have longer corrosion-fatigue lives than those of the welded X65/X70 corrosion-fatigue lives. However, since the later results include the influence of welds, as well as the sour brine environment, a fairer comparison would need to adjust the high-strength data for the threaded connection method that will be employed to join these pipes in service. A first order estimate of this effect on the high-strength steels fatigue lives can be made by assuming an appropriate k_f value for the threaded connections will be in the range of those determined above for the welded joint ($k_f = 1.5$ to 3.0 in Figure 6-8). Applying this range of knock-down factors on stress gives the solid lines shown in Figure 6-9, which can be considered to be a first order estimate of the combined effect of the sour brine environment and threaded connections in high-strength steels. This estimate provides an initial comparison of current riser technology (i.e., welded connections in low-strength steels) versus alternative riser technology (i.e., threaded connections in high-strength steels) for deepwater application. While it is understood that these threaded connections would likely contain

internal seals to prevent ingress of the sour brine environment, the above estimated fatigue performance would nevertheless be useful for initial assessment of remaining fatigue life when considering the possibility that the internal seal is compromised, thereby exposing the threaded connection to the sour brine environment. Of course, this estimate should be verified by performing full-scale fatigue testing on high-strength threaded connections in a sour brine environment. However, a number of technical challenges that would need to be overcome before such data can be obtained.

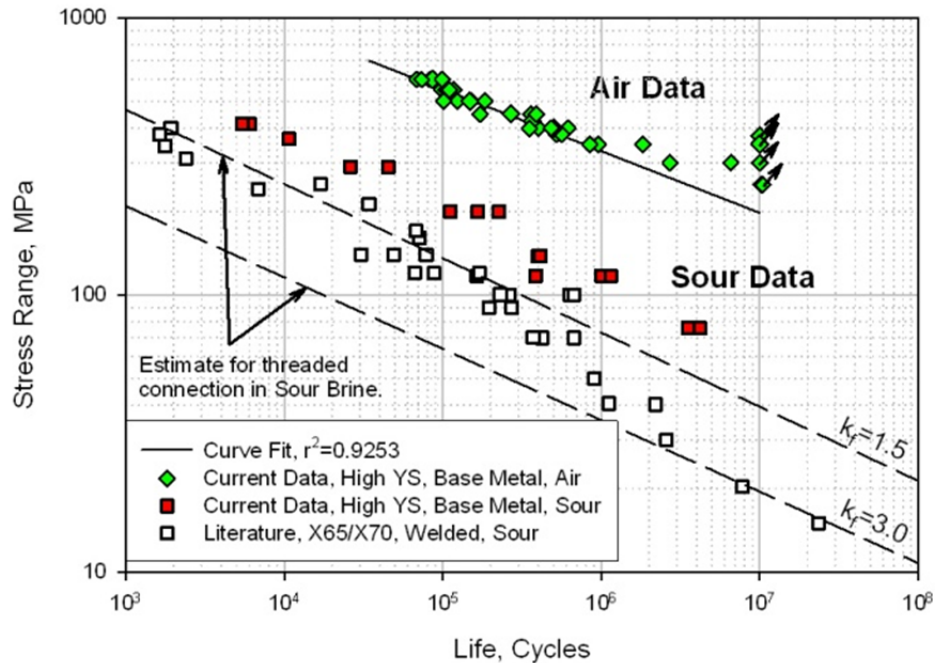


FIGURE 6-9: Comparison of estimated sour brine fatigue performance of high-strength steel with threaded connections versus sour brine fatigue performance of welded X65/X70 steel.

6.1.6 Comparison of Corrosion-Fatigue Trends in S-N Versus Crack Growth Results

As noted above, the trends exhibited in the current S-N corrosion-fatigue results with respect to both strength level and cyclic loading frequency differ from those exhibited by fatigue crack growth rates in these same steels. We can offer two hypotheses to explain these apparent differences between S-N corrosion-fatigue and corrosion-fatigue crack growth kinetics. Before discussing these hypotheses, it is useful to recognize that in general the measured fatigue life (N) in an S-N test is comprised of the number of cycles to initiation of a crack (N_i) plus the number of cycles to propagate the crack to failure (N_p).

The first hypothesis is that the S-N corrosion-fatigue life in the current tests were in fact dominated by the initiation component (that is, $N_i \gg N_p$). And in addition, the material-environment interaction during the corrosion-fatigue initiation component is fundamentally different than that which occurs during the corrosion-fatigue crack growth component. This

hypothesis is particularly viable since the current results were obtained on base materials, as opposed to weldments. Under these conditions, the fatigue initiation life of S-N specimens would be expected to play a more dominant role in controlling the overall fatigue life since the fatigue specimen would not have contained significant intrinsic defects (as are common in welded specimens) to reduce or eliminate the crack initiation component of the total fatigue life. Instead, the predominant fatigue crack initiation location in these base-metal, S-N specimens was observed to occur at the edge of the specimen. Crack initiation was observed to occur preferentially at this location even though the originally sharp edge resulting from initial machining was ground and polished by hand. It was polished to remove possible machining defects, although the effectiveness of this specimen preparation procedure cannot guarantee the removal of all small machining defects. Nevertheless, crack initiation at the specimen edge is also likely to have been promoted due to the lack of constraint at the intersection of the two surfaces, which would give rise to slightly higher strains compared to the nominal strain that existed in the remainder of the specimen.

An alternative hypothesis is that the corrosion-fatigue life in the S-N strip specimens were in fact dominated by fatigue crack growth; however, the noted difference in sensitivity to strength level and cyclic loading frequency between the S-N specimens and the crack growth specimens was due to a crack size/geometry effect. Specifically, the difference between small edge, or surface, cracks in the S-N specimen versus the long, through-thickness cracks in the fatigue crack growth rate specimens. Such crack size/geometry effects have previously been reported to cause differences in corrosion-fatigue crack growth kinetics (da/dN vs. ΔK). Specifically, small surface cracks (0.1 - 1 mm) in high-strength, low-alloy steels exposed to 3.5 percent sodium chloride environments have been shown to grow at significantly faster rates compared to long, through-thickness cracks (25 - 40 mm) in conventional fracture mechanics specimens [28, 29]. It has been proposed that this difference in growth rates is due to the effect of the crack size/geometry differences on mass transport within the crack, which causes changes in the occluded environment at the crack tip [29, 30]. However, this environmental small crack effect has not, to our knowledge, been systematically examined as a function of material strength level or cyclic loading frequency. Thus, further research is needed to confirm that this mechanism is the unequivocal cause of the observed differences between S-N corrosion-fatigue lives and corrosion-fatigue crack growth kinetics.

6.2 Ti-29 S-N Corrosion-Fatigue Results and Discussion

This section summarizes the classical S-N corrosion-fatigue data generated on Ti-29 in the SB environment. Since baseline air data were not generated on this alloy in the current project, these sour brine data will be compared with air data available in the literature. Results will also be compared with S-N corrosion-fatigue data on steels of comparable strength from Section 6.1.

6.2.1 Ti-29 S-N Corrosion-Fatigue in Sour Brine

The Ti-29 corrosion-fatigue data in the sour brine environment are shown in Figure 6-10 (red data points). For comparison, literature data on Ti-23 in air [13] are also shown (green data points), as well as RTI's recommended design curve for welded Ti-29 [12]. As can be seen the corrosion-fatigue lives out to about 4×10^5 cycles are just below the scatter of the air data, thereby indicated a mild reduction in fatigue life of about a factor of two or less due to the sour

brine environment. Moreover, at longer lives the sour brine data cross over the air data as evidenced by the fact that the runout data points in the Ti-29 suggest a fatigue limit at 10^7 cycles in sour brine that is well above 200 MPa, while the air data exhibit failures between 10^6 and 10^7 cycles in this same stress regime. Interestingly, all of the above Ti-29 fatigue lives in sour brine also exceed those of RTI's recommended fatigue design curve for Ti-29 weldmetal [12].

Thus, both the above S-N results in sour brine, as well as the corrosion-fatigue crack growth rate data in Section 5.2, indicate that Ti-29 exhibits only a mild reduction in fatigue life (2 times or less) due to the sour brine environment. However, this conclusion must be tempered by the fact that the baseline air data in this case (Figure 6-10) are for Ti-23 (not Ti-29) and are for basemetal, electron beam (EB) welds, and tungsten inert gas (TIG) welds. Nevertheless, the current results are in general agreement with limited corrosion-fatigue data recently published by RTI on Ti-29 base and weldmetal in sour brine at 150°C and a single applied stress range of 393 MPa [31].

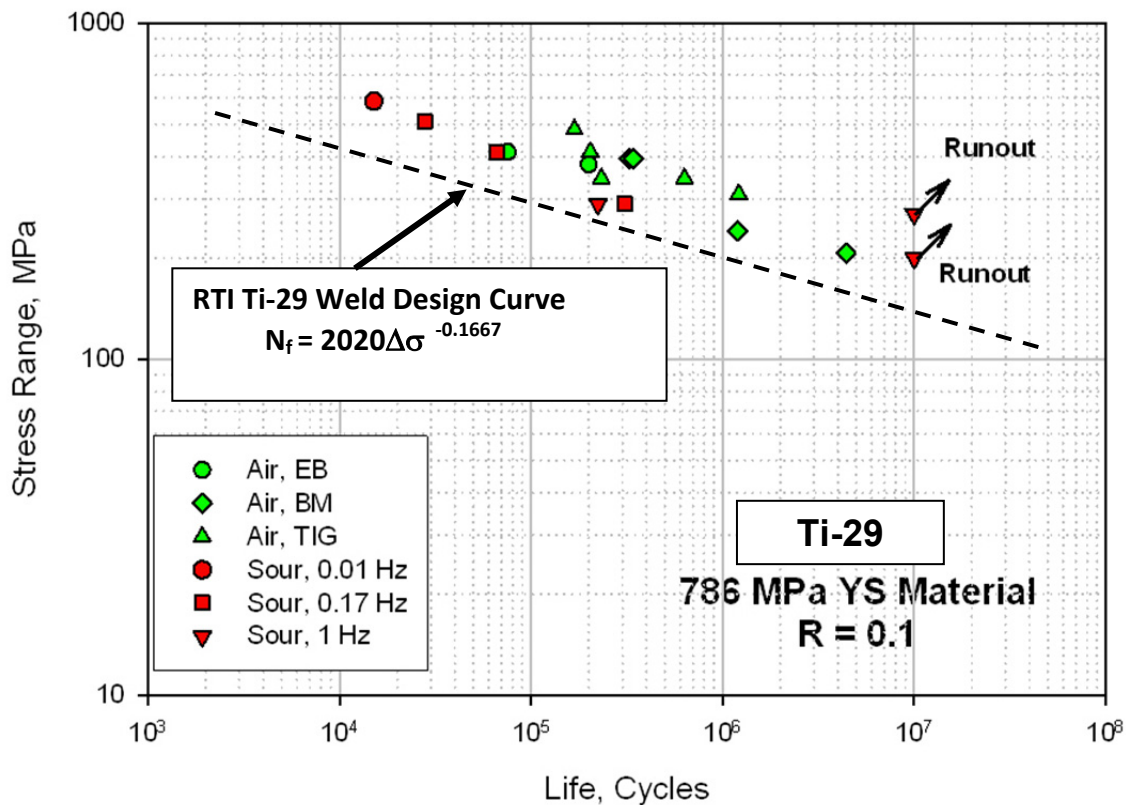


FIGURE 6-10: Comparison of S-N data on Ti-29 in sour brine with Ti-29 air data in base metal (BM), electron beam (EB) welds, and tungsten inert gas (TIG) welds from Ref. [13], and RTI Ti-29 weld design curve [12].

6.2.2 Comparison of S-N Corrosion-Fatigue Performance of Ti-29 and Steels

Figure 6-11 compares the fatigue performance of Ti-alloys in air and sour brine (from Figure 6-10) with those of high-strength steels (Figure 6-4 in Section 6.1.3). As indicated, the baseline air data in Ti-23 exhibit shorter lives at a given applied stress than do the high-strength steels; this is due to the lower modulus and lower ductility of Ti-alloys compared to those in steels. Thus, for a given applied stress, the strain is higher and the strain capacity is lower in Ti-alloys than in a steel of comparable strength level. This effect is analogous to that discussed previously in Section 5.2.1 in relation to fatigue crack growth performance of Ti alloys versus steels.

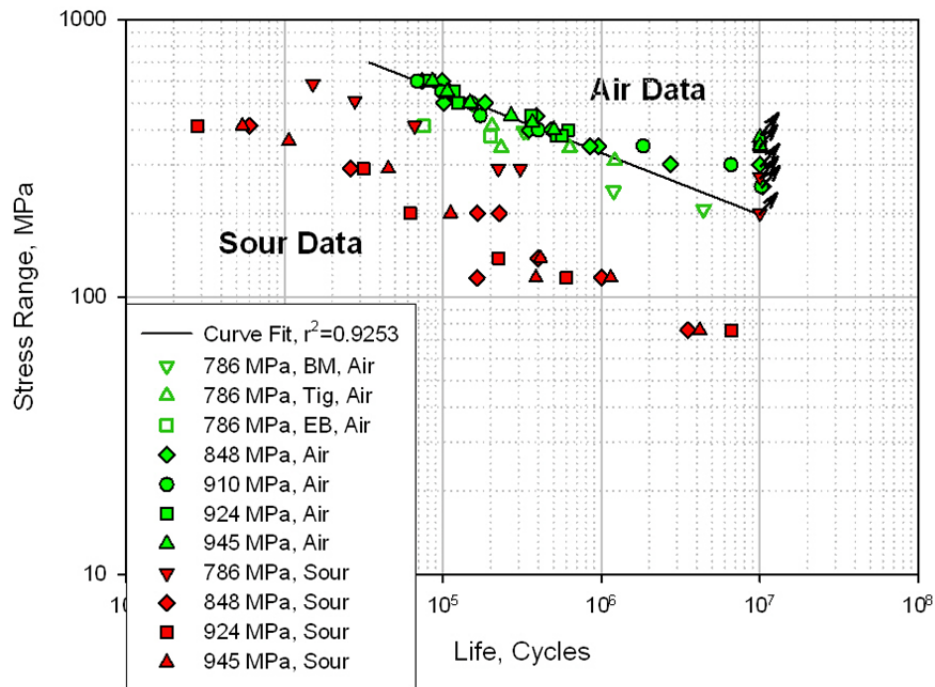


FIGURE 6-11: Comparison of sour brine and air data on 786 MPa YS Ti-29 alloy (from Figure 6-10) with sour brine and air data in high-strength steels (from Figure 6-4).

However, the above effect is more than compensated for by the alloy compositional differences between the two materials, which render Ti-alloys more resistant to general and localized corrosion, as well as to hydrogen permeation. Consequently, the sour brine environment reduces the fatigue life of Ti-29 by less than an factor of two compared to the air baseline performance, while the fatigue lives in high-strength steels are reduced by factors ranging from 30 at higher applied stress ranges, to 100 at lower applied stress ranges. Thus, Ti-29 has markedly superior resistance to S-N corrosion-fatigue life in sour brine environment. Even if one compares the corrosion-fatigue performance of the two materials on an absolute basis, the Ti-29 outperforms the high strength steels in corrosion-fatigue resistance by a factor of 10 to 15 times on life.

Of course, steel still has a significant cost advantage; thus Ti-29 has been employed selectively in applications like tapered stress joints in deepwater oil and gas production to capitalize on the alloy's low modulus and relatively high strength. However, it is important to recognize that in these applications the connection of the titanium stress joint to the steel risers can induce a galvanic couple. Under these conditions the stress joint will be the cathode, thereby subjecting the Ti-29 to cathodic charging of hydrogen – in addition to any production of hydrogen from the reaction of the sour brine production fluid with the material. The potential degree of degradation to the Ti-alloy from these two combined sources of hydrogen is the subject of ongoing research.

7.0 SUMMARY AND CONCLUSIONS

This section provides a summary and conclusions based on corrosion-fatigue results from the current project, as well as comparisons of current results with relevant experimental and theoretical mechanistic results from the literature. First, corrosion-fatigue crack growth rate results are summarized; these are followed by a summary of S-N corrosion-fatigue results. Results on each of the above two corrosion-fatigue characterization methods are also separated for steels and alloy T-29, although comparisons between the materials, as well as the characterization methods are made where appropriate.

7.1 Corrosion-Fatigue Crack Growth Rates

7.1.1 Steel $da/dN(\Delta K)$ Summary and Conclusions

1. Frequency-scan test results obtained at a constant $\Delta K = 22$ MPa \sqrt{m} and $R = 0.5$ on five new high-strength riser steels ranging in yield strength from 848 MPa to 1080 MPa and exposed to either seawater and sour brine environments exhibited the classical frequency dependence with increasing corrosion-fatigue crack growth rates with decreasing cyclic frequency.
2. Frequency-scan tests also showed that for certain material-environment combinations a saturation frequency of about 0.1 Hz occurred below which the rates did not increase appreciably; however, for other material-environment combinations rates continued to increase with decreasing frequency down to a frequency of 0.01 Hz with no indication of a saturation frequency.
3. The above frequency response differs from that previously reported for currently used riser steels with yield strength of 450 to 500 MPa that have exhibited a saturation frequency in sour brine environment of about 0.1 to 0.33 Hz, depending on the specifics of the environment.
4. The magnitude of the corrosion-fatigue crack growth rates in both frequency-scan tests at constant- ΔK and corrosion-fatigue crack growth rates with decreasing- ΔK values was primarily dependent on the steel's YS level, with increasing YS resulting in increasing rates; however, the 910 MPa YS steels did not follow this trend, thereby

suggesting that steel processing and microstructure may also influence corrosion-fatigue crack growth rate performance.

5. At low ΔK values in the constant- K_{\max} and decreasing- ΔK tests, an inverse frequency dependence was observed in both seawater and sour brine environments in which rates decreased with decreasing frequency.
6. The inverse frequency dependence at low ΔK is believed to result from corrosion product wedging near the crack-tip, which causes crack closure – that is, the effective ΔK becomes less than the applied ΔK computed from applied loads and crack size.
7. In the low ΔK regime, it is believed that the inverse frequency dependence arises from a competition between the time-dependent build-up of corrosion product wedging versus the time-dependent advance of the crack. In contrast, in the high ΔK regime, it is believed that the classical frequency response arises from the underlying kinetics processes responsible for supplying damaging species (likely hydrogen in this case) to the crack-tip region.
8. The inverse frequency effect observed at low ΔK holds significant potential for providing a basis to optimize fatigue testing in the high cycle fatigue regime, thereby saving time and resources; however, formulating universally applicable procedures for such testing will require a more complete understanding of this phenomenon.

7.1.2 *Ti-29 Alloy da/dN(ΔK) Summary and Conclusions*

1. Baseline fatigue crack growth rates in Ti-29 in air at high ΔK are three to four times faster than those in the high strength steels; for a strain-controlled fatigue crack growth mechanism, this behavior is consistent the lower elastic modulus and tensile ductility in Ti-29 compared to steel. However, at low ΔK the rates in Ti-29 in air are comparable to those in steel – this is theorized to be caused by roughness-induced crack closure that reduces the local crack driving force at low ΔK , thereby overcoming the effect of lower modulus and ductility that dominates at high ΔK .
2. Frequency scan testing at $\Delta K = 22$ MPa \sqrt{m} and $R=0.5$ in Ti-29 in the sour brine environment initially exhibited two to three times faster rates than those in air at frequencies of 10 Hz and 1 Hz, respectively; however, subsequent rates at lower frequencies of 0.33, 0.1, and 0.01 Hz appeared to be independent of frequency and continued to decrease as the crack grew to rates that were a factor of two below the air baseline results.
3. Frequency scan results in air, tested under identical loading conditions to those in sour brine, were independent of frequency from 10 Hz to 0.01 Hz, thereby suggesting that the above results in sour brine environment were not the result of fabrication-induced residual stresses in the Ti-29 pipe or of an inherent material strain rate sensitivity.

4. Examination of the fracture surfaces from the frequency scan tests in Ti-29 showed that cracks grown in sour brine exhibited very rough surfaces with numerous secondary out-of-plane cracks. Thus, it was concluded that the unusual frequency response in Ti-29 was due to decreasing local crack-tip driving force as the crack grew, due to the combined effect of roughness induced crack closure, as well as a crack-tip branching and secondary out-of-plane cracking.
5. Fatigue crack growth rates as a function of the applied ΔK at $K_{\max} = 48.8$ MPa \sqrt{m} in Ti-29 in sour brine exhibited initial rates at $\Delta K = 20$ to 34 MPa \sqrt{m} that were two to four times faster than those in air, but as the crack grew and ΔK decreased, the rates became equal to or less than the rates in air; this behavior was generally similar to that observed in the frequency scan tests in sour brine, and is believed to be controlled by the same crack closure mechanism.
6. At high ΔK , the effect of the higher baseline crack growth rates in air, combined with increase the three-fold increase in rates due to the sour brine, resulted in overall corrosion-fatigue crack growth rates in Ti-29 that approach those in steels; however, at low ΔK the reduction in the crack driving force in Ti-29 due to roughness induced crack closure in sour brine result in Ti-29 rates that were comparable to air crack growth rates in steels. Thus, for sour-service applications in the intermediate and high cycle fatigue regime, Ti-29 exhibited more favorable corrosion-fatigue crack growth resistance than that of steels.

7.2 S-N Corrosion-Fatigue Life

7.2.1 Steel S-N Summary and Conclusions

1. Fatigue lives in air were observed to be independent of material strength level over the range of yield strengths from 848 MPa to 945 MPa, although fatigue lives were measurably longer for the highest yield strength material at 1080 MPa.
2. The fatigue endurance limit at 10 million cycles in air was about 300 MPa and independent of strength level for yield strengths ranging from 848 MPa to 924 MPa, while it was above 400 MPa for yield strengths of 945 MPa and 1080 MPa.
3. Corrosion-fatigue lives in the seawater with cathodic protection were two to ten times less than those measured in air, and this difference increased with decreased applied stress range.
4. Corrosion-fatigue lives in the sour brine environment were 30 to 100 times less than those measured in air, and this difference increased with decreasing applied stress range, as in the seawater environment.
5. Corrosion-fatigue occurred in seawater with cathodic protection and in sour brine at stresses significantly below the fatigue endurance limit at 10 million cycles in air.

6. Corrosion-fatigue S-N behavior exhibited no measurable differences as a function of material strength level for yield strengths from 848 MPa to 1080 MPa in the seawater with cathodic protection environment and for yield strengths from 848 MPa to 945 MPa in the sour brine environment.
7. The effect of cyclic frequency on corrosion-fatigue behavior was mixed and exhibited both the classic frequency effect with lives decreasing with decreasing frequency, as well as the inverse frequency effect with lives decreasing with increasing frequency, although the effect of frequency was likely confounded by the inherent scatter in the S-N measurements.
8. Corrosion-fatigue lives in S-N tests were considerably less sensitive to cyclic loading frequency, and steel strength level and/or microstructure than were fatigue crack growth rate kinetics (da/dN vs. ΔK) in these same steels and environments.
9. Although several hypotheses were proposed to explain the above differences, the fundamental understanding and critical experimental results needed to clarify these differences are presently lacking.

7.2.2 Ti-29 S-N Summary and Conclusions

1. The S-N corrosion-fatigue performance of Ti-29 basemetal is mildly reduced by the sour brine environment used in the current project; specifically, the S-N fatigue lives were reduced by a factor of two or less compared to air data from the literature on Ti-23 basemetal and weldmetal (EB and TIG), all of which were indistinguishable.
2. The endurance limit at 10 million cycles in Ti-29 basemetal in the sour brine environment used in the current project appear to be higher than those from the literature on Ti-23 basemetal and weldmetal (EB and TIG) in air.
3. The Ti-29 basemetal corrosion-fatigue lives in the sour brine environment used on the current project are longer than the lives given by the Ti-29 weld design curve proposed by RTI.

8.0 ACKNOWLEDGEMENTS

The support of the Research Partnership to Secure Energy for America (RPSEA) under prime contact with the U.S. Department of Energy (Contract DE-AC26-07NT42677), as well as co-funding from BP, is gratefully acknowledged. We also acknowledge the support and encouragement of James Pappas of RPSEA and Jim Chitwood of Chevron, who are respectively the current and past managers of the RPSEA Ultra-Deepwater Floating Facilities Project 07121-1403, as well as Paul Devlin, Chairman of RPSEA's Technical Advisory Committee. The contributions of Steven Shademan and Himanshu Gupta, both of BP, who co-chaired the Project Working Committee, are also acknowledged.

9.0 REFERENCES

- [1] Buitrago, J. and Weir, M.S., 2002, "Experimental Fatigue Evaluation of Deepwater Risers in Mild Sour Environment," Deep Offshore Technology Conf., New Orleans, LA.
- [2] Baxter, D.P., Maddox, S.J., and Pargeter, R.J., 2007, "Corrosion Fatigue Behaviour of Welded Risers and Pipelines," OMAE2007-29360, 26th Int'l. Conf. on Offshore Mechanics and Arctic Engineering, San Diego, CA.
- [3] McMaster, F., Thompson, H., Zhang, M., Walters, D., and Bowman, J., 2007, "Sour Service Corrosion Fatigue Testing of Flowline Welds," OMAE2007-29060, 26th Int'l. Conf. on Offshore Mechanics and Arctic Engineering, San Diego, CA.
- [4] Buitrago, J., Hudak, S.J. Jr., and Baxter, D., 2008, "High-Cycle and Low-Cycle Fatigue Resistance of Girth Welds in Sour Service," OMAE2008-57545, 27th Int'l. Conf. on Offshore Mechanics and Arctic Engineering, Estoril, Portugal.
- [5] McMaster, F., Bowman, J., Thompson, H., Zhang, M., and Kinyon, S., 2008, "Sour Service Corrosion Fatigue Testing of Flowline and Riser Welds," OMAE2008-57059, 27th Int'l. Conf. on Offshore Mechanics and Arctic Engineering, Estoril, Portugal.
- [6] Hudak, S.J. Jr. and McMaster, F., 2003, "Corrosion-Fatigue of Carbon Steel Weldments in Sour Environments," Final Report to ExxonMobil, SwRI Project No. 18.04860, Southwest Research Institute, San Antonio, TX.
- [7] Darcis, Philippe P., Marines-Garcia, Israel, Hudak, Stephen J. Jr., Armengol, Mariano, and Quintanilla, Hector M., "Sour Environmentally Assisted Fatigue of Welded SCR Materials – Post-Weld Finishing Treatment Evaluation, 29th Int'l. Conf. on Offshore Mechanics and Arctic Engineering, OMAE2010-21026, Shanghai.
- [8] Bartlett, M.L. and Hudak, S.J. Jr., 1990, "The Influence of Frequency-Dependent Crack Closure on Corrosion Fatigue Crack Growth," Fatigue '90, pp. 1783-1788.
- [9] Hudak, S.J. Jr., Birring, A.S., Bartlett, M.L., and Hanley, J.J., 1990, "Control of Corrosion-Fatigue in NGV Fuel Cylinders," SwRI Project No. 06-1566, GRI Contract No. 5086-252-1440, GRI-89/0239, Southwest Research Institute, San Antonio, Texas.
- [10] Buitrago, J., Weir, M.S., Kan, W.C., Hudak, S.J. Jr., and McMaster, F., 2004, "Effect of Loading Frequency on Fatigue Performance of Risers in Sour Environment," Offshore Mechanics and Arctic Engineering Conf., OMAE 2004-51641, Vancouver.
- [11] Hudak, S.J. Jr., Feiger, J.H., Patton, J.A., 2010, "The Effect of Cyclic Loading Frequency on Corrosion-Fatigue Crack Growth in High-Strength Riser Materials, 29th Int'l. Conf. on Offshore Mechanics and Arctic Engineering, OMAE2010-20705, Shanghai.

- [12] Baxter, C., Pillai, S., and Hutt, G., Advances in Titanium Risers for FPSO's, Offshore Technology Conference, OTC8409, Vol 2, pp497-508, 1997.
- [13] Salama, M.M., Murali, J., and Joosten, M.W., 1998, "Titanium Drilling Risers – Application and Qualification," OMAE1998-2110, 17th Int'l. Conf. on Offshore Mechanics and Arctic Engineering, Lisbon, Portugal.
- [14] Salama, M.M., Murali, J., and Joosten, M.W., 2000, "Titanium Drilling Risers – Application and Qualification," Journal of Offshore Mechanics and Arctic Engineering, Vol. 122, pp. 47-51.
- [15] Salama, M.M., 2001, "Fatigue Crack Growth Behavior of Titanium Alloy Ti-6Al-4V and Weldment," Journal of Offshore Mechanics and Arctic Engineering, Vol. 123, pp. 141-146.
- [16] Babalola, O.T. and Berge, S., 2002, "Fatigue of Titanium Welds – Models for Assessment of Defect Sensitivity," OMAE2002-28578, 21st Int'l. Conf. on Offshore Mechanics and Arctic Engineering, Oslo, Norway.
- [17] Berge, S., Mainçon, P., and Hauge, M., 2002, "Fatigue of 28-inch Titanium Riser – SN Data and Defect Assessment," OMAE2002-28577, 21st Intl. Conf. on Offshore Mechanics and Arctic Engineering, Oslo, Norway.
- [18] Berge, S., Eide, O.I., and Mainçon, P., 2002, "Fatigue Strength of Titanium Riser Welds – Effects of Material Grade and Weld Method," OMAE2002-28576, 21st Int'l. Conf. on Offshore Mechanics and Arctic Engineering, Oslo, Norway.
- [19] Baxter, C.F.G., 2008, "Cyclic & High Strain Behavior of Titanium Alloys Used for Riser Components," OMAE2008-57157, 27th Int'l. Conf. on Offshore Mechanics and Arctic Engineering, Estoril, Portugal.
- [20] ASTM E 647, "Standard Test Method for Measurement of Fatigue Crack Growth Rates," ASTM Annual Book of Standards, Volume 03.01, ASTM, Philadelphia, PA.
- [21] S. J. Hudak, Jr., J. F. H. Feiger, J. A. Patton, *The Effect of Cyclic Frequency on Corrosion – Fatigue Crack Growth in High Strength Riser Materials*. Proc. ASME 2010, Intern. Conf. on Ocean, Offshore and Arctic Engineering, OMAE2010-20705, Shanghai, June 6-11, 2010.
- [22] C. M. Holtman, D. P. Baxter, I. A. Ashcroft, R. C. Thomson, *An Investigation into Fatigue Crack Growth Test Methods on Sour Environment*, Int. J. Offsh. Polar Eng., 20, 2010, 103-109.
- [23] C. M. Holtman, D. P. Baxter, I. A. Ashcroft, R. C. Thomson, *Effect of Crack Depth on Fatigue Crack Growth Rate for a C-Mn Steel in a Sour Environment*, Intern. J. Fat., 32, 2010, 288-296.
- [24] Hudak, S.J. Jr. and Davidson, D.L., 1987, "The Dependence of Crack Closure on Fatigue Loading Variables, in *Mechanics of Closure*, ASTM STP 982, J.C. Newman, Jr., and W. Elber, Eds., pp. 121-138.

- [25] Dawson, D.B. and Pellou, R.M., 1974, "Corrosion Fatigue Crack Growth in Titanium Alloys in Aqueous Environments," *Met. Trans.*, Vol. 5, pp. 723-731.
- [26] Hudak, S.J. Jr., FitzGerald, F.H., and Wei, W., 1987, "The Influence of Corrosion-Product Wedging and Crack Surface Morphology on Corrosion Fatigue Crack Growth in Aluminum Alloys," Final Rpt. Contract No. T&M-23152-C, Douglas Aircraft Co., Long Beach, CA.
- [27] Wei, R.P., 1979, "On Understanding Environment Enhanced Fatigue Crack Growth: A Fundamental Approach, in *Fatigue Mechanisms*, Edited by J. T. Fong, ASTM STP 675, pp. 816-840.
- [28] Gangloff, R.P., 1981, "The Criticality of Crack Size in Aqueous Corrosion Fatigue," *Research Mechanica Letters*, Vol. 1, pp. 299-306.
- [29] Gangloff, R.P., 1985, "Effect of Crack Size on the Chemical Driving Force for Corrosion Fatigue," *Metallurgical Trans.*, Vol. 16A, pp. 953-969.
- [30] Turnbull, A., 1982, "A Theoretical Evaluation of the Influence of Mechanical Variables on the Concentration of Oxygen in a Corrosion Fatigue Crack," *Corrosion Science*, Vol.22, pp. 877-893.
- [31] Schutz, R. W., Baxter C. F., and Caldwell, C. S., 2010, "Effect of Sour Brine Environment on the S-N Fatigue Life of Grade 29 Titanium Pipe Welds, Paper No. 10313, NACE Corrosion 2010, Houston, TX.